SHEAR STRENGTH ASSESSMENT OF CORROSION-DAMAGED PRESTRESSED CONCRETE GIRDERS

Abdullah Al Rufaydah

Thesis submitted to the faculty of the Virginia Polytechnic Institute and State University in partial fulfillment of the requirements for the degree of

Master of Science

in

Civil Engineering

Carin L. Roberts-Wollmann, Chair

Ioannis Koutromanos

Matthew Hebdon

November 20, 2020

Blacksburg, Virginia

Keywords: Corrosion Damage, Shear strength, Prestressed concrete girders, Bridges, Forensic engineering, Residual shear strength

SHEAR STRENGTH ASSESSMENT OF CORROSION-DAMAGED PRESTRESSED CONCRETE GIRDERS

Abdullah Al Rufaydah

ABSTRACT

Corrosion is a concern in old prestressed concrete bridges, especially bridges built in marine environments. Corrosion induces cracks in the concrete superstructure which accelerates the deterioration rate and can result in a complete loss of the concrete cover and exposure of the reinforcing and prestressing steel. This causes degradation in the load-carrying capacity of the bridge girders. Consequently, decisions need to be made on whether to replace, retrofit, or load post these bridges. Extensive research has focused on the flexural strength of corroded prestressed concrete girders. This research studies the shear strength of corroded prestressed concrete girders which can, then, be expanded further to evaluate the possible retrofitting techniques for restoring, or enhancing, their shear strengths.

Two old prestressed concrete girders built in the 1960's and 1970's were delivered to the Murray Structural Engineering Laboratory at Virginia Tech from two decommissioned bridges in Virginia. The two girders showed signs of deterioration due to corrosion. Non-destructive testing was performed to evaluate their in-situ conditions. For both girders, each end was tested in the lab in three-point loading condition to make full use of the girders. Shear capacities of the girders were predicted using four methods in the current AASHTO LRFD and the ACI codes. In addition, analyses using Response2000 and strut-and-tie modelling were also carried out. Evaluation of these methods and comparisons with the experimental results were performed to reach to conclusions and recommendations for future work.

Corrosion in strands seemed to not have as much influence on the shear capacity as on the flexural capacity. Destructive shear tests indicated that the actual shear capacities of the girders investigated in this research exceeded nominal capacities

predicted by the current codes. However, the flexural capacities were reduced. Possible reasons for the girders' behaviors are discussed.

SHEAR STRENGTH ASSESSMENT OF CORROSION-DAMAGED PRESTRESSED CONCRETE GIRDERS

Abdullah Al Rufaydah

GENERAL AUDIENCE ABSTRACT

Many bridges in the United States were built using longitudinal members, called girders, made of prestressed concrete. In prestressed concrete, because concrete cannot resist high tensile forces, tensioned steel cables, called strands, are used to produce compression on the concrete member to improve its behavior when it is in service. Corrosion is a concern in old prestressed concrete bridges, especially bridges built in marine environments. Corrosion induces cracks in the concrete superstructure which accelerates the deterioration rate and can result in a partial loss of the concrete body and exposure of the embedded steel. This causes degradation in the load-carrying capacity of the bridge girders which raises a danger to vehicles, passengers, and pedestrians. Consequently, decisions need to be made by authorities on whether to replace, repair, or load post these bridges. Two main types of loads exist in bridge girders, namely shear forces and bending moments. Extensive research has focused on the ability of corroded prestressed concrete girders to resist stresses produced by moment, or flexure. However, bridge girders must also resist shear forces. This research studies the shear strength of corroded prestressed concrete girders which can, then, be expanded further to evaluate the possible retrofitting techniques for restoring, or enhancing, their shear strengths.

Two old prestressed concrete girders built in the 1960's and 1970's were delivered to the Murray Structural Engineering Laboratory at Virginia Tech from two decommissioned bridges in Virginia. The two girders showed signs of deterioration due to corrosion. These signs include concrete losses, cracks, areas of unsound concrete, and exposed strands. Non-destructive testing was performed on the girders to evaluate the severity of their in-situ conditions. Then, two destructive full-scale tests were performed on each girder in the lab to estimate their actual shear strengths. Shear strengths of the girders were also predicted using four methods present in the current American

Association of State Highway and Transportation Officials, AASHTO, and the American Concrete Institute, ACI, codes. In addition, analyses using other advanced tools were also carried out. Evaluation of these methods and comparisons with the experimental results were performed to reach to conclusions and recommendations for future work.

Corrosion in strands seemed to not have as much influence on the shear strength as on the flexural strength. Destructive shear tests indicated that the actual shear strengths of the girders investigated in this research exceeded nominal strengths predicted by the current codes, the AASHTO and the ACI. However, the flexural strengths were reduced. Possible reasons for the girders' behaviors are discussed.

AKNOWLEDGEMENTS

Firstly, I would like to thank God for the opportunity to pursue my studies at Virginia Tech. Secondly, I would like to thank my government for supporting me during my educational journey.

I would like to deeply thank Dr. Roberts-Wollmann for being my advisor and for her continuous support, guidance, and encouragement throughout my journey at Virginia Tech. I would like to extend my gratitude to the committee members Dr. Koutromanos and Dr. Hebdon for their support and guidance. I am also grateful to the whole team involved in this project for sharing their expertise and knowledge with me.

I would like to thank Virginia Tech for welcoming me and providing me with the environment to pursue my studies. I would like to thank the lab manager, technicians, and all students at the Thomas M. Murray Structures Laboratory for making my research possible. I thankfully acknowledge the support of the Virginia Department of Transportation (VDOT) and the Virginia Transportation Research Council (VTRC) to this project which I had the advantage to be part of.

I would like to thank my family for their emotional support and encouragement while I am studying abroad. Special thanks to my colleague and companion during my journey Ali Alfailakawi for his generous and uninterrupted offer to help me anytime and anywhere. I thank everyone I met in Blacksburg.

TABLE OF CONTENTS

LIST OF FIGURES

LIST OF TABLES

CHAPTER – 1 INTRODUCTION

1.1. Motivation

Corrosion in concrete bridge girders is a concern that affects the strength and durability of bridges and safety of passengers and vehicles. Many bridges in the United States were constructed in the 1950's and 1960's. According to Naito et al. (2011), most wearing surfaces were constructed directly on the superstructure without waterproofing barriers. While concrete cover is meant to protect the reinforcing steel, accumulation of chloride to a certain limit can initiate corrosion in the embedded reinforcement (Chloride Corrosion Threshold). Collapses and shutdowns of bridges due to corrosion have raised questions about the reliability of other in-service bridges. In Virginia, deicing chemicals are used frequently to keep roads safe during the winter season. These agents can leak and reach to the reinforcing steel through concrete pores and expansion joints. In addition, bridges built in marine environments are susceptible to corrosion due to the spray of salt water. Even though bridges are inspected and load rated periodically, corrosion damage may not be visible on the concrete surface until advanced stages. Techniques and tools for detecting corrosion damage in concrete bridges are evolving. Recently, a nondestructive technique for detecting corrosion using magnetic flux leakage looks promising for detecting corrosion damage in box girders at early stages. This device is cost efficient and can be deployed in the inspection process of bridges (Chase and Balakumaran, 2020).

In addition to the corrosion issue, bridges constructed following the 1950's and 1960's era provisions could be determined to be inadequate according to newer design codes and construction methods. One important design aspect that has evolved is the shear provisions. Catastrophic shear failures which are brittle in nature have led to accelerated research over the past decades. Pei et al. (2008) points out that girders designed prior to the 1979 interim were usually less conservative in terms of shear capacity than the subsequent codes. Runzell et al. (2007) says that the 2002 Standard and

the 2004 LRFD include more stringent requirements for shear reinforcement than the 1979 interim. This study aims to address the aforementioned issues and add to the previous work done in this field.

This current study is part of an ongoing project at Virginia Tech funded by the Virginia Department of Transportation (VDOT), and the Virginia Transportation Research Council (VTRC) to evaluate and repair bridges in Virginia that show signs of deterioration due to corrosion. Repair techniques include external post-tensioning reinforcement, CFRP, and others. Nine I-shaped prestressed concrete girders and six adjacent-box beams were recovered from the Lesner Bridge and the Aden Road Bridge in Virginia, respectively, and delivered to the Thomas Murray Structures Lab at Virginia Tech for the purpose of this project. These girders show signs of deterioration with varying levels. The current study discusses mainly the unrepaired shear strength of corrosion damaged prestressed concrete bridge girders in Virginia. Figure 1 and Figure 2 show the condition of the Lesner and Aden Bridges before being demolished.

Figure 1 Deterioration in the Lesner Bridge (Alfailakawi et al., 2020)

Figure 2 Deterioration in the Aden Bridge (Alfailakawi et al., 2020)

1.2. Objectives and Scope

1.2.1. Objectives

To provide guidance for bridge inspectors in rating deteriorated girders for shear, some uncertainties regarding shear strength of girders that show signs of corrosion must be alleviated. Therefore, this study aims to:

- Compare the shear strength of girder ends that have different levels of deterioration.
- Investigate the shear and flexural behavior and the failure mode of girder ends that have different levels of deterioration.

- Evaluate the adequacy of bridges constructed in the 1960's and 1970's in light of the current design codes.
- Evaluate previous recommendations for flexural strength calculation of corrosion damaged prestressed concrete girders; also, evaluate these recommendations in case of deep beams.
- Add new full-scale test results to the limited database of shear strength of corrosion damaged prestressed concrete girders.

1.2.2. Scope

To accomplish the objectives of this research, a thorough review of the available literature concerning the shear strength of deteriorated bridge girders was conducted. Two prestressed concrete bridge girders recovered from decommissioned bridges in Virginia with different levels of corrosion damage at the two ends of each girder were selected for shear testing in the lab. Girders and test configurations in this study were selected to allow a head-to-head comparison between the shear strength of the damaged and undamaged, or less damaged, ends. Then, destructive investigation and material testing were performed to gain information about the in-situ condition of girders. Shear and flexural strengths of the girders were predicted using different methods provided in the 2017 AASHTO LRFD and the ACI318-19 codes. These calculations were refined using tested material properties, measured parameters during physical tests, and recommendations proposed in the literature. Evaluation of these methods, analyses, and comparisons with the experimental results were performed to reach to conclusions. Computer software used to aid in this research were Microsoft Excel, Mathcad.15, Response 2000, and GOM Correlate.

Beyond the scope of this research, other girders from the same bridges will be repaired to return them to their original shear strength. These repair techniques will be evaluated in a separate research. However, this research is considered as a step towards this goal.

1.3. Limitations of the Research

- This research investigates prestressed concrete girders designed using old provisions which are found to be different from the current ones.
- Most of the shear span-to-depth ratios of the girders used in this research are less than 2.5 which makes the entire shear span fall in a disturbed region (ACI-ASCE Committee 445). Therefore, the resistance mechanism for this type of beams can be significantly different than others with higher shear span-to-depth ratios. The reason for selecting small shear span-to-depth ratios will be discussed later.
- Girders selected for this research included signs of corrosion damage. However, most of this damage was on or near the soffits of the girders. There were no noticeable signs of corrosion damage in their webs nor exposed shear reinforcement.

1.4. Background on Bridge girders investigated in this research

Girders used in this research were recovered from the Lesner Bridge and the Aden Road Bridge in Virginia prior to the demolition phase. The bridge plans are provided in appendix-A.

The west-bound side of Lesner Bridge was constructed in 1967 and is located in Virginia Beach. After about 49 years of service, the bridge was demolished. Lesner girders were AASHTO Type II pretensioned concrete with overall lengths of 49.75 ft. The west bound lanes of the bridge are supported by seven girders spaced 5ft-2.5 in center-to-center. The nominal concrete compressive strength from the bridge plans was 4000 psi. A 38-in wide strip of the composite concrete deck was cut and delivered attached to the girder. A 1.25-in thick overlay was attached to the concrete deck. The haunch thickness was varying along the length of the girder. The measured thickness of the haunch near the ends was 1 in. Lesner girders were prestressed with 22 7/16-in Grade 270 stress-relieved seven-wire strands distributed in seven layers. Based on the bridge plans, strands were prestressed to produce a total prestressing force of 477.4 kip (21.7 kip per strand). Nowadays, a 7/16-in strand has a cross sectional area of 0.115 in^2. However,

the plans showed that the area of strands is 0.117 in^2, which will be used in all subsequent calculations for the Lesner specimen.

The shear reinforcement of the Lesner girders consists of two No. 4 bars spaced as shown in Figure 3. The yield stress of stirrups was missing in the bridge plans. However, 40 ksi was assumed for preliminary calculations as it was the commonly used grade for reinforcing bars at that time. Figure 4 shows the cross section of a Lesner Bridge girder.

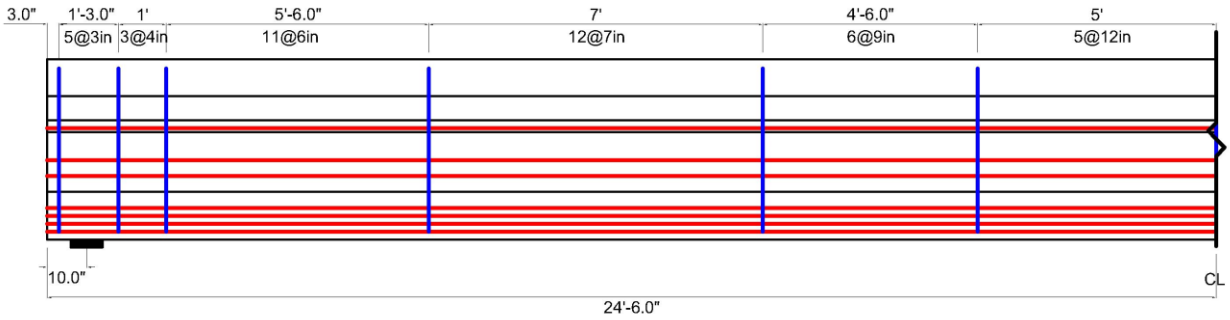

Figure 3 Longitudinal section of the Lesner girder

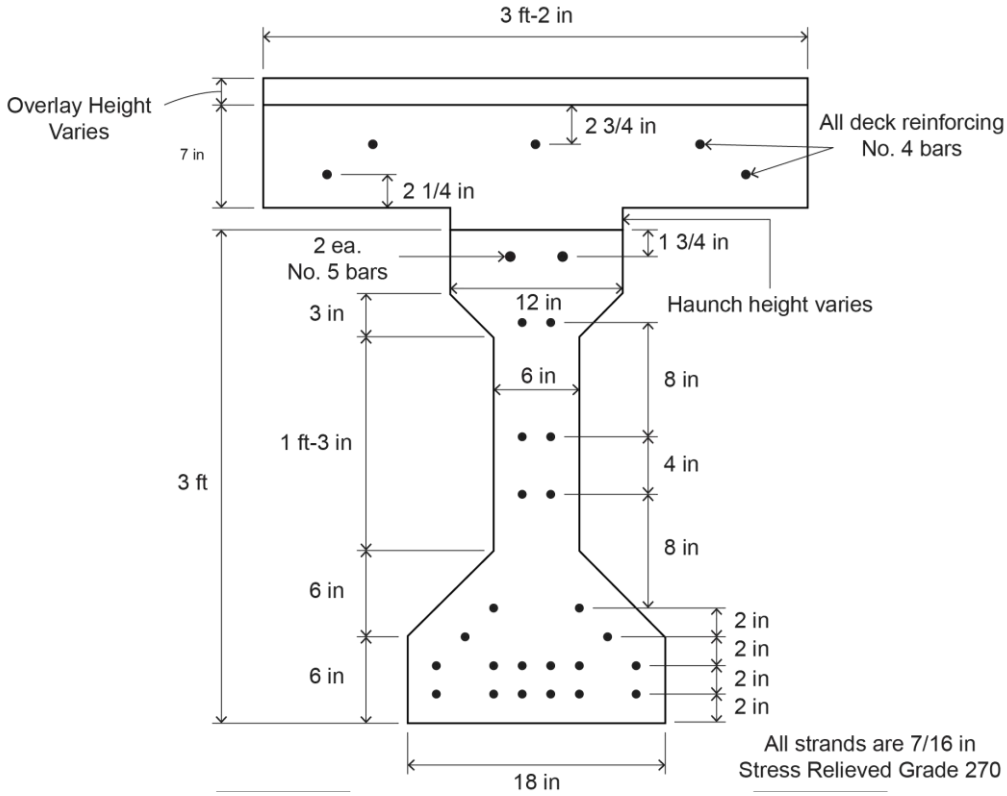

Figure 4 Cross-section of the Lesner girder (Alfailakawi, 2020)

The Aden Road Bridge is located near Quantico, Virginia and was constructed in 1979. After about 34 years of service, the bridge was demolished. The Aden bridge consists of two 3-ft wide exterior girders and seven 4-ft wide interior girders tied laterally with two post-tensioning ties along the span length. The girder used in this research is an interior one. All girders were adjacent box prestressed concrete beams with overall lengths of 55 ft. The specified nominal concrete compressive strength from the bridge plan was 5000 psi. The wearing surface was removed before they were delivered to the lab. Aden girders were reinforced with 33 7/16-in Grade 270 stress-relieved seven-wire strands distributed in six layers. Based on the bridge plans, strands were prestressed to produce a total prestressing force of 716.1 kip (21.7 kip per strand).

The shear reinforcement of the Aden girders consists of two types of stirrups. First, No. 5 pairs of lapped U-shaped stirrups forming close units with spacing of 12 in. for the entire length, except for the first and last three stirrups near the ends which were 4-in. spaced. The top U-shaped stirrups were epoxy-coated. Second, other No. 5 inverted U-shaped stirrups were provided at the top of the girder with a leg length of 18 in. These stirrups were also epoxy-coated with spacing of 12 in. In the preliminary shear strength calculations, the second type of stirrups was assumed not to contribute to the nominal shear strength of the girder due to lack of anchorage. The two types of stirrups were staggered as shown in Figure 5 (Stirrups are not shown for the entire length). The yield stress of stirrups was missing in the bridge plans. However, 40 ksi was assumed for preliminary calculations as it was the commonly used grade for reinforcing bars at that time. Figure 6 shows the cross section of an Aden Road Bridge girder.

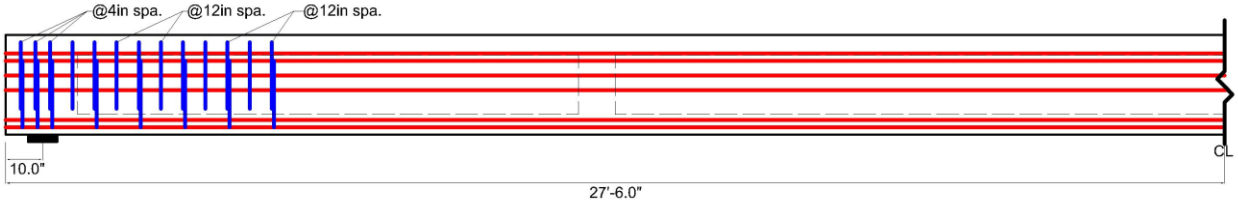

Figure 5 Longitudinal section of the Aden girder

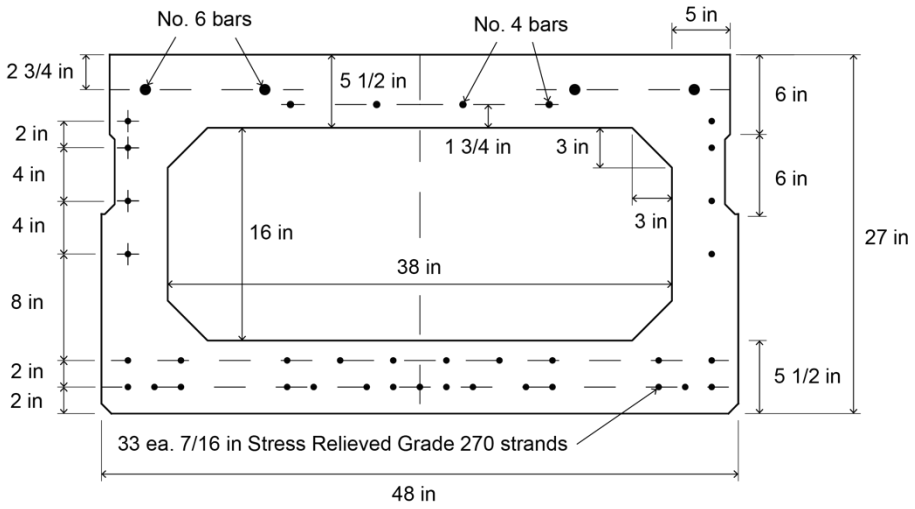

Figure 6 Cross section of the Aden girder (Alfailakawi, 2020)

1.5. Organization of the Thesis

Chapter 2 of this thesis provides a general background on the shear behavior of prestressed concrete beams. It also discusses the shear design methods present in the current AASHTO LRFD and ACI codes. In addition, it reviews, to some extent, some of the relevant literature on the shear topic. Chapter 3 provides a review of the available literature related to the residual shear strength of deteriorated reinforced and prestressed concrete beams. It also presents few studies on the residual flexural strength of deteriorated bridge girders. Chapter 4 discusses the methodology used in this research. It starts with geometric properties of the girders used in this research, material properties, and non-destructive investigation performed. In addition, experimental tests performed in the lab with instrumentation used are described in detail. Finally, results from material tests are presented. Chapter 5 summarizes the results from the experimental tests. Analyses and comparisons between the experimental results and the code predictions are also presented. Chapter 6 outlines the conclusions reached by this investigation and provides some recommendations to enhance future work related to the residual shear strength of corroded prestressed concrete girders.

CHAPTER – 2 BACKGROUND ON SHEAR STRENGTH OF REINFORCED CONCRETE MEMBERS

2.1. Shear Failure Modes and Behavior

There are many types of shear failure modes in reinforced and prestressed concrete beams. These modes include:

- Diagonal tension failure (the diagonal crack extends excessively to separate the member into two pieces)
- Web compression failure (the compressive stresses in the web exceed the concrete crushing strength. The concrete crushing strength is mainly affected by the transverse tension 'Softening')
- Shear compression failure (a flexural-shear crack, or a web shear crack, propagates towards the top of the beam reducing the uncracked, effective, compression area of concrete until it crushes)
- Shear tension (bond) failure (a secondary crack propagates horizontally from an existing flexural-shear crack or a web shear crack along the longitudinal reinforcement which leads to a loss of the bond between concrete and reinforcement)
- Horizontal shear failure (a horizontal shear failure can happen at the interface between the beam and the deck or between the web and the flexural tension flange. The latter type of failure usually occurs in deep beams with thin webs)

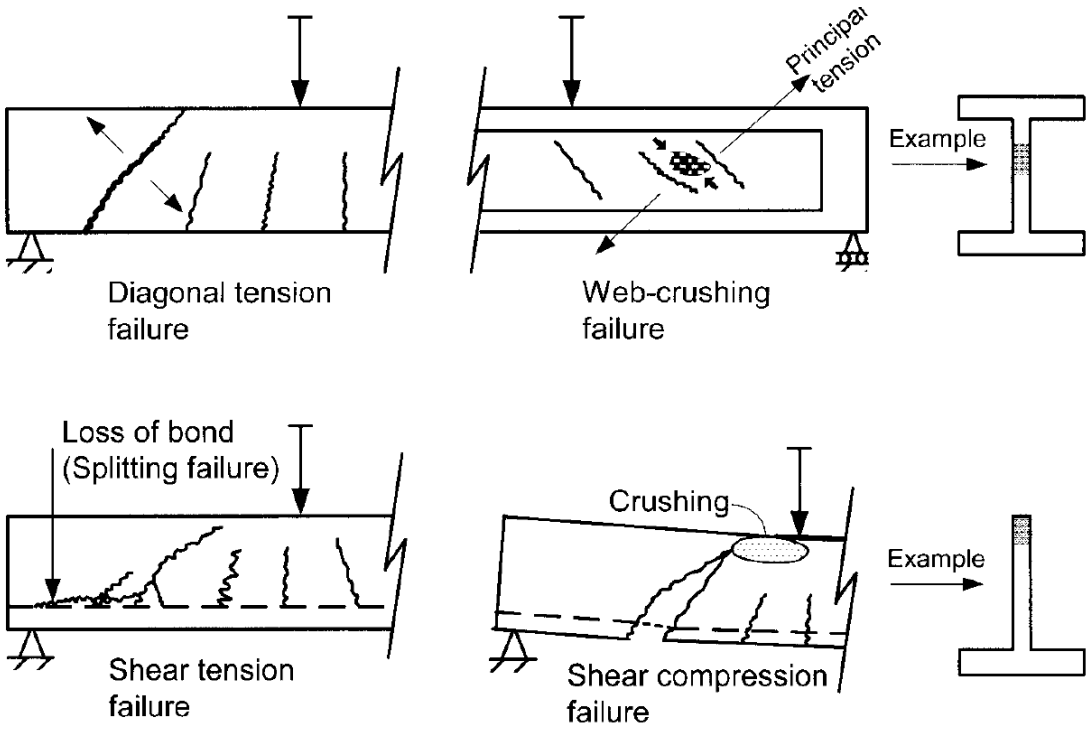

Figure 7 Major shear failure modes (Naaman, 2012)

Two types of shear cracks form in beams subjected to vertical loadings. The first type is the web-shear crack. This crack initiates in the web and is formed when the diagonal tension caused by shear exceeds the cracking strength. Therefore, this type of cracks usually observed near the ends and inflection points of beams, where the shear force is high and the moment is low, with thin webs and high level of prestressing force. The second type of shear-related cracks is the flexural-shear crack. This crack occurs due to both flexure and shear. It initiates as a flexural crack in the tension side; then it transforms into an inclined crack propagating towards the applied load. When the flexural crack occurs, the shear stresses, and diagonal tension, increase at the tip of the crack due to redistribution of stresses, which transforms the crack into a flexural-shear crack. It is also important to mention that the shear cracks in prestressed concrete beams are generally shallower when compared to those of non-prestressed concrete beams. Figure 8 illustrates the shear-related cracks in concrete beams.

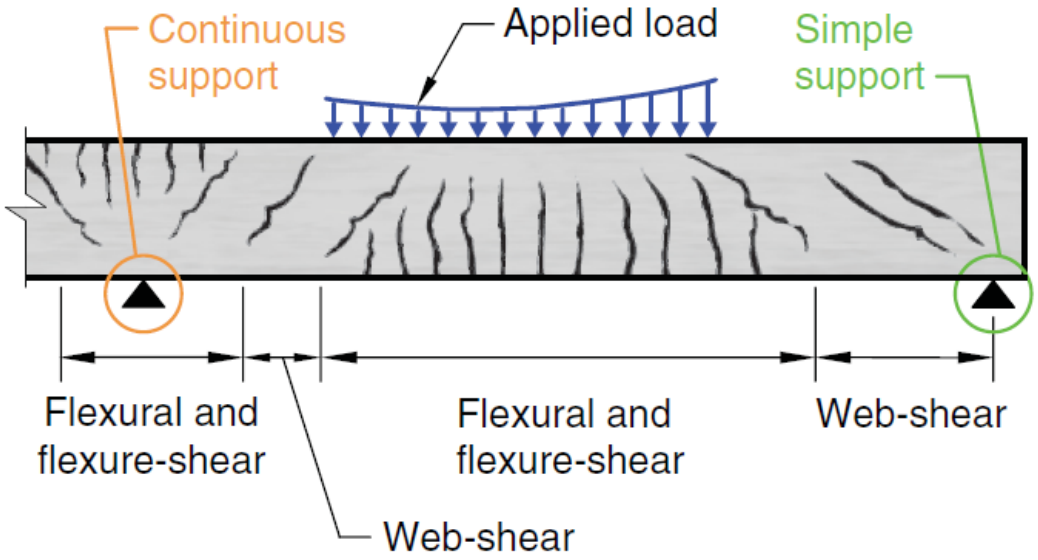

Figure 8 cracks in beams (from ACI318-19)

2.2. Shear Strength for Reinforced Concrete Beams Using Sectional Methods

In sectional shear design methods, the nominal shear strength, V_n, for a reinforced concrete section can be expressed as the summation of three contributions provided by the section components as follows

$$V_n = V_c + V_s + V_p \quad (1)$$

where V_c is the nominal shear strength contribution provided by the concrete, V_s is the nominal shear strength contribution provided by the web reinforcement, usually made up of stirrups or bent-up bars, and V_p is the nominal shear strength contribution provided by the vertical component of the effective prestressing force if the tendon is harped or draped. The latter contribution can be determined as follows

$$V_p = P_e \tan\theta \quad (2)$$

where P_e is the effective prestressing force which can be obtained by multiplying the effective prestress f_{se} by the total area of the tendon, and θ is the inclination angle between axis of the tendon at the section under consideration and the horizontal axis.

Prestressed concrete beams generally require a smaller amount of shear reinforcement compared to non-prestressed concrete beams. This fact can be attributed to

two major reasons. First, if the tendon is draped or harped, the vertical component of the prestressing force, V_p, adds a mechanism to resist shear. Sometimes, V_p is included in the demand side of the strength design equation, that is $\varphi V_n \geq V_u$, by assuming that the web is subjected to a net shear force equal to V_u- V_p. Second, the compressive axial stress provided by the prestressed tendon reduces the magnitude of the principle diagonal tension; and reduces the principle angle, θ, less than 45 degrees. The reduction in the magnitude of the diagonal tension will lead to a higher shear force required to crack the web, V_c. Additionally, the shallower angle of inclination, θ, means a higher number of stirrups through which the crack will cross. This will lead to an increase in V_s.

The transverse steel contribution to the shear strength, V_s, is determined from the fixed 45-degree truss model (Ritter, 1899; Morsch, 1909). In this model, it is assumed that the steel has yielded when the shear failure occurs. V_s is given as follows

$$V_s = \frac{A_v f_y d_v}{S} \tag{3}$$

Conversely, in the sectional design method, V_s, is determined from the variable-angle truss model. The only difference in V_s is that the right-hand side of Eq.(3) is multiplied by $\cot \theta$ to account for the fact that the horizontal projection of the cracked surface is equal to $d_v \cot \theta$.

$$V_s = \frac{A_v f_y d_v}{S} \cot \theta \tag{4}$$

2.2.1. Vci-Vcw Method (ACI318-19)

This method is presented in the ACI and a similar method had existed in the AASHTO until the current version of the code emerged. It should be mentioned that this method is referred to as the V_{ci}-V_{cw}, or the ACI, method in this document. Before the Modified Compression Field Theory emerged, the V_{ci}-V_{cw} method had been the dominant shear design method for prestressed concrete members since the 1960's. This method is used to provide the concrete contribution to the nominal shear strength, V_c based on the diagonal tensile strength of concrete. As mentioned previously in section 2.1 of this document, the concrete shear strength can be dominated by either the web shear crack, which is initiated by a diagonal crack in the web due to the principle diagonal tension, or

the flexural-shear crack, which is initiated as a flexural crack. The concrete contribution to the nominal shear strength is limited to the smaller of the web shear cracking strength, V_{cw}, and the flexural-shear cracking strength, V_{cw}.

2.2.1.1. Vcw

V_{cw} is derived from the principle stresses of an element under biaxial stress state located at the centroidal axis of the section, which has no applied longitudinal stress due to external loadings for a non-composite section. In Figure 9, the principle tensile stress can be calculated using the following equation

$$\sigma_1 = \frac{f_{pc} + f_v}{2} + \sqrt{v^2 + \left(\frac{f_v - f_{pc}}{2}\right)^2} \tag{5}$$

where σ_1, σ_2 are the principle tensile and compressive stresses, respectively. f_{pc} is the compressive stress applied on the element due to the prestressing force and externally applied moment in x-direction, f_v is the compressive stress applied on the element due to the vertical loadings in y-direction. However, in Euler-Bernoulli beam theory, f_v is negligible which is what we will assume here. Finally, θ is the principle stresses angle and v is the shear stress applied on the element.

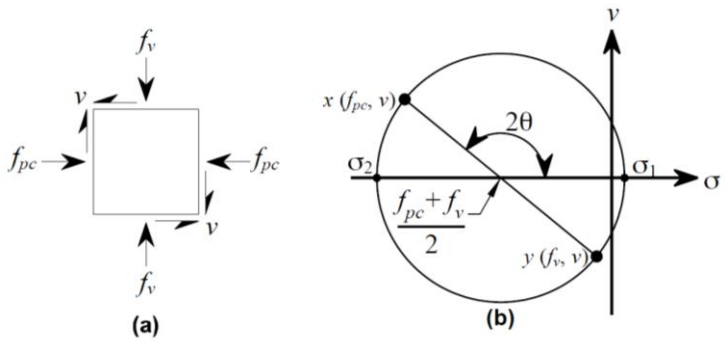

Figure 9 (a) element under biaxial stress state. (b) Mohr's circle for element under biaxial stress state (Kassner, 2012)

By neglecting f_v, Eq. (5) becomes

$$\sigma_1 = \frac{f_{pc}}{2} + \sqrt{v^2 + \left(\frac{f_{pc}}{2}\right)^2} \tag{6}$$

V_{cw} is now derived by equating the right-hand side of Eq. (6) to the cracking strength of the concrete, σ_{cr}. Based on tests, σ_{cr} is taken conservatively as $4\sqrt{f`_c}$ to account for the tension softening due to the transverse diagonal compressive stress. ACI takes $\sigma_{cr}$ conservatively as $3.5\sqrt{f`_c}$. By substituing $3.5\sqrt{f`_c}$ for σ_1 in Eq. (6) then solving for v, we obtain

$$v_{cw} = 3.5\sqrt{f`_c}\sqrt{1+\left(\frac{f_{pc}}{3.5\sqrt{f`_c}}\right)} \quad (7)$$

Note that Eq. (7) is a nonlinear equation for the independent variable f_{pc}. For simplicity, the ACI 318 simplifies the equation to

$$v_{cw} = 3.5\lambda\sqrt{f`_c} + 0.3f_{pc} \quad (8)$$

where λ is added in Eq. (8) to account for the light concrete shear strength. Finally, v_{cw} is taken as the average shear stress $\frac{V_{cw}}{b_w d}$ which can be plugged into Eq. (8) to solve for V_{cw}

$$V_{cw} = \left(3.5\lambda\sqrt{f`_c} + 0.3f_{pc}\right)b_w d_p + V_p \quad (9)$$

where d_p is not taken less than $0.8h$.

Eq. (7) through (9) takes the diagonal cracking strength of the concrete to be proportional to the square root of the concrete compressive strength, $f`_c$. However, Carino & Lew (1982) points out that the actual diagonal tensile strength is proportional to $f`_c$ taken to the power of 0.73 instead of 0.5 for concrete with compressive strength less than 10 ksi. This increase in the power leads to an increase in the tested V_{cw} compared to the calculated V_{cw}, which means a more conservative V_{cw} for concrete with higher $f`_c$, using the ACI formula, presented in Eq. (9) here. The increase of the power is explained in a research conducted by Elzanaty et al. (1986). According to Elzanaty et al. (1986), as the concrete compressive strength increases, the diagonal compressive stress decreases which will in return increase the diagonal tensile strength of the concrete. These findings are not accounted for when Eq. (9) was derived.

Note that $f`_c$ in Eq. (7) through Eq. (9) is taken in psi unit. In addition, for a composite section, f_{pc} is calculated at the centroid of the composite section, or at the

junction of web and flange, due to both prestressing force and externally applied moment carried by the precast member only, that is

$$f_{pc} = \frac{-P_e}{\mathrm{A}} + \frac{P_e e(y_{comp} - y_{bare})}{I} + \frac{-M_D(y_{comp} - y_{bare})}{I} \qquad (10)$$

where *e* is the distance between the centroid of the tendon and the centroid of the bare beam, y_{comp} and y_{bare} are the distance between the bottommost fiber and the centroid of the composite section and the non-composite section, respectively, and M_D is the moment due to a portion of externally applied loadings carried by the bare beam alone, usually due to the bare beam and deck weights.

2.2.1.2. Vci

V_{ci} is the total shear required to form a critical flexural-shear crack. As mentioned in section 2.2.1, a flexural-shear crack is initiated as flexural crack on the tensile side of the beam. Due to redistribution of internal stresses, shear stress, and thus, diagonal tension become high at the tip of the flexural crack leading to a flexural-shear crack. The mathematical expressions for V_{ci} in ACI code are primarily based on early work done by MacGregor et al. in the 1960s. The sequential stages of forming a critical flexural-shear crack is presented in the following paragraph.

Tests have shown that the shear failure is triggered by a critical flexural-shear crack that has a horizontal projection of at least *d* from the critical section X. After the first flexural crack is formed at *d* from the section X, failure will be impending when another flexural crack forms at *d/2* from the section X. Finally, an additional increment of shear is required to transform the flexural crack into a flexural-shear one. Therefore, V_{ci} can be calculated as the sum of the pre-existing dead-load shear, the external-load shear at the instance of the second flexural crack located at *d/2* from the section under consideration, X, and an additional increment of shear required to develop a diagonal shear crack. Figure 10 illustrates the idealized critical flexural-shear crack, where V_{cr} and M_{cr} are the shear and moment at d/2 from the section X when the second flexural crack develops; V and M are the shear and moment at the section X when the second flexural crack develops.

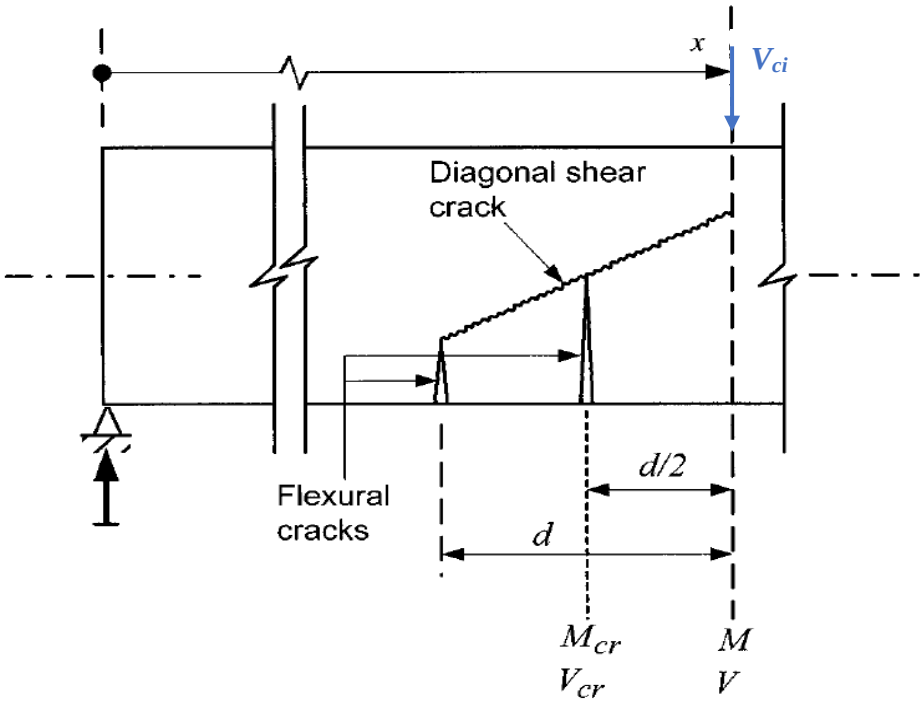

Figure 10 Idealization of the critical flexural-shear crack (Naaman, 2012)

From Figure 10, V_{cr} can be calculated as

$$V_{cr} = V = \frac{M_{cr}}{\frac{M}{V} - \frac{d}{2}} \tag{11}$$

In Eq.(11), the difference in shear between the two sections is assumed to be negligible. In addition, the ratio *M/V* is constant at all loading stages. Therefore, the value of *V* needs not to be known, of course. Now, V_{ci} can be estimated as follows

$$V_{ci} = V_d + V_{cr} + 0.6\lambda\sqrt{f`_c}\,b_w d_p \tag{12}$$

where V_d is the pre-existing shear force due to dead loads, $0.6\lambda\sqrt{f`_c}\,b_w d_p$ is the additional shear, from tests, required to develop a flexural-shear crack. In 1971, the ACI conservatively simplified Eq. (11) by dropping the term *d/2*

$$V_{ci} = V_d + M_{cre}\frac{V_i}{M_{max}} + 0.6\lambda\sqrt{f`_c}\,b_w d_p \geq 2.0\lambda\sqrt{f`_c}\,b_w d_p \tag{13}$$

where

$$M_{cre} = \frac{I}{y_t}\left[6\lambda\sqrt{f`_c} + f_{pe} - f_d\right] \tag{14}$$

V_i *Shear due to externally applied loads including the superimposed dead loads at the section in question,* $V_i = V_u - V_d$

M_{max} *Moment due to externally applied loads including the superimposed dead loads at the section in question,* $M_{max} = M_u - M_d$

M_{cre} *Cracking moment due to externally applied loads at the extreme tension fiber*

f_{pe} *Concrete compressive stress due to prestressing force at the extreme tension fiber*

f_d *Tensile stress due to unfactored dead loads (seflf-weight) at the extreme tension fiber*

$6\lambda\sqrt{f`_c}$ *Conservatively assumed modulus of rupture*

Tests have shown that the tested V_{ci} can be smaller than the calculated V_{ci} using the ACI formula, which means a less conservative V_{ci}. Elzanaty et al. (1986) shows in their study that as the concrete compressive strength increases, the additional shear stress required to transform a flexural crack into a flexural-shear crack decreases instead of being constant as implied by the ACI V_{ci} formula. One reason for this decrease is the fact that the crack surface is smoother for high strength concrete because the crack forms through the aggregate. This smoothness leads to higher stresses at the top of the flexural-shear cracks.

2.2.2. AASHTO Sectional Design Method

The AASHTO Sectional Design method is based on the modified compression field theory, simply denoted as MCFT, developed by Vecchio & Collins (1986) and then simplified for design implementation by Collins et al. (1996). This method has been presented in the AASHTO since 1994. The MCFT describes the behavior of a diagonally cracked concrete subjected to in-plane shear.

The main target of the MCFT is to determine the coefficient β and the angle of principle compressive stress, θ, which directly govern the contribution of the concrete and the steel to the shear strength, respectively. These two factors are determined using an iterative process, which was unliked by many design engineers. Therefore, simplification, of course, with higher level of conservatism, and design tables have been established by the 2004 Canadian Standards Association to facilitate the use of this method in design.

Modified Compression Field Theory (MCFT)

Collins et al. (1996) investigated the behavior of diagonally cracked concrete by conducting tests on many reinforced concrete panels subjected to pure in-plane shear. Unlike the variable-angle truss model, the MCFT accounts for the fact that diagonally cracked concrete can still carry tensile stresses between cracks. This fact combined with equilibrium, stain compatibility equations, and average stress-strain relations lead to an exact solution for the concrete and steel contributions to the shear strength. From a diagonally cracked concrete subjected to biaxial stress state, the following strain compatibility equations can be proven from Mohr's circle for a diagonally cracked web

$$tan^2\theta = \frac{\varepsilon_x - \varepsilon_2}{\varepsilon_t - \varepsilon_2} \quad (15)$$

$$\varepsilon_1 = \varepsilon_x + \varepsilon_t - \varepsilon_2 \quad (16)$$

$$\varepsilon_1 = \varepsilon_x + (\varepsilon_x - \varepsilon_2)cot^2\theta \quad (17)$$

where ε_x, ε_t are the average longitudinal and transverse strains, respectively. ε_1, ε_2 are the average tensile and compressive principle strains, respectively. θ is the angle of the diagonal compressive stresses from the horizontal axis, assumed to be equal to the angle of the diagonal cracks. It should be noted that the previously mentioned strains are averaged over more than one diagonal crack to simplify the actual complex stress variations.

Figure 11 demonstrates the stresses in a diagonally cracked reinforced concrete web and in web reinforcement. From the free body diagram in Figure 11 (a), it can be seen that the concrete tensile stress is varying along the depth with its maximum values

between the cracks and minimum values at the cracks. However, f_1 and f_2 are taken as a average values over enough length in the following equations.

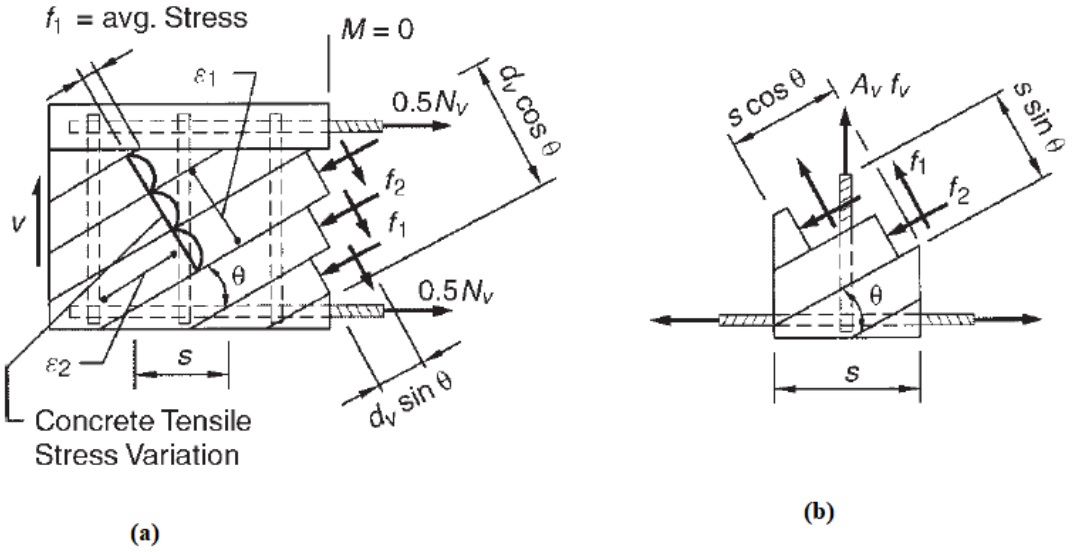

Figure 11 (a) stresses in diagonally cracked reinforced concrete. (b) stresses in web reinforcement (Barker & Puckett, 2013)

By taking equilibrium of the vertical forces in Figure 11 (a) and (b), the following expression is obtained

$$V = f_1 b_v d_v \cot\theta + \frac{A_v f_y d_v}{S}\cot\theta \tag{18}$$

By inspection, Eq.(18) is analogous to Eq.(1) which represents the concrete and steel contributions to the nominal shear strength. Therefore,

$$V_c = f_1 b_v d_v \cot\theta \tag{19}$$

$$V_s = \frac{A_v f_y d_v}{S}\cot\theta \tag{20}$$

It can easily be noticed that Eq.(20) is the same as the shear resistance obtained from the variable-angle truss model. Now, if we define a factor, β, which indicates the ability of diagonally cracked concrete to transmit tension and shear, as follows

$$\beta = \frac{f_1}{0.0316\sqrt{f`_c}}\ cot\theta \tag{21}$$

Then, Eq.(19) can be rewritten as

$$V_c = 0.0316\beta\sqrt{f`_c}b_v d_v \quad (22)$$

where the constant 0.0316 is added only for the unit of $f`_c$ to be in ksi.

The average tensile principle stress, f_1, and thus, β factor, is related to the average tensile principle strain, ε_1, using the following constitutive relations developed by Collins & Mitchell (1991). It is important to mention that researchers in that study assumed that both principle stresses and principle strains have the same angle, θ. Prior to cracking, f_1 and ε_1 follow this equation

$$f_1 = E_c\varepsilon_1 \quad (23)$$

where E_c is Young's modulus for concrete in compression. For early stages of cracking, f_1 is related to ε_1 through the following equation suggested by Collins & Mitchell (1991).

$$f_1 = \frac{4(0.0316)\sqrt{f`_c}}{1+\sqrt{500\,\varepsilon_1}} \quad (24)$$

where $4(0.0316)\sqrt{f`_c}$ is cracking strength of concrete in tension (ksi), denoted as f_{cr}. Again, Eq.(24) is based on the average stress and strain, and thus, does not capture the effect of local stresses at a diagonal crack's surface shown in Figure 12 (c). Therefore, this equation is only valid at early stages of cracking.

As the crack becomes wider and wider, at a crack location, the tensile stresses in the reinforcement becomes higher, until reaching the yield stress, while the tensile stresses in the concrete drop to zero. However, the concrete tensile stresses build up again due to bond as we move towards a plane that is parallel but away from crack surfaces, Figure 12 (a). At a crack location, the concrete carries only shear stresses provided by aggregate interlock and a small amount of local compressive stresses that can be neglected (Vecchio & Collins, 1986). Figure 12 demonstrates the stresses between and at diagonal cracks.

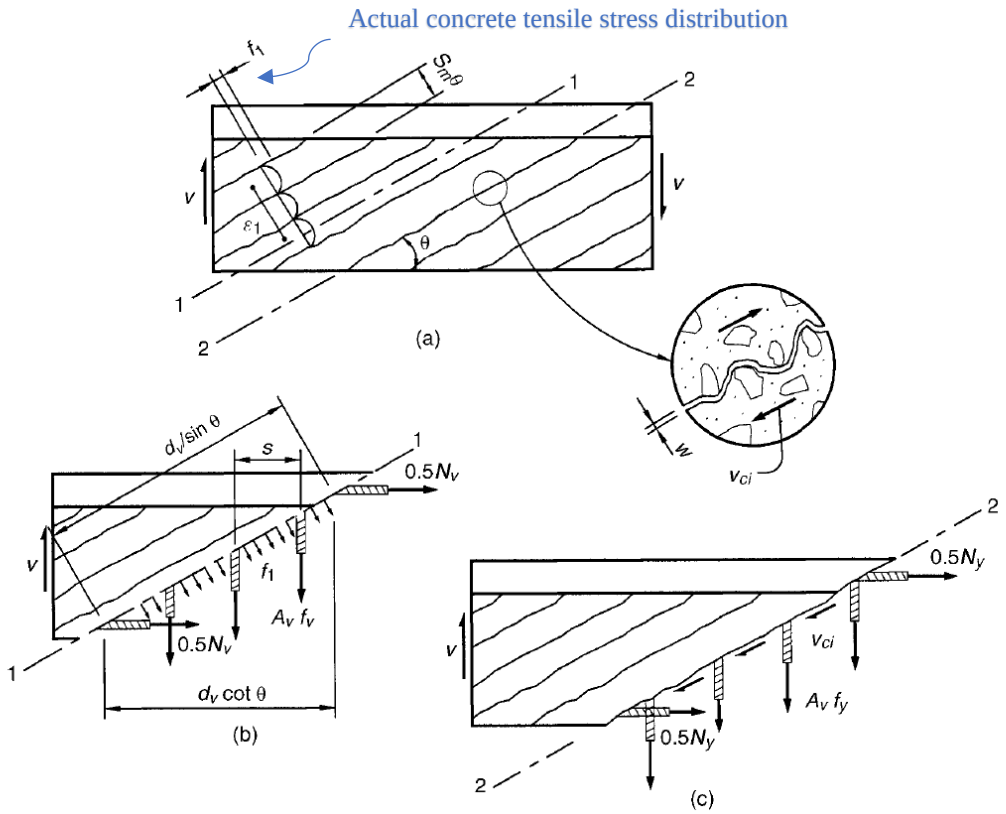

Figure 12 Stresses in a cracked reinforced concrete web. (a) cracked web. (b) stresses between cracks. (c) stresses at a crack. (Barker & Puckett, 2013)

The stresses in Figure 12 (b) and (c) are statically equivalent. Therefore, to satisfy the vertical forces equilibrium, the following condition, obtained after some manipulation, must be met

$$f_1 \leq v_{ci} \tan\theta + \frac{A_v}{b_v s}(f_y - f_v) \qquad (25)$$

After yielding the shear reinforcement, $f_v = f_y$, any further increase in the applied shear is resisted by the shear stress along the crack interface only, v_{ci}, assuming elastoplastic material law for the shear reinforcement. Eq.(25) limits the average tensile principle stress in concrete, f_1, to a certain value to ensure that it can be equilibrated locally by the steel and the interfacial shear stress mechanisms at the crack. This is referred to as *The Crack Check* (Bentz, 2000).

The maximum interfacial shear stress that can be transmitted by the aggregate interlock without slipping depends on the crack opening, maximum aggregate size, and crack spacing. Using the data of statistical work done by Walraven (1981), Vecchio &

Collins (1986), the amount of shear stress that can be transmitted across a crack was limited to the following value, which was simplified by Collins & Mitchell (1991).

$$v_{ci} = \frac{2.16(0.0316)\sqrt{f`c}}{0.3+\frac{24w}{a+0.63}} \tag{26}$$

where 'w' is the crack opening width, which can be taken as $\varepsilon_1 S_\theta$, 'a' is the maximum aggregate size, and 'S_θ' is the average spacing of the diagonal cracks. Collins & Mitchel (1991) used a value of 12in for 'S_θ' and 0.75in for 'a' which can be substituted into Eq.(26) to obtain the following

$$v_{ci} = \frac{2.16(0.0316)\sqrt{f`c}}{0.3+200\varepsilon_1} \tag{27}$$

Now, by plugging Eq.(27) into Eq.(25) while assuming steel yields before concrete slips along the crack interface, we obtain an upper bound value for f_1

$$f_1 \le v_{ci}\tan\theta + \frac{A_v}{b_v S}(f_y - f_v) \underset{f_v=f_y}{\Longrightarrow} f_1 \le v_{ci}\tan\theta \tag{28}$$

To summarize, Figure 13 shows the constitutive relations of all stages of cracking.

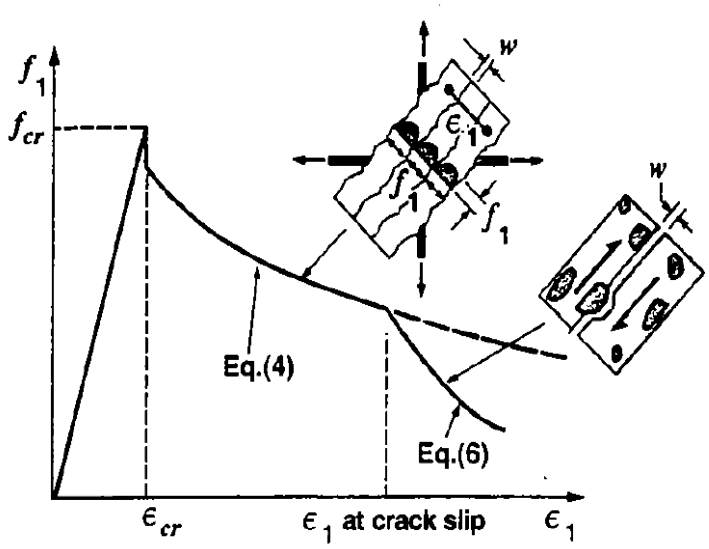

Figure 13 Constitutive relations for a cracked reinforced concrete (Collins & Mitchell, 1991)

From Eq.(21), (24), and (28), β for a cracked reinforced concrete is controlled by

$$\beta = \frac{4\cot\theta}{1+\sqrt{500\,\varepsilon_1}} \le \frac{2.16}{0.3+200\varepsilon_1} \tag{29}$$

Now, the remaining goal is to find a closed-form solution for the average tensile principle strain ε_1. Before doing so, it is important to mention that crushing of the

diagonal compressive strut is another potential failure mode that can occur, especially for thin-web girders, prior to yielding the shear reinforcement and slipping of the concrete along the crack plane. This mode of failure is very brittle and should be avoided in the design process. The AASHTO LRFD limits the shear force resisted by both concrete and shear reinforcement to prevent the diagonal web-crushing failure

$$V_{n,max} = 0.25\sqrt{f`_c}b_v d_v + V_p \tag{30}$$

Another important constitutive relation is the one that relates the average compressive stress, f_2, to the average tensile principle strain, ε_1 for concrete under biaxial state of stress. Unlike uniaxial state of stress, the presence of the principle tensile strain, ε_1, softens the principle compressive stress in concrete, f_2, which is called as compression softening. Vecchio & Collins (1986) suggested a mathematical expression for this phenomenon given in Eq.(31) in this document.

$$f_2 = \beta_o f`_c \left[2\left(\frac{\varepsilon_2}{\varepsilon_{peak}}\right) - \left(\frac{\varepsilon_2}{\varepsilon_{peak}}\right)^2\right] \tag{31}$$

$$\beta_o = \frac{1}{0.8+170\varepsilon_1} \leq 1 \tag{32}$$

where ε_{peak} is the compressive principle strain corresponding to $f`_c$ and can be taken as 0.002. $\beta_o$ is the compression softening factor that is a function of the average tensile principle strain, $\varepsilon_1$. The term $\beta_o f`_c$ is the reduced crushing strength of the concrete under biaxial state of stress. From Eq.(31) and Eq.(32), it can be noticed that the higher the transverse strain, the lower the compressive stress in concrete.

From vertical forces equilibrium of the free body diagram in Figure 11 (a), the following relation between f_1 and f_2 is obtained

$$f_2 = \frac{V}{b_v d_v \sin\theta \cos\theta} - f_1 \tag{33}$$

where the second term of the right-hand side of Eq.(33) can conservatively be dropped as it is very small compared to the first term. Solving for ε_2 in Eq.(31) while taking f_2 from Eq.(33), then plugging the resulted quantity in Eq.(17) will lead to the closed-form solution for the average tensile principle strain ε_1

$$\varepsilon_1 = \varepsilon_x + \left[\varepsilon_x + 0.002\left(1 - 1 - \sqrt{\frac{V}{b_v d_v f`_c}\frac{0.8+170\varepsilon_1}{\sin\theta\cos\theta}}\right)\right]cot^2\theta \tag{34}$$

Because the axial strain at the centroid of the flexural tension side of the section, ε_s, is much higher the one o the flexural compression side, the AASHTO estimates ε_x to be equal to one-half of ε_s,[A5.7.3.4.2-4 and B5.2-4] , as shown in Figure 14.

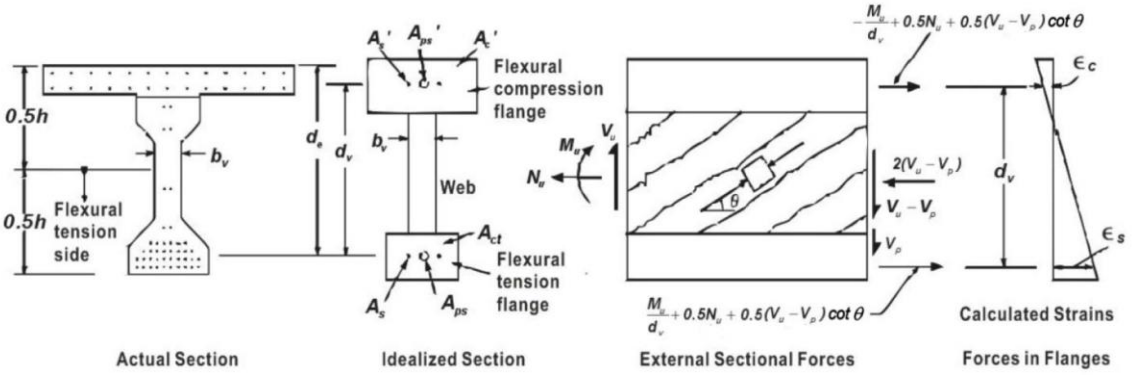

Figure 14 Axial forces on each component of the idealized section under V, N, and M (AASHTO LRFD)

$$\varepsilon_x \approx \frac{\varepsilon_s}{2} = \begin{cases} \dfrac{\frac{|M_u|}{d_v}+0.5N_u+0.5|V_u-V_p|\cot\theta-A_{ps}f_{po}}{2\left(E_sA_s+E_{ps}A_{ps}\right)}, & \varepsilon_x \geq 0 \\ \dfrac{\frac{|M_u|}{d_v}+0.5N_u+0.5|V_u-V_p|\cot\theta-A_{ps}f_{po}}{2\left(E_sA_s+E_{ps}A_{ps}+E_cA_{ct}\right)}, & \varepsilon_x < 0 \end{cases} \quad (35)$$

where f_{po} is the Young's modulus of the prestressed strands multiplied by the locked-in difference in strain between concrete and the strands. This value should be adjusted for sections within the transfer length, l_t.

From previous discussion, it can be noticed that obtaining the nominal shear strength is an iterative procedure. For a guessed value of θ, β factor can be determined from Eq.(29), and then V_s and V_c can be calculated using Eq.(20) and Eq.(22), respectively. This process is cumbersome and needs many iterations on the angle θ. The following subsections present a relatively simpler way of obtaining θ and β that can be conducted using simple hand-calculations for prestressed concrete members.

Before presenting the two approaches, it is important to mention that the sectional analysis for shear assumes that the shear stress in concrete is uniformly distributed over an area of b_v times d_v and the angle of the principle compressive stresses is constant over the depth d_v. In addition, average principle stresses and strains are collinear, while the average principle compressive stresses are parallel to the cracks, as illustrated in Figure 12.

General Procedure [AASHTO Appendix B5.2]

The general procedure appeared in the 1994 Canadian Standards Association's Design of Concrete Structures (CSA 1994) and then in the 2002 AASHTO LRFD Bridge Design Specification. In this method, the values of θ and β are given in tables based on work originally done by Collins & Mitchel. These values are given in the AASHTO LRFD, table B5.2-1, for sections containing at least the minimum required transverse reinforcement, given in [AASHTO 5.7.2.5] and repeated in Eq.(36) in this document for convenience.

$$A_{v,min} = 0.0316\lambda\sqrt{f`_c}\frac{b_v S}{f_y} \tag{36}$$

Two quantities need to be known at the section under consideration to enter Table B5.2-1. The first one is the axial strain, ε_x, which can be calculated using Eq.(33). The second quantity is the shear stress divided by the concrete compressive strength. For a section containing less than the minimum transverse reinforcement, θ and β are given in Table B5.2-2. Beside calculating ε_x, one needs to estimate the crack spacing parameter, S_{xe}, to enter Table B5.2-2, which is given here in Eq.(37).

$$S_{xe} = S_x\frac{1.38}{a+0.63} \leq 80in \tag{37}$$

where S_x definition is given in [B5.2], and a is the maximum aggregate size. Finally, the tabulated values of θ and β were established on the basis of ensuring that the principle compressive stress, f_2, does not exceed the crushing strength of concrete under biaxial state of stress, $\beta_o f`_c$, while the shear reinforcement reaches its full yield stress as stipulated previously in Eq.(28).

For design purposes, the tabulated values of θ and β will generally result in the minimum amount of shear reinforcement. The designer first assumes a value for θ, 30 degrees for example, then calculates ε_x from Eq.(33) using V_u, M_u, N_u, and f_{po} calculated at the section under consideration. The values of θ and β can then be determined from Table B5.2-2 or Table B5.2-2. This process is repeated using the new obtained value of θ until it converges.

Simplified Procedure [AASHTO 5.7.3.4.2]

In lieu of the iterative procedure described in the General Procedure [AASHTO Appendix B5.2], a more straightforward procedure has been accepted by the AASHTO since 2008. The simplified procedure is similar to the one in the 2004 Canadian Standards Association's Design of Concrete Structures (CSA 2004). Hawkins et al. (2005) developed explicit mathematical expressions for θ and β based on the MCFT, which was found to be appropriate for shear design in the LRFD Bridge Design Specification.

The axial strain at the centroid of the reinforcement, ε_s, is estimated using the idealized sectional model in Figure 14.

$$\varepsilon_s = \begin{cases} \dfrac{\frac{|M_u|}{d_v}+0.5N_u+|V_u-V_p|-A_{ps}f_{po}}{E_sA_s+E_{ps}A_{ps}}, & \varepsilon_s \geq 0 \\ \dfrac{\frac{|M_u|}{d_v}+0.5N_u+|V_u-V_p|-A_{ps}f_{po}}{E_sA_s+E_{ps}A_{ps}+E_cA_{ct}}, & \varepsilon_s < 0 \end{cases} \tag{38}$$

Eq.(38) is similar to Eq.(35) except that in the former, $0.5cot\theta$ is taken equal to 1. β is determined using Eq.(39) for sections that contains at least the minimum required transverse reinforcement.

$$\beta = \frac{4.8}{1+750\varepsilon_s} \tag{39}$$

For sections that contains less than the minimum required transverse reinforcement, Eq.(40) is used.

$$\beta = \frac{4.8}{1+750\varepsilon_s}\frac{51}{39+S_{xe}} \tag{40}$$

The angle θ is determined using Eq.(41)

$$\theta = 29 + 3500\varepsilon_s \ (degree) \tag{41}$$

Note that the simplified procedure reduced the computational effort needed in shear design when following the General procedure with tabulated values of θ and β. This is because θ and β are now given explicitly as functions of ε_s only. In addition, Eq.(38) no longer contains θ. However, the simplified procedure is still an iterative process when calculating the nominal shear strength of a section. This is clear in Eq.(38) as it contains the applied shear force, V_u, which is our unknown in the analysis.

Demand on the longitudinal reinforcement

Shear causes additional tensile force at the bottom flexural tension side that needs to be resisted by the longitudinal reinforcement if the member is not subjected to an axial force. This consideration is crucial and can lead to slipping of the longitudinal steel if not appropriately checked especially near the ends of simply supported beams where the shear demand is high.

The tensile force demand on the longitudinal reinforcement due to shear can be determined by summing moments about point 'O' in the free body diagram in Figure 15

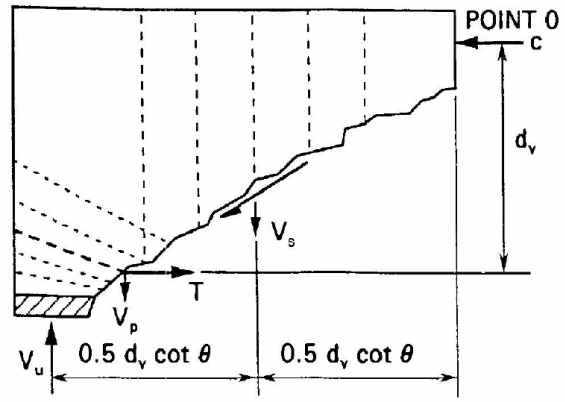

Figure 15 Longitudinal reinforcement demand (AASHTO LRFD)

It is assumed that the moment caused by V_c about point 'O' is small and can be neglected. In addition, the moment arms for both V_u and V_p are equal to $d_v \cot \theta$. This will lead to the following requirement, which is given in AASHTO LRFD for member not subjected to torsion.

$$T = A_s f_y + A_{ps} f_{ps} \geq \left(\frac{V_u}{\varphi_v} - 0.5V_s - V_p\right) \cot\theta \qquad (42)$$

where, A_s and f_y are the area and the yield stress of the non-prestressed steel in the flexural tension side, respectively. A_{ps} and f_{ps} are the area and the average stress at ultimate of the prestressed strands in the flexural tension side, respectively. φ_v is the strength reduction factor for shear. According to the AASHTO LRFD [C.5.7.3.5], the right-hand side of Eq.(42) may be evaluated at d_v from the inside edge of the support. Finally, f_y and f_{ps} should be adjusted for any undeveloped reinforcement. For non-prestressed steel, the stress is assumed to build up linearly from zero to f_y within the

development length. For prestressed strands, the stress is assumed to build up linearly from zero to f_{se} within the transfer length, and from f_{se} to f_{ps} within the development length minus the transfer length as shown in Figure 16.

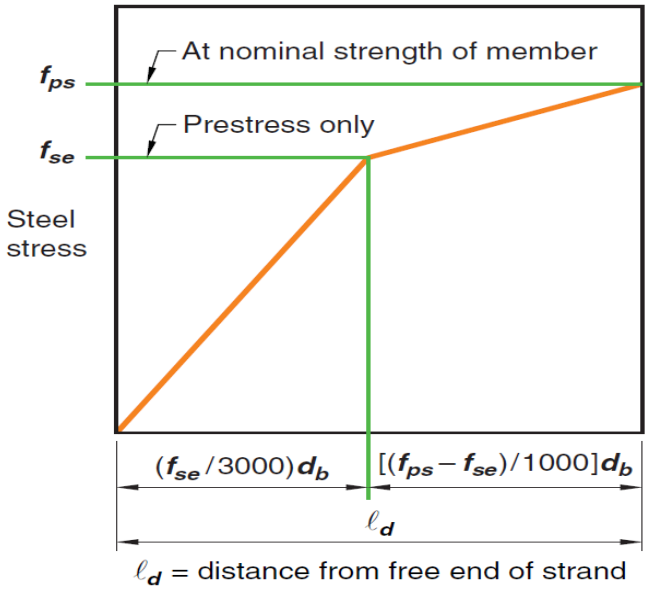

Figure 16 Bilinear strand stress idealization along its length (ACI318-19)

2.2.3. Strut and Tie Model

Strut and tie model, STM, for a structural system is represented by a truss that provides a rational path of the flow of forces while satisfying the lower bound theorem of plasticity. It is a useful tool for shear and torsion design of members especially for regions where bending theory assumptions do not apply. These regions are referred to as *disturbed regions*, or simply *D-regions*. STM idea evolved from the early developed truss model by Ritter and then Morsch in the late 1890s and early 1990s that represents the behavior of a cracked concrete subjected to shear. Then, guidelines were introduced to STM by Schlaich et al. (1987). Later, it was incorporated into the 1993 AASHTO LRFD and the 2002 ACI code. In the 2019 ACI code, STM has been moved from the appendix to the main body with new modifications which will be mentioned in the context.

The strength obtained from a STM is conservative since it is a lower bound. This is attributed to the lower bound theorem of plasticity where the obtained load is always less than or equal to the actual collapsing load if the assumed collapse mechanism

satisfies both equilibrium and strength (yield criterion). In addition, enough ductility must be provided to ensure that forces can be distributed according to the developed STM (Reineck, 2002). This ductility is usually ensured by providing enough anchorage of the reinforcement and well-distributed reinforcement to control cracking. However, acceptable level of cracking and deflection is not always guaranteed by the STM (Kuchma et al., 2008).

An optimum STM is the one that corresponds to minimum strain energy. Typically, a designer would need to refine the initially assumed STM. Therefore, a rule of thumb is to establish a STM that mimic the flow of stress trajectories from an elastic finite element analysis (Schlaich et al., 1987). In addition, cracking pattern is also another helpful tool to establish a STM. Investigation of STM on bridges with examples is conducted by Williams et al. (2011).

D-regions and Deep beams

According to St. Venant's principle, strains are assumed to be linearly distributed in regions that are *some distance* away from discontinuities. This distance is taken approximately as the depth, *d*, of the member. Therefore, the elastic bending theory assumes that a plane section remains plane in such regions after deformations. These are regions are known as B-regions. On the other hand, D-regions, *disturbed regions,* are regions with load or geometric discontinuity. Concentrated load and reactions are examples of load discontinuity, while abrupt change in the cross section is an example of geometric discontinuity.

When the shear span-to-depth ratio (*a/d*) for a beam is greater than 2, B-region exists within the shear span. Such a beam is called a slender beam. On the other hand, the entire shear span is a D-region when *a/d* is less than 2 and the beam is called a deep beam. In deep beams, the load is transferred to the support through a combination of an arching action, or direct load transfer, and a truss action, or indirect load transfer (Reineck, 2002). These two mechanisms can be both captured in STM by superposition of two determinate trusses as shown in Figure 17. Therefore, STM is a more meaningful tool to use for design and analysis of deep beams.

Much research has focused on the shear strength of deep beams. This includes experimental investigations of the shear strength of deep beams to validate the STM (Aguilar et al., 2002; Maxwell et al., 2000). Regardless of how well the STM predicted the strength, it was less than the experimental strength. This comes as no surprise because the STM provides a lower bound strength as mentioned previously. Most of the STM discussion will be dedicated to deep beams as they are related to this research.

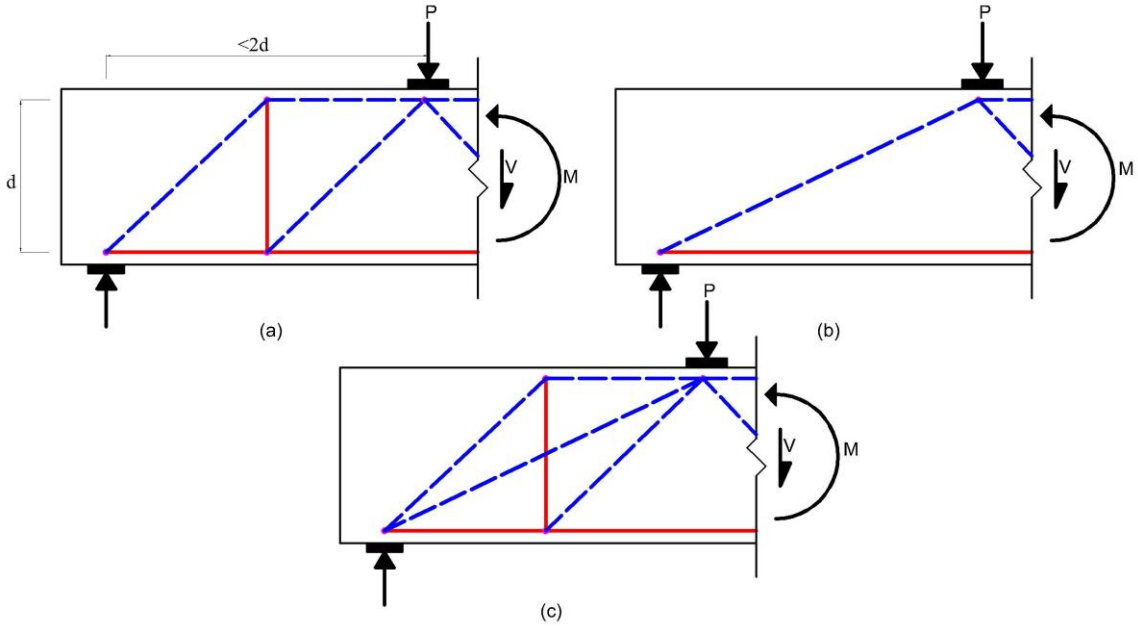

Figure 17 STM for a deep beam. (a) Truss action. (b) Arch action. (c) combined action

Strength of a STM

STM for a structure is represented by a truss, preferably determinate, where compression members are called *struts*, tension members are called *ties*, joints are called *nodes*. Loads are applied at the nodes and struts and ties are uniaxial members. The prestressing force is applied as external loads at the centroid of the tendon. The load-carrying capacity of a STM is governed by the weakest link among its components.

Nodes

Nodes are the intersection zones of ties and struts. A node can be classified as CCC, CCT, and CTT node based on the types of elements intersecting that node, where 'C' stands for compression, that is a strut, and 'T' stands for tension, that is a tie. Figure 18 shows node types and their geometries.

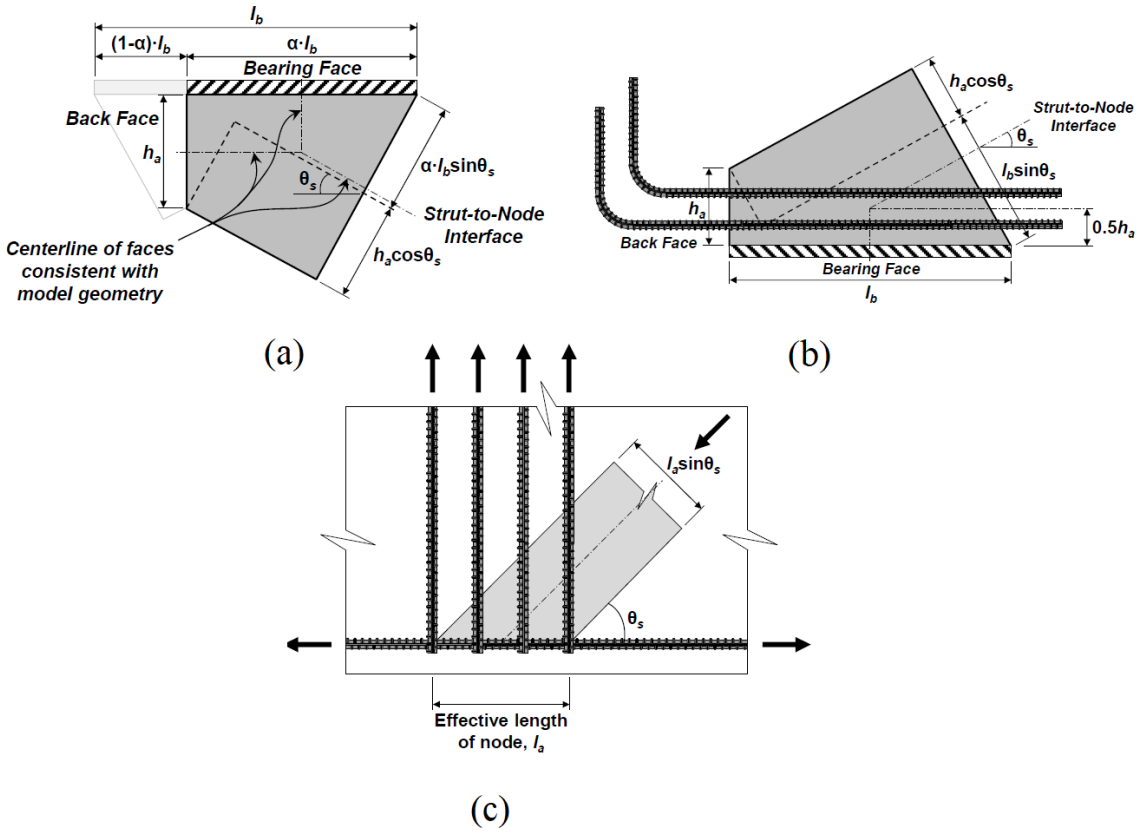

Figure 18 Node Types (a) CCC node. (b) CCT node. (c) CTT node. (AASHTO LRFD)

Nodes are also classified based on the stress at their faces. Nodes bounded by a support or load bearing plate are usually called *discrete nodes*. These nodes have more or less concentrated forces. *Smeared nodes* have stresses that are smeared out over undefined length. Smeared nodes are generally not critical and need not be checked (Schlaich, 1987; Fib, 1999). Therefore, smeared nodes will not be checked for their strength in this research.

The strength of each node face is checked for strength separately. This includes back face, bearing face, and strut-to-node interface. Strength of a node is given in the ACI318-19 as

$$F_{nn} = f_{ce} A_{nz} \quad (43)$$

$$f_{ce} = 0.85 \beta_c \beta_n f`_c \quad (44)$$

where

A_{nz} *Area of the nodal face perpendicular to the line of action of the force applied on the face*

β_c *Confinement modification factor for nodes and struts [ACI318-19 Table 23.4.3(b)]*

β_n *Nodal zone coefficient, depends on the node type [ACI318-19 Table 23.9.2]*

Struts

Struts are compression members in the STM. They are usually made of concrete and compression reinforcement, if provided. Previously, the struts were classified into *prismatic* and *bottled-shape* struts. However, Laughery et al. (2015) suggest that both types of struts have similar strength. In the ACI318-19, struts are renamed to *interior* and *boundary* struts based on their location and the stress field. Interior struts are located in the interior of the member and cross a tensile stress field. On the other hand, boundary struts are present in a uniaxial compressive stress field.

While the AASHTO LRFD does not require the struts to be checked, the ACI code suggests that they need to be checked. According to the ACI commentary, struts are generally assumed to be prismatic. However, it might be difficult to do so for reasons such as different bearing lengths of the nodes connecting the strut. In such a case, it is reasonable to assume a tapered strut between the nodes and check its strength at both ends. The width of the strut is taken as the nodal interface length if the strut axis is perpendicular to the nodal face. Otherwise, the strut width is taken as the width perpendicular to the strut axis. The strut thickness is taken as the width of the member

except at the support where the strut thickness is taken as the member width or the bearing element width, whichever is smaller.

Strength of a strut is given in the ACI318-19 as Eq.(45) in this document. Where the second term accounts for any compression reinforcement along the strut.

$$F_{ns} = f_{ce} A_{cs} + A`_s f`_s \quad (45)$$

$$f_{ce} = 0.85 \beta_c \beta_s f`_c \quad (46)$$

where

A_{cs} *Area of the strut at the end under consideration*

β_s *Strut coefficient [ACI318-19 Table 23.4.3(a)]*

Note that the strut coefficient, β_s, accounts for the fact that the strength of a strut crossed by a transverse tension field is weaker. In addition, it depends on the presence of the distributed reinforcement. Distributed reinforcement controls cracking and provides ductility for force redistribution (Rogowsky et al., 1986).

Ties

Ties are the tension members in the STM. They are resisted by the prestressed and the non-prestressed reinforcement. In fact, concrete can also contribute in resisting the tension force between cracks as the bond exists; However, its contribution is usually neglected. In analysis, the tie axis is placed at the centroid of the reinforcement. The strength of a tie is given in the ACI318-19 as follows

$$F_{nt} = A_{ts} f_y + A_{tp} \Delta f_p \quad (47)$$

where

A_{ts} *Area of non-prestressed reinforcement in the tie*

A_{tp} *Area of prestressed reinforcement in the tie*

Δf_p *Stress increase in the prestressed tendon due to applied loads [ACI318-19 23.7.2.1]*

It should be mentioned that the ACI code treats the effect of the prestressing force in the tendon as an externally applied load on the STM.

Beside strength, ties should also be anchored to develop their strength. This anchorage is provided by mechanical devices, hooks, or straight bar development length.

The critical section for the anchorage check is the intersection of the tie reinforcement and the end of the extended nodal zone as shown in Figure 19.

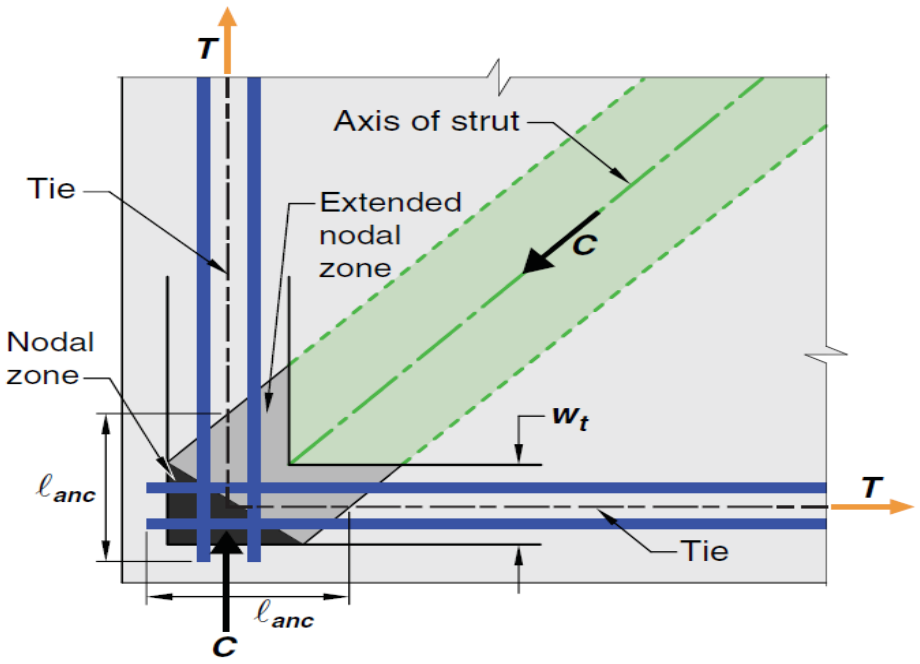

Figure 19 Tie reinforcement detailing (ACI318-19)

Proportioning of a horizontal tie is clear. However, vertical tie proportioning needs further explanation. Vertical tie forces are resisted by the transverse reinforcement, usually in the form of stirrups; sometimes they are made of a transverse prestressing tendon. Generally, vertical ties connect two smeared nodes. Therefore, it is not so clear how to select the width of a vertical tie. Wight and Parra-Montesinos (2003) suggested a technique to estimate the width of a vertical tie. It is based on the assumption that struts spread in a fan-like shape with an angle of no less than 25 degrees of the vertical axis. Therefore, stirrups engaged in carrying the load are those that are spread over a band bounded by the two 25-degree-inclined lines. Transverse reinforcement is to be lumped at the centroid of the vertical tie as shown in Figure 20 (Williams et al., 2011).

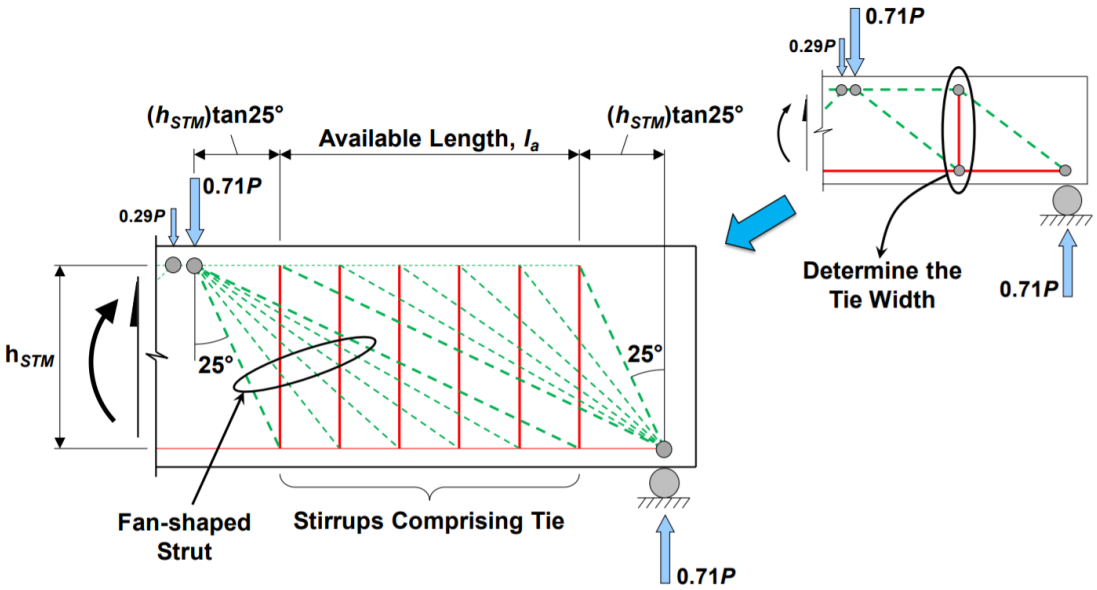

Figure 20 Proportioning of a vertical tie joining two smeared nodes based on Wight and Parra-Montesinos (2003). (Williams et al., 2011)

CHAPTER – 3 LITERATURE REVIEW ON DETERIORATED BRIDGE GIRDERS

3.1. Higgins et al. (2003)

This research was performed in the Oregon State University and sponsored by the Oregon DOT and the Federal Highway Administration to assess the shear capacity of concrete bridge beams with corroded shear reinforcement. Fourteen non-prestressed concrete beams for this study were designed following the 1950's AASHTO provisions. Beams were 10-ft long with 8-ft effective span and had *a/d* of 2.04. Beams were designed in three types of cross-sections, a rectangular section and two different rectangular sections with concrete slab built integrally. Four levels of corrosion were made using an accelerated corrosion procedure. These levels were no corrosion, light, medium, and heavy corrosion. The no-corrosion level was used as a baseline for comparisons. The intended cross-sectional losses of stirrups corresponding the four corrosion levels were 0%, 20%, 40%, and 80%, respectively. After testing, stirrups crossed the failure crack were retrieved and investigated for their actual sectional loss.

Beams were tested in four-point loading condition. During testing, most stirrups with medium and heavy level of corrosion fractured due to significant sectional loss. From test results, beams with light-corroded stirrups achieved 87.7% of the capacity of the beams with no corrosion. Beams with medium-corroded stirrups achieved from 74.2% to 95.2% of the capacity of the beams with no corrosion. Beams with heavy-corroded stirrups achieved from 58.5% to 93.6% of the capacity of the beams with no corrosion. Variation in percentages for each level of corrosion was mainly due to other factors including concrete compressive strength, cross-section geometry, and stirrup spacing. However, corrosion level in stirrups generally correlates with the shear strength loss. In addition, tests generally showed that the ductility decreases as the severity of corrosion increases.

Spacing of corroded stirrups was only studies for rectangular sections. It was found that the shear strength loss due to corroded stirrups is considerably affected by the stirrup spacing. Higgins et al. (2003) pointed out that when corroded stirrups are closely

spaced, corrosion-induced cracks intersect causing delamination and spalling to the concrete cover. This deterioration reduces the concrete contribution to the nominal shear strength, V_c. In addition, closely spaced stirrups provide a higher contribution to the nominal shear strength, V_s. Thus, the corrosion level in closely spaced stirrups influences the residual shear strength more than the corrosion level in widely spaced stirrups.

In these beams, sectional loss of stirrups and corrosion-induced cracks in concrete were apparent. Sectional methods, STM, and FEA were used to calculate the residual shear strength. Sectional loss of stirrups and spalling in concrete due to corrosion-induced cracks were incorporated in these methods. Sectional loss of stirrups was incorporated in calculations by modifying the cross-sectional area of stirrups across a potential shear crack in the V_s term. Damaged, spalled, concrete was incorporated by modifying the effective width of the web in the V_c term. Spacing of corroded stirrups affects the concrete cover as shown in Figure 21.

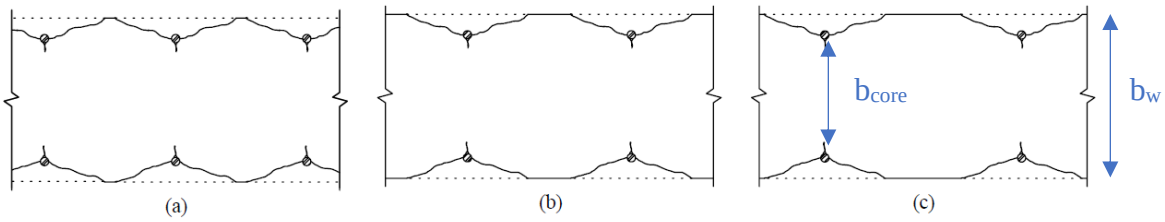

Figure 21 concrete cracking in beam web due to corrosion for three different stirrup spacings. (a) 8in. (b) 10in. (c) 12in. (Higgins et al., 2003)

Angle of spalls was taken as 20 degrees from observation. This modification to the concrete effective width was suggested to be used when stirrups show a sectional loss of more than 10% of their original sectional area.

Sectional method in the ACI code did not predict the shear strengths of the beams very well. It was attributed to the small *a/d* used in their study. Thus, the coefficient for V_c was increased from 2 to 5 which was also suggested by Fereig et al. (1977). Using these modifications, sectional method in the ACI reasonably predicted the residual shear strength with some level of conservatism in most cases. Finally, it was found that corrosion damaged beams, with cover delaminated, did not diagonally crack at a lower

load than the uncorroded ones. They concluded that the concrete cover has less effect than the core on the concrete contribution to the shear strength.

3.2. Runzell et al. (2007)

This research was performed for the MnDOT to evaluate the shear strength of old-designed prestressed concrete bridge girders with the newer design codes. An old bridge girder, which was designed following the 1979 code provisions, underwent two shear tests for its both ends. The goal of this research was to evaluate the shear capacity of bridge girders designed according to the 1979 AASHTO interim, which required lesser amount of shear reinforcement. This evaluation was performed under the light of the 2004 LRFD, 2002 Standard, 1979 Interim, and the STM. The first and second methods are similar to those presented in the current research.

Two ends were cut from a bridge in Minnesota with a length of 30.5ft. The girder was in-service for more than 20 years according to the plans. The girder was I-shaped with a depth of 54 in. and pretensioned with straight and harped strands. Each end was tested in a three-point loading condition with *a/d* of 2.7.

Physical tests indicated that the girder failed at a load higher than what was predicted by the aforementioned shear design provisions. However, the 2002 Standard code was the closest to predict the actual strength. Table 1 shows a comparison between predicted and tested strengths (Runzell et al., 2007). In addition, it was found that if the shear capacity was calculated by adding the V_c term using the 2002 Standard to the V_s term using the 2004 LRFD, the discrepancy between V_{test} and $V_{predicted}$ will be about 6%.

Table 1 Results from Runzell et al. (2007)

		V_{pred} (kips) (Measured material properties)	V_{test} (kips) (Including dead load)	$\frac{V_{test}}{V_{pred}}$
Specimen I (with bridge deck)	2004 LRFD	259	392	1.51
	2002 Standard	316		1.24
	1979 Interim	189		2.07
	Strut and Tie	281		1.40
Specimen II (no bridge deck)	2004 LRFD	204	329	1.61
	2002 Standard	238		1.38
	1979 Interim	157		2.09
	Strut and Tie	246		1.34

3.3. Pei et al. (2008)

Two full-scale prestressed concrete girders in Oklahoma were tested to failure in the University of Oklahoma. The first girder was about 40-year old and was recovered from the I-244 Bridge. The other girder was intended for the Wild Horse Creek Bridge but rejected for a quality control issue. The I-244 had a severely damaged end repaired with glass fiber reinforced polymer, while the other was non-retrofitted. This research was funded by the ODOT to evaluate bridges designed in the 1960's and 1970's which were expected to have experienced some level of deterioration. Girders tested in this research were AASHTO Type II, designed prior to the 1979 AASHTO interim. Similar to Runzell et al. (2007), the goal of this study was to evaluate whether these old bridges were safe in shear or not according to the current provisions. Experimental results were compared against three design provisions and the STM.

Camber measurements and non-destructive flexural tests were first performed to estimate the effective prestress and the flexural stiffness of these girders. Then, shear tests were performed using three-point loading condition. The I-244 Bridge girder was tested on its both ends. Then, the girder was shortened and tested on its both ends again. All shear tests for this girder were performed with *a/d* of approximately 1. The Wild Horse Creek Bridge girder was tested on its both ends once. The first and second tests were performed with *a/d* of approximately 2.5 and 1, respectively.

The retrofitted end of the I-244 Bridge girder failed at a load that was 23% more than the non-retrofitted end with the original girder length. For the Wild Horse Creek Bridge girder, the first test with a higher *a/d* failed in flexure with a load that was about 45% of the load reached in the other end with lower *a/d*.

According to this study, the sectional design methods for shear showed consistent predicted strengths, except the STM which was very conservative. This was due to the limited anchorage for strands. However, tests showed higher experimental shear strengths than what was predicted by the various code provisions including the STM with a wide safety margin. Pei et al. (2008) concluded that these bridges were adequate in terms of shear capacity according to the AASHTO and the ACI codes. The reported results for the I-244 Bridge girder is shown in Figure 22 (Pei et al., 2008). It should be recalled that the 'Short FRP' in the figure is the one failed in flexure.

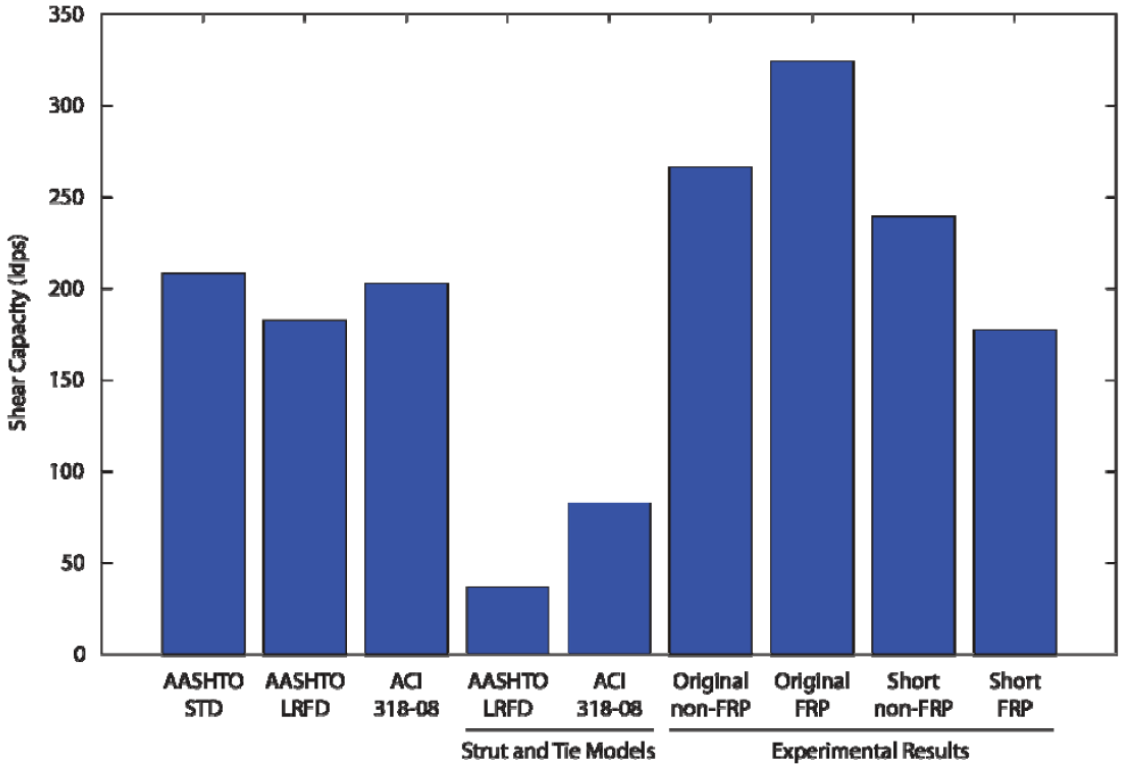

Figure 22 Results from Pei et al. (2008)

3.4. Osborn et al. (2012)

In this research, seven salvaged prestressed concrete bridge girders, AASHTO Type II, were tested for their flexural cracking and ultimate shear strengths. This bridge was built in 1968. The goal was to estimate the residual prestressing force in the tendon and the residual shear strength. The residual prestressing force was estimated from the flexural cracking tests. The shear tests were performed on each end, similar to the tests performed in this current research, with *a/d* equals to 1.5. According to this study, the AASHTO provisions underestimate the prestress losses and the shear strength. The calculated effective prestressing force using the AASHTO method was found to be 10% higher than the experimentally measured one. The predicted shear strength to the tested shear strength ratio for the girders ranged from 39% to 51% when the simplified AASHTO method was used. This method is similar to the V_{ci}-V_{cw} provided in the ACI code. In addition, the ratio ranged from 28% to 38% when the MCFT was used. The STM was much more accurate with ratio ranging from 85% to 98%. This suggests that the sectional methods for shear strength prediction is very conservative for deep beams. The reason for this was explained in subsection 2.2.3. Furthermore, finite element analyses captured the ultimate shear capacity with a difference of no more than 5%. Finally, a parametric study showed that the concrete compressive strength had a greater influence on the shear strength than the web-reinforcement spacing (Osborn et al., 2012).

3.5. El-Sayed (2014)

This research studied the effect of the corrosion on the residual shear strength of reinforced concrete deep beams. STM accounting for corrosion damage was used to predict the shear strength and then compared against experimental results. The author deemed accounting for corrosion damage by estimating the sectional losses of stirrups is impractical for evaluating in-service structures. Thus, the corrosion damage was incorporated differently in two ways. First, the effective compressive strength of struts and nodes were modified based on the widths of the superficial corrosion-induced cracks.

Second, the effective width of the member was reduced assuming the concrete cover is ineffective.

The effective compressive strength of struts was modified by accounting for the corrosion crack width in the strut and node efficiency factors, β_s and β_s, respectively. This was accomplished by using the equation developed by Coronelli and Gambarova (2004).

For struts
$$\beta_{s-corr} = \frac{1.17}{1 + K\frac{\varepsilon_1}{\varepsilon_{co}}} \leq 0.75 \tag{48}$$

For nodes
$$\beta_{n-corr} = \frac{1.17}{1 + K\frac{\varepsilon_1}{\varepsilon_{co}}} \leq k_1$$

$$\varepsilon_1 = \frac{n_{bars} w_{cr}}{b}$$

where

K	*Bar diameter and roughness coefficient (1 for medium diameter ribbed bars)*
k_1	*Node type factor (1, 0.8, and 0.6 for CCC, CCT, and CTT node, respectively)*
ε_{co}	*Concrete compressive strain at peak stress (can be taken as 0.002 for most cases)*
n_{bars}	*Number of bars in the compression zone*
b	*Beam width (undamaged width)*
w_{cr}	*Corrosion crack width*

The effective width of the member was modified in light of the work done by Higgins et al. (2003). Conservatively, the width was taken as the core width neglecting the concrete cover completely. This plays a role when calculating the strength of struts and nodes using Eq.(43) and Eq.(45).

The proposed modifications were validated using experimental data available in the literature (Suffern et al., 2010). Data included six uncorroded and nine corroded beams. The predicted strength was calculated using STM with the proposed modifications applied on the corroded beams. Comparison is given in Table 2. The author points out that the level of conservatism for both corroded and uncorroded beams is approximately consistent, thus, the proposed method is reasonable.

Table 2 Comparison between experimental results by Suffern et al. (2010) against proposed STM by El-Sayed (2014)

Beam		Concrete strength (MPa)	Corrosion crack width (mm)	Experimental shear strength $V_{u,\ exp}$, (kN)	Predicted shear strength $V_{u,\ pred}$, (kN)	$V_{u,\ exp} / V_{u,\ pred}$
Uncorroded beams	0-1.0-UR	35.7	--	401	284	1.41
	0-1.0-R	41.3	--	473	392	1.21
	0-1.5-UR	41.3	--	352	255	1.38
	0-1.5-R	41.3	--	396	318	1.24
	0-2-UR	41.3	--	150	221	0.68
	0-2.0-R	41.3	--	337	276	1.22
					Mean	**1.19**
					Standard deviation	**0.27**
					Coefficient of variation (%)	**22**
Corroded beams	L-1.0-R	45.4	0.30	356	284	1.25
	M-1.0-R	40.5	0.50	221	246	0.90
	H-1.0-R	43	0.90	283	224	1.26
	L-1.5-R	45.4	0.30	308	233	1.32
	M-1.5-R	40.5	0.30	307	220	1.39
	H-1.5-R	43	1.00	201	180	1.12
	L-2.0-R	45.4	0.30	273	209	1.31
	M-2.0-R	40.5	0.35	330	192	1.72
	H-2.0-R	43	0.6	282	183	1.54
					Mean	**1.31**
					Standard deviation	**0.23**
					Coefficient of variation (%)	**18**

3.6. Shield et al. (2018)

This research was done in the University of Minnesota, funded by the MnDOT, to assess the effectiveness of a shear strength repair technique applied on 45-type PC girders in 2013. The bridge was constructed in the 1970's and runs over the Nine-Mile Creek in Minnesota. Girders were repaired by providing additional reinforcement encased in shotcrete as shown in Figure 23. This was applied over 4 ft length of the girders near the ends. Four girders were cut into smaller lengths and brought to the lab during the demolition process in 2017. Each girder underwent one shear test by applying a single

point load until it failed. The *a/d* was greater than 2.5. Two girder ends were repaired and had significant corrosion damage, while other two ends were undamaged and unrepaired. Both repaired and unrepaired ends had the same material properties and prestressing level.

Figure 23 Rehabilitation technique used in Shield et al. (2018) (Shield et al., 2018)

Shield et al. (2018) concluded that this repairing technique was able to return the damaged ends to no less than 1% of their undamaged shear strengths. The tested strengths exceeded the predicted strengths in all cases. When measured material properties were used, the ratio of the tested strength to the predicted strengths ranged from 1.13 to 1.18. This indicates that the design-based equations for calculating shear strength is conservative. The level of conservatism is their study was much lower than the one by Osborn et al. (2012). This might be attributed to the higher *a/*d ratio used in this research. Similar to Osborn et al. (2012), the concrete compressive strength was a main factor that affected the shear strength.

It should be mentioned, however, that the damaged ends were in much more severe conditions than the ones used in this research. In addition, significant section loss was present near the ends with exposed and deteriorated shear reinforcement before repairing.

3.7. Naito et al. (2011)

This study was performed on seven corroded segments of adjacent box girders to estimate their flexural strength based on visual inspection. These girders were taken from three bridges in Pennsylvania and had been in service for more than 50 years. According to Naito et al. (2011), longitudinal cracks were found to identify the corrosion in strands better than half-cell potential and chloride level methods alone. Probabilistic-based study and quantification of corrosion in strands adjacent to longitudinal cracks were performed to provide a nondestructive method for estimating the residual flexural strength of corroded girders based on superficial deterioration.

The investigation included inspecting all types of deterioration such as spalling, delamination, longitudinal cracks and exposed strands, half-cell potential and material tests were performed. In addition, strands were exposed and each level of corrosion in strands was given an index based on the sectional loss as illustrated in Figure 24.

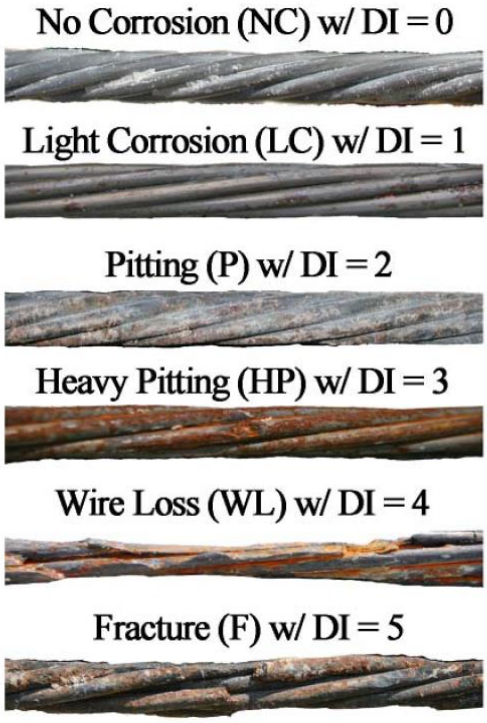

Figure 24 Strand damage condition (Naito et al., 2011)

Probabilistic-based study revealed that that the corrosion level of strands along the girder is correlated with the location of longitudinal cracks. Based on this

probabilistic study combined with the observed reduction in the tensile strength of corroded wires (Figure 24), Naito et al. (2011) proposed recommendations for estimating the residual flexural strength reproduced here in Table 3.

Table 3 Damage estimation of strands to calculate flexural strengths of corroded adjacent box beams (Naito et al., 2011)

Percent of original cross-sectional area of strands accounted for strength calculation	Which strand?
0%	• All exposed strands
75%	• Strands (in all layers) in line with a longitudinal crack • Exterior strands adjacent to a longitudinal crack located no more than 3 in. from the crack
95%	• All other strands in a longitudinally cracked beam

It is important to mention that Naito et al. suggested that all damages within an inspection window length of two development lengths are assumed to be present at the same section under consideration simultaneously. The inspection window is centered at the section under consideration. Additionally, delaminated concrete should be removed if exists. More detailed recommendations are given in Naito et al. (2010). It can be noticed that the reduction in the prestressing strand area will also affect other geometric quantities such as the center of gravity of the tendon and the prestressing force eccentricity.

Flexural strengths from these recommendations were compared against flexural strengths calculated based on the investigated condition of strands and the PennDOT guidelines. Naito et al. recommendations were able to give closer results to the forensic investigation of strands condition with some level of conservatism but less than that of the PennDOT.

3.8. Pape and Melchers (2012)

This research is similar to the work done by Alfailakawi et al. (2020). Three full-scale post-tensioned concrete girders were tested to failure in the lab. These I-shape girders were retrieved from a 45-year-old bridge named Sorell Causeway Bridge, in Australia. The bridge experienced considerable deterioration as it was exposed to aggressive environment. Tested girders were selected to have light, medium, and heavy level of corrosion damage. The cross-sectional area losses of the tendons at the failure locations due to corrosion were estimated after destructive investigation to be 0%, 57%, and 64%, respectively. Some of these losses had an external visual evidence, such as rust, cracks, while others did not have any visual evidence of damage at all. The goal of this study was to investigate the effect of the corrosion damage on the failure mode and residual strength.

Girders were tested in four-point loading conditions. All failed by progressive rupture of the wires. This type of failure is also experienced in one of the girders currently researched in this thesis. Test results showed that the light, medium, and heavy corrosion-damaged girders failed at loads that were 89%, 61%, and 45% of their corresponding undamaged-condition design capacities. This study showed that the amount of remaining cross-sectional area of the tendon correlates with the residual strength achieved in the test and the deformability developed. However, the strength correlation did not directly apply for the girder with light level of corrosion, because it did not show any loss in the cross-sectional area of the tendon at the failure location while only 89% of the design capacity was achieved. Some reasons were suggested for this girder without absolute certainty. In addition, the study showed that girders failed progressively by wires rupturing one after another. This phenomenon has been seen for deteriorated girders because corroded wires lose their ductility (Cairns et al., 2005). This was evident in the tests as the light-corroded girder failed in a very ductile manner compared to the more corroded ones.

3.9. Alfailakawi et al. (2020)

This study was performed at Virginia Tech on three corroded adjacent box girders and three corroded AASHTO Type II girders from the Aden and the Lesner bridges, respectively. Information about these girders is provided in Section 1.4. This study aimed to estimate the residual flexural strength of the girders based on visual inspection. Before testing, a detailed damage map for each girder was prepared to assess its in-situ condition. In addition, non-destructive measurements were performed, including half-cell potential and resistivity. After testing, concrete powder was collected from different locations for chloride concentration tests, strand samples were retrieved for tension tests, and concrete cores were extracted for concrete compressive strength tests. Each girder was tested under four-point loading condition using an 8-ft long spreader beam. The residual flexural strength was estimated for each girder using the strain compatibility and the AASHTO LRFD approaches. For the box beams, the estimated damage in the strands was accounted for by following the recommendations provided by Naito et al. (2011). These recommendations were found to give conservative estimate of the flexural strength, except for one box beam which contained trapped water inside the beam. For the I-beams, modifications to the Naito's recommendations were proposed resulting in closer, less conservative, estimates of flexural strength to the tested strengths. These modifications are summarized in Table 4.

Table 4 Damage estimation of strands to calculate flexural strengths of corroded I-beams (Alfailakawi et al., 2020)

Percent of original cross-sectional area of strands accounted for strength calculation	Which strand?
0%	• Cut or heavily corroded exposed strands in a spalled area
10%	• All strands in a patched area
20%	• Moderately corroded exposed strands in a spalled area
60%	• Strands in line of a longitudinal crack
80%	• Strands adjacent to a longitudinal crack • All strands in a delaminated area
100%	• Other strands

CHAPTER – 4 EXPERIMENTAL PROGRAM

This chapter goes through the experimental investigation methodology used in this research. It discusses the specimen configurations, preliminary assessment of the girders, test set-up, and post-testing investigation. Implementation of each step is described in detail. In addition, instrumentation and experimental tools used in this research are also presented.

4.1. Test Specimens

In this research, an I-shape girder with a composite concrete deck from Lesner Bridge and an adjacent box beam from the Aden Road Bridge were tested in shear. Both girders were prestressed concrete. In this document, the I-shape girder is designated as Lesner, while the other girder is designated as Aden. Brief information about these girders was explained in subsection 1.4. The Lesner girder was tested first and then the box girder. These tests were conducted in the Thomas M. Murray Structures Laboratory at Virginia Tech.

4.2. Selection of girders

Girders retrieved from the Lesner and Aden Bridges had varying degrees of corrosion damage. As expected, the bay side of the girders had a higher level of corrosion damage when compared to the inland side. From visual inspection, all Aden girders were in the most severe condition. Corrosion-related damages that appeared in the selected girders for this research include longitudinal cracks, concrete section losses, concrete delamination, exposed, or even fractured, strands, and patched areas from old repairs. The research team selected one girder from the Lesner Bridge and another from the Aden Bridge. They tried to select girders that had less, or no, level of corrosion damage at one end, while the other end shows evidence of higher level of corrosion damage.

Figure 25 and Figure 26 show the two ends condition of the selected girders from the bay side. Figure 25 (a), shows the first tested end of the Lesner girder with no

evidence of any pre-existing damage. In Figure 25 (b), a longitudinal crack with concrete delamination present in the bottom flange as highlighted. This crack indicates that the outer strands in the bottom flange have some level of corrosion damage.

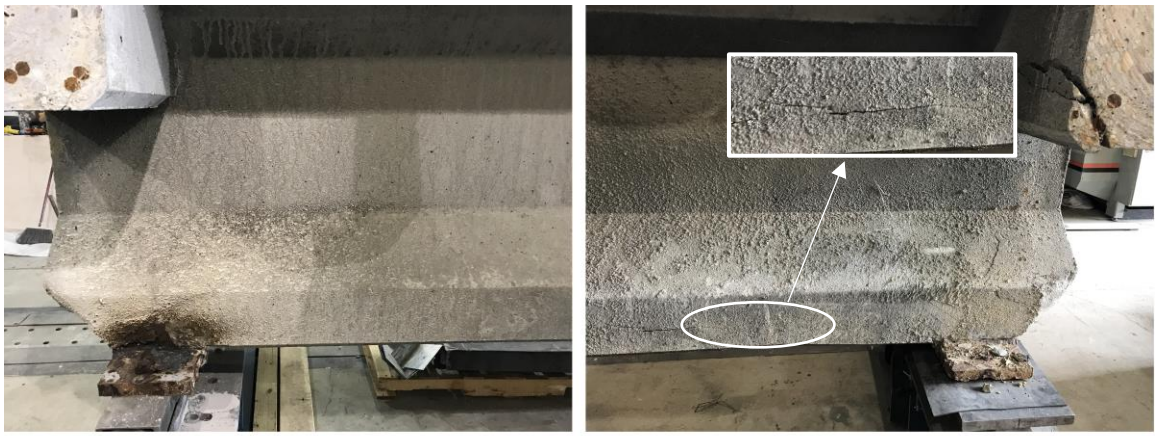

(a) (b)

Figure 25 Lesner girder end regions. (a) Undamaged end. (b) Damaged end with longitudinal crack and delamination

Obviously, the Aden girder had a heavier level of corrosion damage. Figure 26 (a) shows the first tested end of the Aden girder with less pre-existing damage manifested by a longitudinal crack as highlighted. In addition, three outer cracks were present beneath the girder at this end. Figure 26 (b), shows a significant section loss with four completely exposed strands in severe condition. In addition, an outer crack and another section loss with five exposed strands were present beneath the girder at a distance of 73 in. from the more damaged end.

(a) (b)

Figure 26 Aden girder end regions. (a) Less damaged end. (b) More damaged end with section loss and exposed strands

4.3. Estimation of Prestress Losses

The effective prestress was calculated for the girders using provisions in the AASHTO. Prestress losses after the jacking operation are elastic shortening, creep and shrinkage of the concrete, and relaxation of the strands. In Lesner girder, losses were calculated from the release stage to the deck placement, and from the deck placement to the end of service life. The total prestressing force is provided in the plans for Lesner and Aden bridges as 477.4 kip and 716.1 kip, respectively. After estimating the prestress losses, the effective prestresses for the girders are calculated and provided in Table 5.

Table 5 Losses and effective prestress for girders

	Initial Prestress (ksi)	Effective Prestress (ksi)
Lesner	185	149.7
Aden	189	156.7

Because Lesner and Aden were constructed in the 1960's and 1970's, respectively, some information regarding losses was guessed. Specifically, humidity,

time from jacking to release, and time from release to deck placement. Thus, an experimental effective prestress was back calculated during each test using the load at which the first flexural crack was observed. This procedure is outlined in subsection 5.3.

Values for the effective prestress, f_{se}, from Table 5 were used for predicting the cracking and ultimate strengths. In addition, calculations were also done using the experimental effective prestress, $f_{seEx.}$ A comparison between the two approaches is presented in Table 13.

4.4. Non-Destructive Tests

This subsection presents the methodology used to assess the in-situ condition for the selected girders. This includes visual inspection and the half-cell potential test. A detailed damage map for each girder is provided with a cross-sectional configuration following the recommendations by Naito et al. (2011) and Alfailakawi et al. (2020).

4.4.1. Visual Inspection

The selected Lesner and Aden girders were visually inspected for the corrosion-related types of damage mentioned earlier in Subsection 4.2. Before inspecting each girder, unsound concrete was chipped off using a hammer. Locations and geometries of these damages were measured from the bottom and the sides using a tape measure. In addition, a photogrammetry method was used for establishing the current condition of the girders and a 3D model was created for each girder. This work is explained in detail in research done by Neeli (2020). Figure 27 and Figure 28 present sketches of the three sides of each girder. The top sketch shows the damage on one side of the girder in its right position. The middle sketch shows the bottom of the girder. The bottom sketch shows the damage on the other side of the girder flipped up-side-down. The bottom sketch was drawn this way to allow relating the damage on that side to the damage in the bottom of the girder as some defects extend from the soffit of the girder to the sides.

In the Lesner girder, the inland side had only a minor section loss, while the bay side contained four section losses, one delamination, and four longitudinal cracks along its length. Crack lengths varied from 13 in. to 23 in. Among delamination and section

losses, one major section loss is present near the middle of the girder. All these defects were formed in the bottom flange of the girder. The bottom of the girder contained three outer section losses that were extensions from the bay side section losses, and ten longitudinal cracks with lengths varying from 10 in. to 41 in. Figure 27 shows a detailed damage map of the Lesner girder from the bottom and both sides.

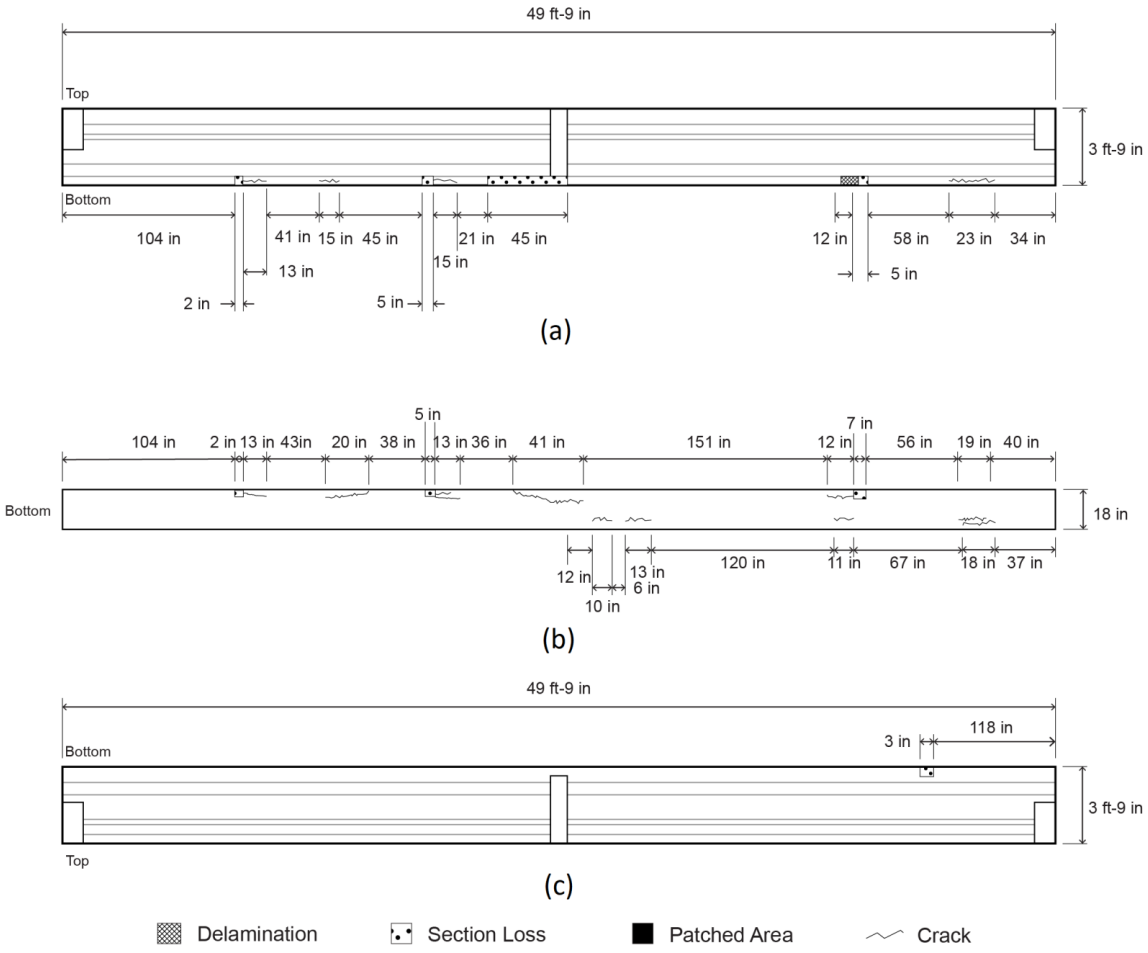

Figure 27 Damage map for Lesner girder. (a) Bay side. (b) Bottom. (c) Inland side.

In the Aden girder, the east side contained a relatively major longitudinal crack extending about 208 in. near the middle of the girder. The two ends did not have any visually detected defects except a 27-in. long crack, which was 102 in. from the second tested end. These two cracks were 3 in. from the bottom of the girder (Crack heights are not shown in the damage map for clarity). The west side of the Aden girder contained two longitudinal cracks and a significant continuous section loss. The first crack is the one that can be seen in Figure 26 (a) marked in red. The other crack is 31 in. long and

terminates as a continuous uniform section loss that runs through the rest of the length with two exposed fractured strands from the bottommost two layers. This can also be seen in Figure 26 (b). The height of this section loss is 9 in. (not shown in the damage map for clarity). The bottom of the girder contained several outer longitudinal cracks besides two major section losses with exposed strands. The first one is an outer section loss that runs through about one fifth of the girder's length with varying widths and three exposed strands. The other is at the middle of the girder's width with five exposed strands. **Figure *28*** shows a detailed damage map of the Aden girder from the bottom and both sides.

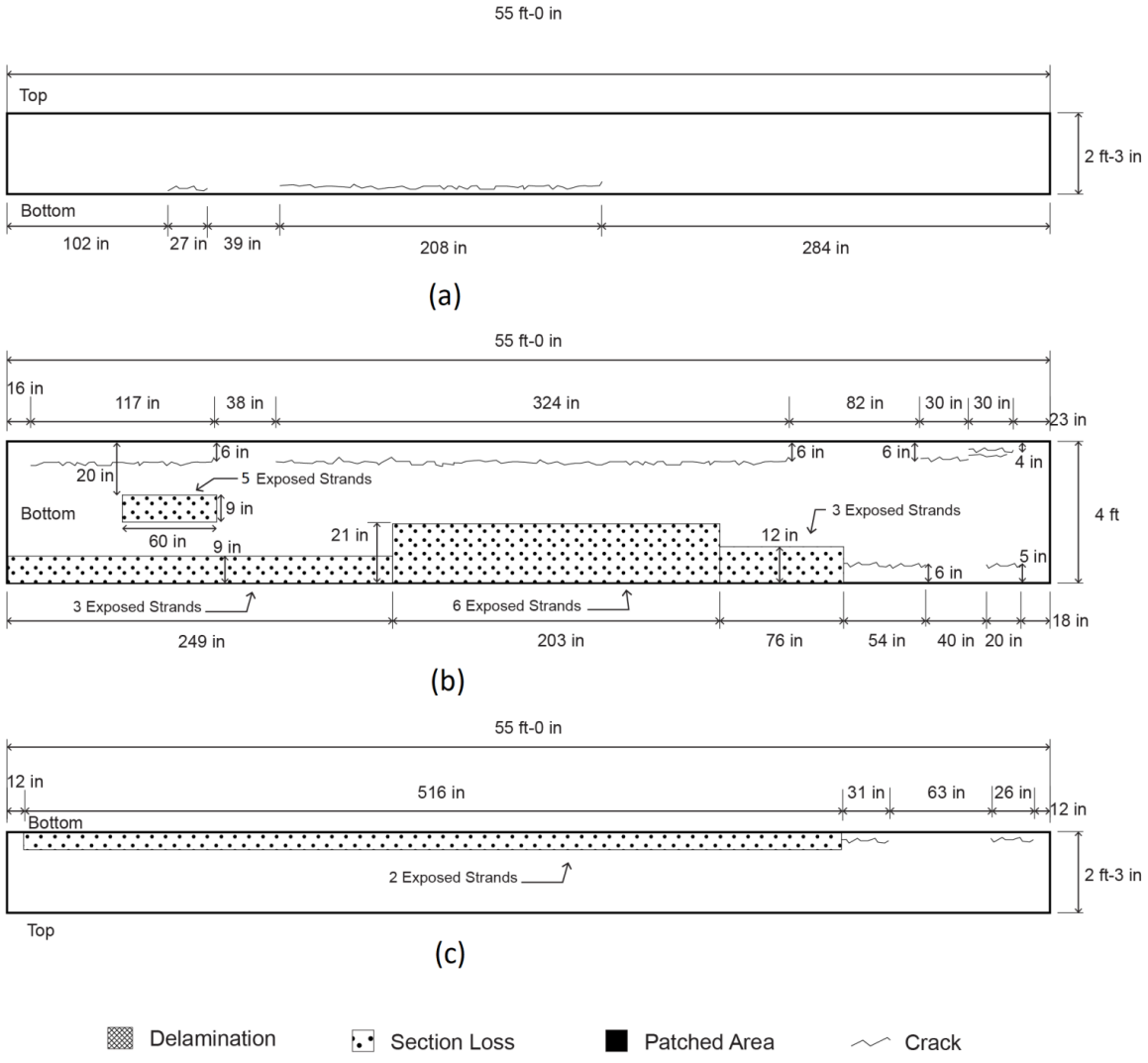

Figure 28 Damage map for Aden girder. (a) East side. (b) Bottom. (c) West side.

To perform shear and flexural analyses, a procedure proposed by Naito et al. (2011) is followed. Any damage within a window of two development lengths centered at the section to be analyzed is included. The development length for a bonded seven-wire strand is given in the AASHTO LRFD [5.9.4.3.2]. For the Lesner girder, the amount of the strands' area reduction follows the recommendations proposed by Alfailakawi (2020). For the Aden girder, the amount of the strands' area reduction follows the recommendations proposed by Naito et al. (2011). This is due to the fact that the Naito proposal was developed for box beams only and confirmed to be accurate enough (Alfailakawi, 2020). For I-beams, slight modifications to the original recommendations were made by Alfailakawi (2020). Figure 29 and Figure 30 show the damaged cross sections for the first and the second tested ends of each girder. It should be noted that *'Modified'* in the legends indicates the recommendations proposed by Alfailakawi (2020).

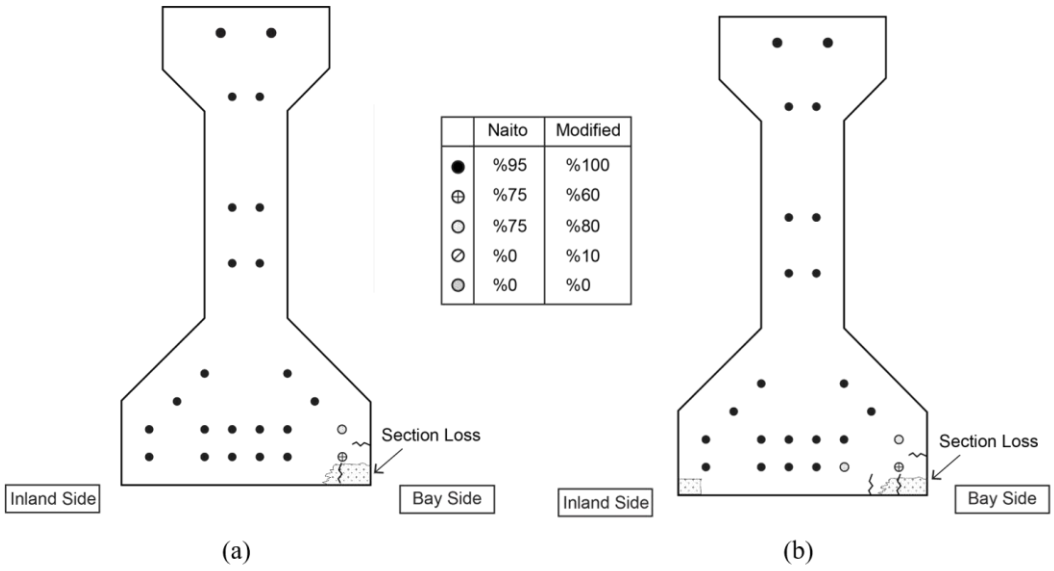

Figure 29 Damaged cross section for the Lesner girder. (a) First end (less damaged). (b) Second end (more damaged).

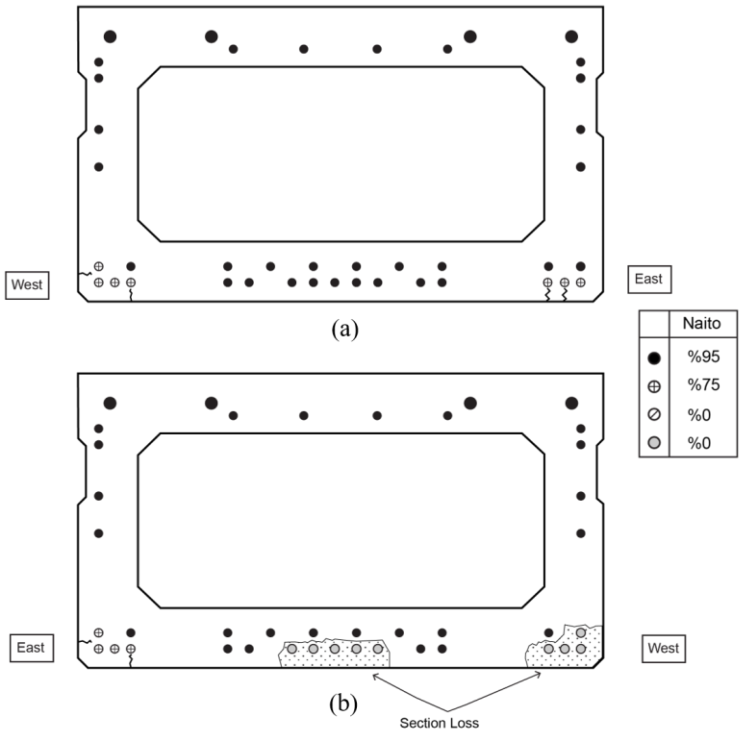

Figure 30 Damaged cross section for the Aden girder. (a) First end (less damaged). (b) Second end (more damaged).

Table 6 and Table 7 show the procedure to estimate the damage in strands for the Lesner and the Aden girders, respectively.

Table 6 Damage estimation for the Lesner girder per Alfailakawi et al. (2020)

	Layer	Distance from bottom (in.)	Original No. of strands	Reduced No. of strands	Total original area of strands	Total reduced area of strands
First End (less damaged)	1	2	6	5.6	2.574	2.504
	2	4	6	5.8		
	3	6	2	2		
	4	8	2	2		
	5	16	2	2		
	6	20	2	2		
	7	28	2	2		
Second End (more damaged)	1	2	6	5.4	2.574	2.480
	2	4	6	5.8		
	3	6	2	2		
	4	8	2	2		
	5	16	2	2		
	6	20	2	2		
	7	28	2	2		
Area of each is 0.117 in.^{2} from plans						

Table 7 Damage estimation for the Aden girder per Naito et al. (2011)

	Layer	Distance from bottom (in.)	Original No. of strands	Reduced No. of strands	Total original area of strands	Total reduced area of strands
First End (less damaged)	1	2	15	13.05	3.795	3.444
	2	4	10	9.30		
	3	12	2	1.90		
	4	16	2	1.90		
	5	20	2	1.90		
	6	22	2	1.90		
Second End (more damaged)	1	2	15	6.05	3.795	2.530
	2	4	10	8.35		
	3	12	2	1.90		
	4	16	2	1.90		
	5	20	2	1.90		
	6	22	2	1.90		
Area of each is 0.115 in.^{2} from plans						

4.4.2. Half-Cell Potential

The half-cell potential test is a non-destructive testing method standardized in ASTM C876 to identify the likelihood of corrosion in embedded steel bars, or strands, in concrete. It is performed by measuring the potential difference between a reference electrode, copper sulfate, and steel along the length of a concrete member. The more negative the value, the more likely that corrosion presents in the steel near that location. The probability of corrosion in reinforcing steel per the ASTM C876 is 90% if the potential difference is less than -0.35V. The probability that there is no corrosion in reinforcing steel is 90% if the potential difference is greater than -0.20V. The corrosion in reinforcing steel is uncertain if the potential difference between these two limits.

Although this range was developed for mild reinforcing steel, the numerical values of the potential difference can be used qualitatively for prestressing strands to gain insight into the relative probability of corrosion in some areas in the girder over others.

In the Lesner girder, at every 2 ft along the length of the girder, six measurements were taken over the depth from both sides while three measurements were taken from the bottom. In the Aden girder, three and five measurements were taken from the sides and the bottom, respectively, due its shallower depth and larger width. The data was then collected to produce contour maps shown in Figure 31 and Figure 32. The procedure followed was similar to that by Alfailkawi et al. (2020). In these figures, red areas indicate higher probability of corrosion compared to the blue areas.

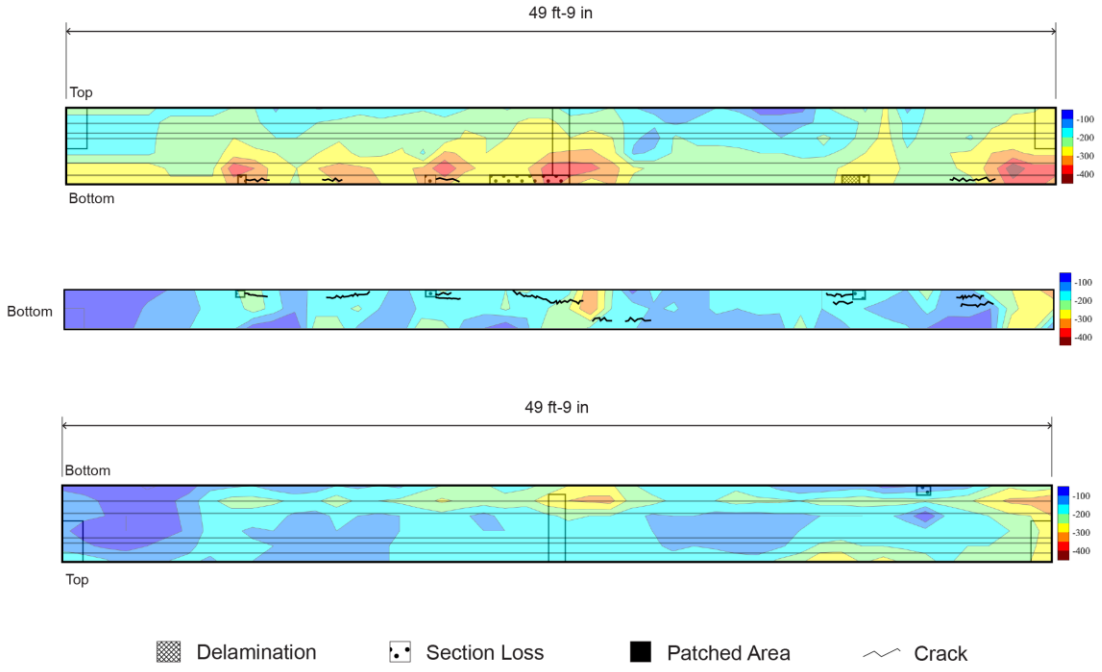

Figure 31 The half-cell potential map for the Lesner girder overlaid on the damage map

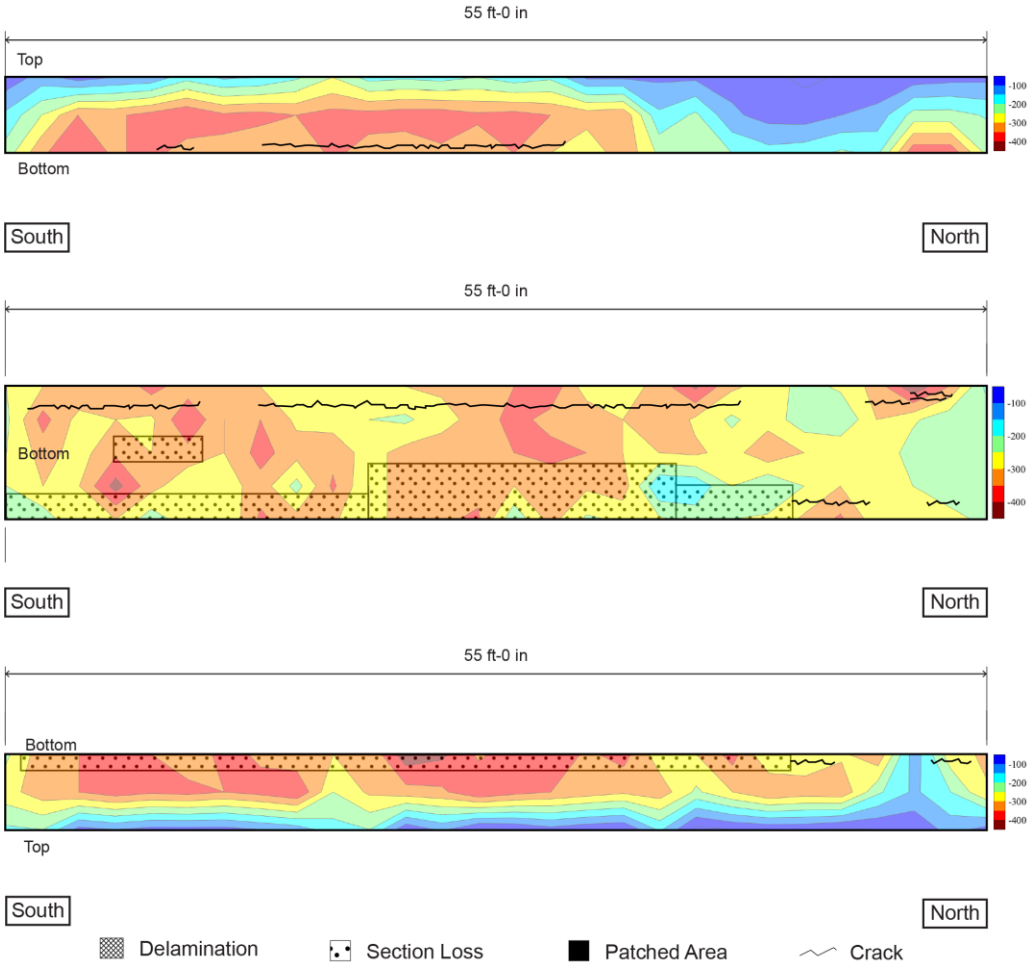

Figure 32 The half-cell potential map for the Aden girder overlaid on the damage map

Figure 31 and Figure 32 represent sketches of the two sides and the bottom of each girder and are oriented in a way similar to that described in the damage maps. The contour maps were overlaid on the damage maps so that one can correlate the visually inspected damages with the relative likelihood of corrosion indicated by the half-cell potential contour maps. It should be mentioned that the numbers provided in the contour map legend are in mV.

From the Lesner girder potential mapping (Figure 31), the bottom sketch shows that only few regions on that side have potential differences in the vicinity of -300mV indicating a lower chance that the strands in the inland side of the girder are significantly corroded. When compared to the damage map, the inland side did not have significant

deterioration. The bay side potential mapping, the top sketch, shows an increased likelihood of corrosion in several regions in the bottom flange near the longitudinal cracks. These areas have potential differences in the vicinity of -400mV and colored in red/orange. The bottom potential mapping, the middle sketch, indicates, for an unknown reason, that corrosion in most of the girder is not very likely although longitudinal cracks exist in the bottom towards the bay side of the girder. However, two spots near the right end and the middle of the girder are expected to have a higher likelihood of corrosion with a potential difference of about -300mV.

The potential mapping of the Aden girder (Figure 32) indicates that the Aden girder has significantly higher probability of corrosion than the Lesner girder. All sides of the girder seem to have a strong likelihood of corrosion everywhere where a longitudinal crack or a concrete spall exists. In addition, the mapping shows that corrosion has propagated extensively away from the expected sources of corrosion, i.e. cracks and cover losses. Only a segment of the girder between the two longitudinal cracks near the north end, the less damaged end, seems to have a lower likelihood of corrosion than the rest of the girder.

4.5. Instrumentation

Before each test, the research team installed several instruments to monitor the behavior of the specimen. Data was collected via a datalogger from BDI (Bridge Diagnostics Inc.). This instrumentation included wire potentiometers, strain transducers (strain gauges), linear variable differential transformers (LVDTs), and digital image correlation (DIC). Each wire potentiometer and LVDT was calibrated using a height gauge before use.

Wire Potentiometers

A wire potentiometer was installed beneath the girder at the loading location to monitor the displacement while testing. Load-Displacement plot gives an indication of the girder stiffness, cracking load, yielding of the reinforcement, and rupturing of reinforcement. Load-Displacement plots for the four tests are presented in section 5.1.

In the first Lesner test only, two panels of wire potentiometer rosettes were used along the shear span to measure the principle strains and the angle of inclination. A potentiometer rosette consists of two diagonal potentiometers at angles of -45 and 45, two horizontally placed potentiometers, and two vertically placed potentiometers as shown in Figure 33. However, data obtained from the potentiometer rosettes had a lot of noise and fluctuation. Therefore, the research team decided to replace it with LVDT rosettes in the next tests as will be discussed later.

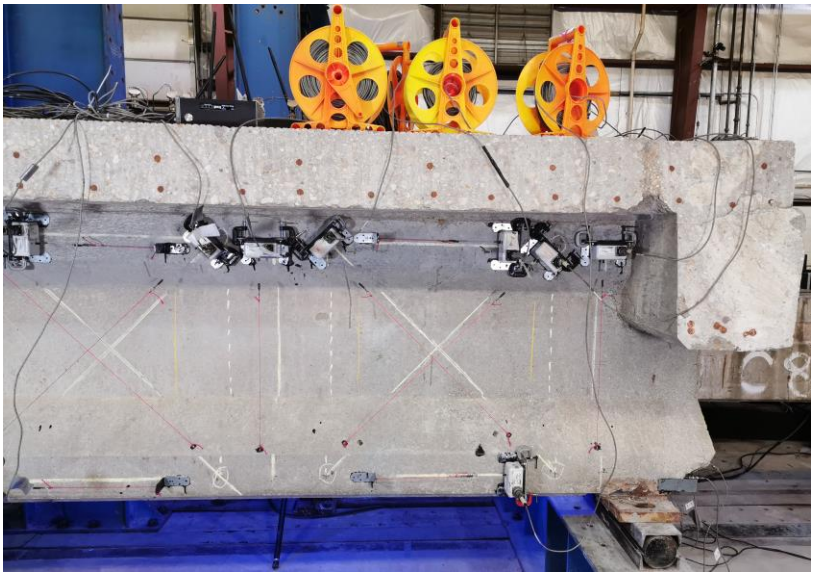

Figure 33 Wire potentiometer rosette (used for the first Lesner test only)

Strain Transducers (Strain Gauges)

All strain gauges were attached to the member surface using an instant adhesive material. They were used for three main purposes. First, a set of strain gauges were horizontally installed along the depth of the member at the loading location. These gauges are named as the horizontal strain gauges in this document. Depending on the depth and geometry of the girder, six strain gauges along the member depth were used for Lesner tests, while four gauges used for Aden tests. These gauges can be used to determine the strain profile over the member depth at each loading stage. In addition, since no elastic modulus test was conducted for the concrete, horizontal gauges were also

used to verify the elastic modulus of the concrete as will be discussed later in section 5.3. Figure 34 shows the arrangement of the horizontal gauges over the depth.

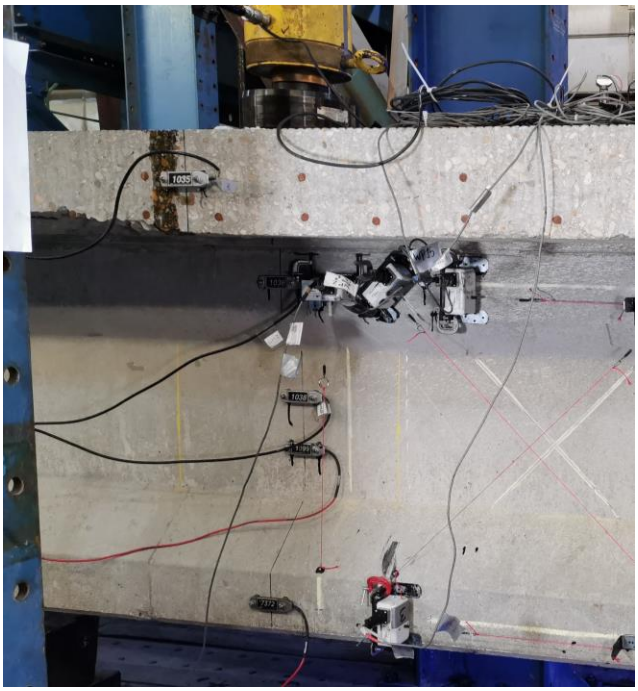

Figure 34 Horizontal strain gauges installed on the Lesner girder

Except for the first Lesner test, two strain gauge rosettes were installed 9 in. before and after the main LVDT rosette, which will be shown later. There is nothing significant about this number, 9 in., other than avoiding too much instrumentation being installed in the same area. Gauges were installed at angles of 0, 45, 90 degrees. Since strain gauges represent the state of strain over a relatively localized area, these rosettes were meant to be used only in case the main LVDT rosette malfunctioned. However, strain gauge rosettes were not of much importance as the main LVDT rosette functioned properly until removal for safety purposes.

Usually, electrical resistance strain gauges are directly attached to the stirrups before casting the concrete to investigate the stirrups' behavior. However, this luxury is unavailable for an already cast girder. Therefore, a set of strain gauges were installed vertically on the concrete surface at the stirrup locations tracing an expected cracking path. This method was also used by Osborn et al. (2012) discussed in subsection 3.4. The cracking path was based on the judgement of the research team. To locate stirrups, a ground penetration radar (GPR) was used. An implicit assumption here is that stirrup

strain is compatible with the adjacent exterior concrete. The main goal of these strain gauges is to know whether the web reinforcement has yielded when the failure occurred. In addition, the DIC was used for performing this task as well. Strain gauges and LVDT rosette are shown in Figure 35.

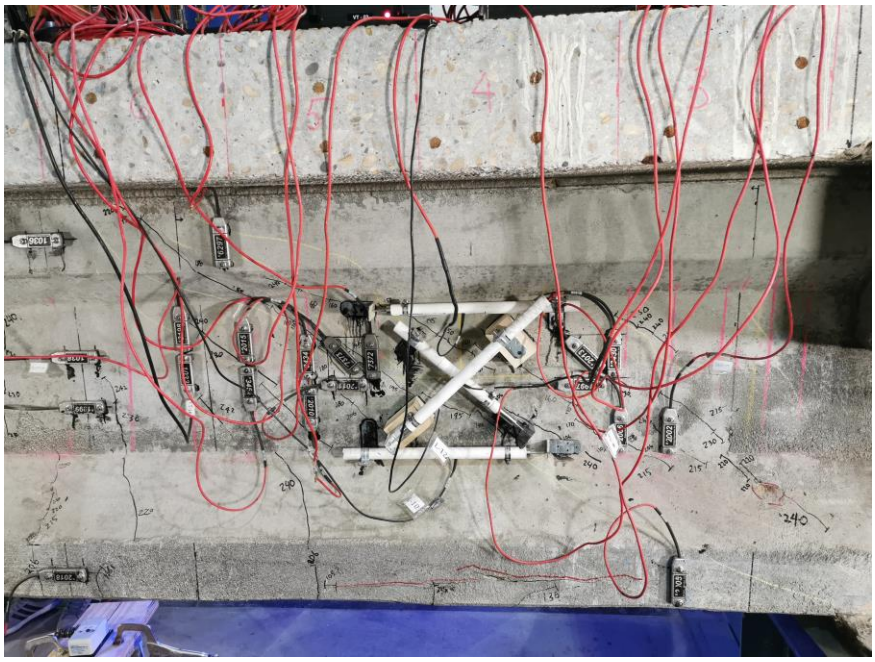

Figure 35 LVDT rosette and strain gauges installed on the Lenser girder

Linear Variable Differential Transformers (LVDTs) Rosette

Except for the first Lesner test, an LVDT rosette was used for two purposes. These LVDTs have a gauge length of 2in. approximately. To obtain average strains, displacements are to be measured over long enough distance that includes at least one crack. This is the basis for the average strains and stresses discussed in the MCFT. Thus, LVDTs' gauges' lengths were extended to 16 in. using plastic tubes as shown in Figure 36. Each tube was attached to a piece of wooden block that was installed to the girder surface using adhesive material.

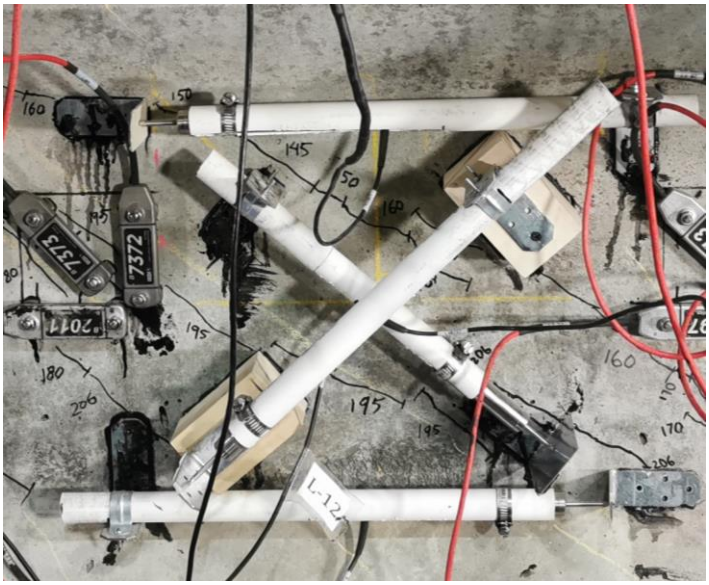

Figure 36 LVDT rosette installed on Lesner girder

An idealized LVDT rosette consists of three LVDTs oriented at angles of -45, 45, and 0 degrees. Because assembling such a rosette is impractical, two LVDTs were placed at -45 and 45 degrees, while other two were placed horizontally offset by -10 in. and 10 in. from the center of the LVDT rosette. It is assumed that the longitudinal displacement change at the center of the rosette can be obtained by averaging the readings from the two horizontally placed LVDTs. The center of the LVDT rosette was placed at the middle of the shear span longitudinally, which is approximately the critical section for shear as per AASHTO. Vertically, the rosette center was placed at the centroidal axis for Aden girders and at the middle of the web for Lesner girder due to geometry restrictions.

Strand slip LVDTs

As mentioned in subsection 2.2.2, shear increases the tensile force demand on the longitudinal reinforcement. Especially when the load is applied within the development length of the reinforcement, this can lead to a shear tension (bond) failure which can be manifested by slipping in strands. AASHTO requires checking the longitudinal reinforcement demand using equations presented in Section 2.2.2. Experimentally, strand slip was monitored using LVDTs with a stroke length of about 0.2 in. Kassner (2012) defined a strand slipping failure threshold as 0.02 in. of inward slip.

Because corrosion-damage is expected to significantly affect the outermost strands, four-short-stroke LVDTs were attached to the bottommost layer of strands. Two LVDTs were monitoring the outer strands slip, while other two were monitoring the inner strands slip. LVDTs were attached directly to the cross-sectional surface of the strands and held snug in their position using aluminum brackets glued to the concrete surface. Figure 37 shows the strands slip LVDTs.

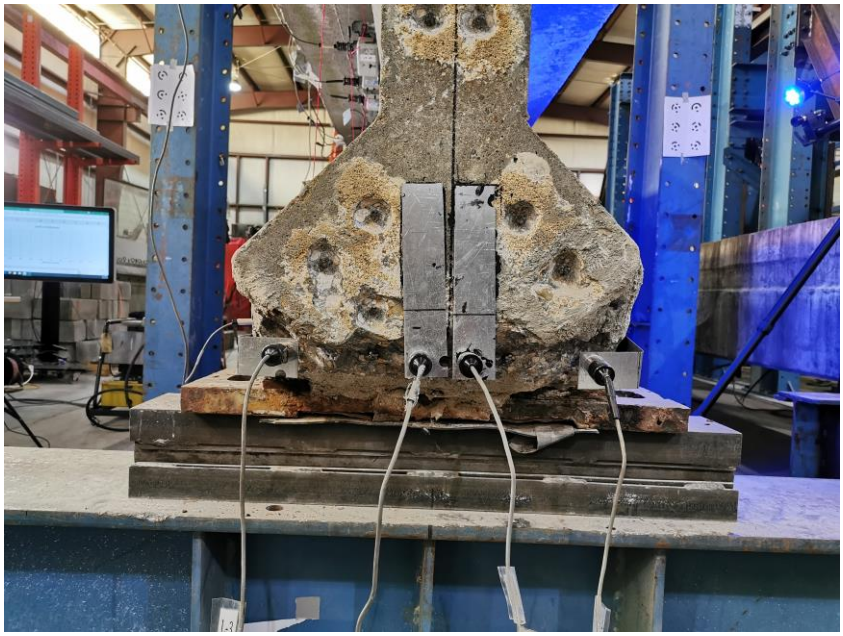

Figure 37 Strands slip LVDTs in Lesner girder.

Digital Image Correlation (DIC)

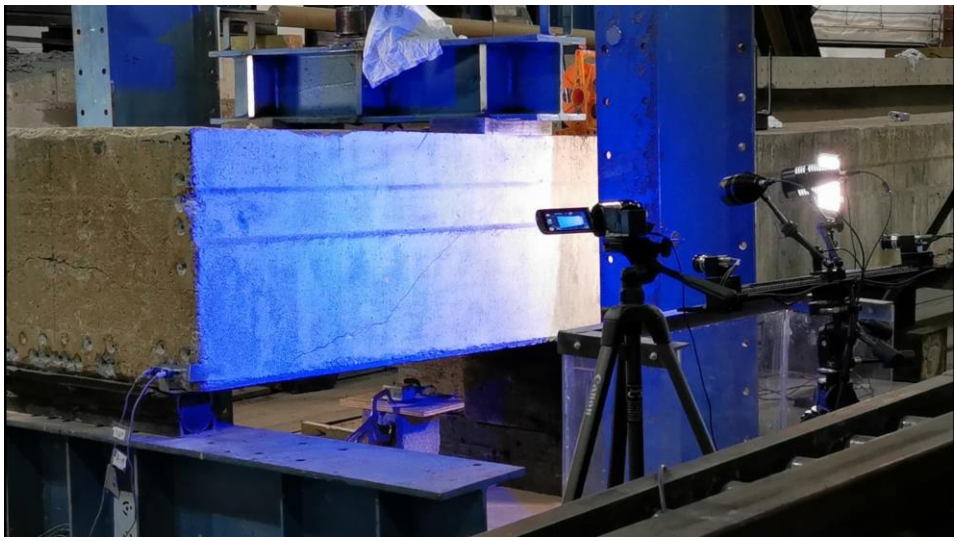

Figure 38 DIC machine monitoring the first Aden test

Digital Image correlation (DIC) is an optical technology used in this project to measure deformations with no contact to the object. The deformations are measured with respect to a reference stage, for example the unloaded stage, by taking photos of the inspected area at multiple stages of loading. Before each test, the DIC machine was calibrated using a specific calibrating panel and the surface of the girder was cleaned with a metal brush to remove any stuck debris or dust. Then, the inspected area of the girder was spray-painted in a white and black pattern as shown in Figure 38. The surface area of girders inspected using the DIC was about 30 in. by 24 in., where the longest dimension is along the girder's longitudinal axis. In this research, fields measured using the DIC are displacements and strains. Calibration, inspection, and data processing are done using GOM Correlate Software. During each loading stage, the research team took a snapshot of the girder and entered the load value to the inspecting software. A sample of the DIC results is shown in Figure 39 which shows a contour map of the tensile principle strains over the inspected web surface at a specific loading stage.

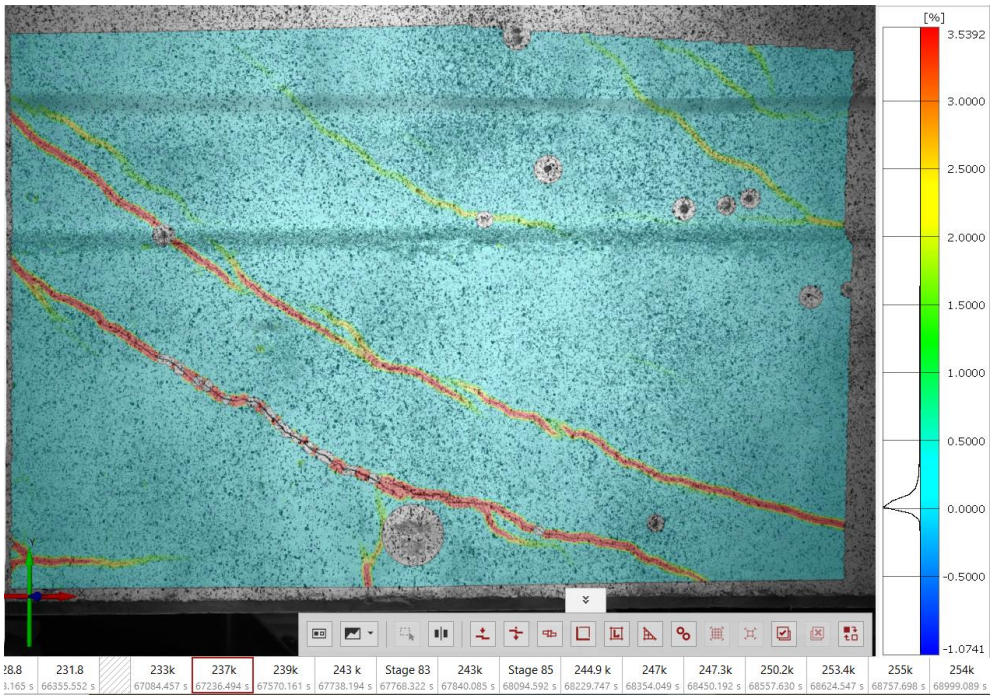

Figure 39 Maximum principle strain field in the first Aden test at an applied load of 237 kip (GOM Correlate)

4.6. Test Set-up

Upon placement of each girder in the lab, concrete surface was cleaned to facilitate identifying cracks during the test, and to enhance the adhesion of the glued instruments on the surface. Stirrups were located and marked using a metal detector device. In addition, strands were exposed at the ends to measure their slip. Several cameras were used from both sides to capture and record the behavior of the girder throughout the test. The load cell was calibrated each time using the compression test machine.

Before each test, the flexural-cracking load, web-shear cracking load, and flexural capacity, were estimated according to the ACI318-19 and the LRFD AASHTO codes. Flexural capacity was calculated using the basic beam theory where the assumption of plane sections remain plane is stipulated. In this approach, a limiting strain value, usually 0.003, is prescribed at the extreme compression fiber that causes crushing in concrete. In the literature, this approach is sometimes referred to as the *Strain Compatibility*

Approach. In addition, the shear capacity was estimated using the methods discussed in Section 2.2. All strength reduction factors, and load factors were taken as unity. In most tests, the load was applied in 10-kip increments. The loading increment was reduced to 5 kip as we approached the predicted cracking load. Then, the loading increment was returned to 10 kip. At each loading stage, the load value was entered into the GOM Correlate Software (see instrumentation subsection). In addition, the research team monitored and marked the new forming cracks and extension of the old cracks. This process ceased when getting close to the girder became a safety concern for people in the lab. Figure 40 shows the test set-up for the Lesner girder.

Figure 40 Test set-up for Lesner

In Aden tests, the load was applied on the hollow part of the girder as shown in Figure 43. Therefore, punching the top flange of the girder was a concern. The research team decided to use a steel spreader beam to distribute the actuator load evenly on the two webs directly. The spreader beam was transversely stiffened by three pairs of 1-in-thick steel plates. Stiffeners were required to avoid web local yielding of the spreader beam if the full actuator capacity was used. Figure 41 shows the steel spreader beam used in Aden tests.

Figure 41 Spreader beam used in Aden tests

Configuration and Dimensions

Each of the aforementioned girders was tested twice in the lab in a three-point loading condition. The load was applied on the specimen using a hydraulic actuator machine with a capacity of 400 kips through a 9 in. by 14 in. elastomeric neoprene pad. The long dimension of the pad was aligned with the beam axis. True pin and roller supports were used for the reactions. The load was gradually increased until the girder failed. The first test was conducted by applying the point load near the less damaged end. This can be used as a baseline for the shear strength comparison of the specific girder.

As most bridges designed to have a ductile flexural failure prior to reaching their shear strength, the researcher intended to select an appropriate shear span-to-depth ratio so that the girder failed in shear. The problem here arises from the fact that in most real-world girders, the shear capacity to demand ratio at the nominal moment is greater than 1. In other words, having a ‘too’ long shear span can lead to a flexural failure, which is something undesired for the purpose of this research. On the other hand, very short shear span will transition the behavior from a slender beam to a deep beam. In deep beams, a

major portion of the load is carried by the direct arching action. This is something, also, undesired in this project because the stirrups are not fully engaged in resisting the shear. In other words, the load is not carried in the sectional mode. However, falling in deep beam behavior in this research was inevitable.

The specimen configuration of the four tests is given in Figure 42 and Figure 43. The intended shear-span-to-depth ratios, a/d, are given in Table 8. The actual *a/d* for the tests might have slightly changed by ±3in. This is due to the fact that the loading frame is connected to the ground through 6-in.-spaced holes. However, this deviation is considered minor and the intended values for *a/d* are still used in calculations.

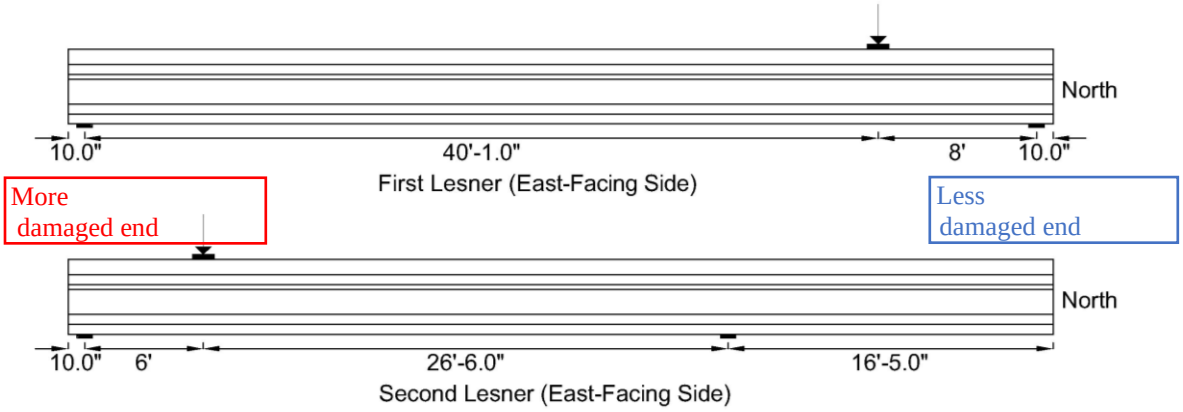

Figure 42 Lesner girder test set-up

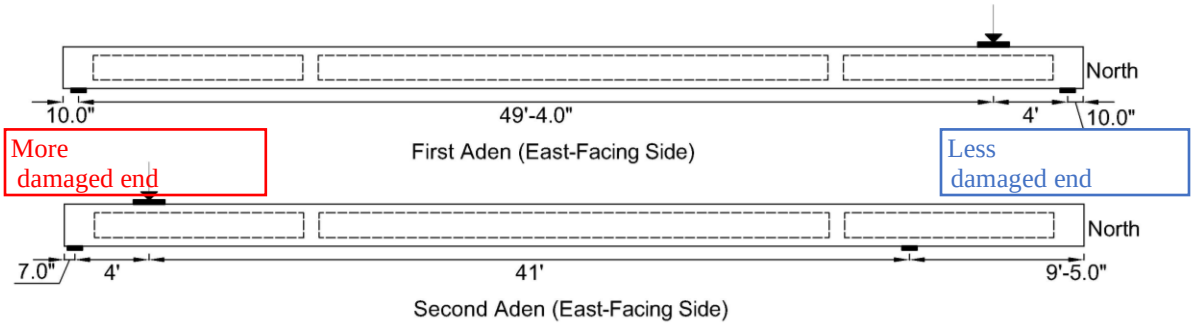

Figure 43 Aden girder test set-up

Table 8 Configuration of the tested specimens

	Overall length (ft)	Net span (ft)	Shear span (ft)	Shear-span-to-depth ratio	Critical section for shear from the end (ft)
First Lesner	49.75	48.083	8	2.629	4
Second Lesner		32.5	6	1.971	4
First Aden	55	53.333	4	2.222	2.787
Second Aden		45	4	2.222	2.537

It can be noticed from the table above that the net span in the second test for each girder is shorter than the one in the first test. This was done by moving the support near the first tested end beyond the damage occurred during the first test to avoid any potential undesired failure that may happen due to the pre-existing damage. The research team selected the location of the support for the second test by ensuring that the girder will not crack due to the self-weight moment induced by the overhang portion of the girder.

4.7. Material Tests

After each test, the research team conducted some destructive tests on the girder. These include extracting concrete cores, stirrups, and strands. In addition, concrete was chipped off near the failure location and strand condition was investigated.

Concrete cores were taken from the webs and the top flanges near the ends of the girders. In Lesner girder, the top flange core is taken from the deck. Concrete cores were tested in uniaxial compression using correction factors as per the ASTM C39, if necessary. Table 9 shows the concrete compressive strength results.

Table 9 Compressive strength of the concrete cores

	Location	L/D	Correction factor	Compressive strength (ksi)
Lesner	Deck	1.38	0.94	4.04
	Deck	2.23	1.00	3.97
	Deck	2.1	1.00	4.26
	Average			4.09
	Web	1.5	0.96	5.36
	Web	1.63	0.97	4.6
	Web	2.09	1.00	4.91
	Average			4.957
Aden	Top flange	1.596	0.97	6.62
	Top flange	1.948	1.00	5.27
	Top flange	1.952	1.00	6.35
	Average			6.08

After each test, samples of the stirrups and the strands were retrieved for tension tests. These samples were taken from relatively undamaged regions in the girders to ensure that they were not stressed over their yield stresses. The tension tests were performed using a Universal Test Machine in the Virginia Tech lab. The yield stresses and the ultimate strengths for the stirrups retrieved from the Lesner girder and the Aden girder are provided in the following tables.

Table 10 Stirrups tension test for the Lesner girder

	Length (in)	Yield Stress (ksi)	Ultimate Strength (ksi)
Sample #1	6.75	48	74.8
Sample #2	6.75	49	75.82
Average		48.5	75.31

Table 11 Stirrups tension test for the Aden girder

	Length (in)	Condition	Yield Stress (ksi)	Ultimate Strength (ksi)
Sample #1	16.25	Uncoated	60	92
Sample #2	16.5	Uncoated	62	95.5
Sample #3	16.75	Epoxy-coated	71	111
Average			64.33	99.5

In addition, samples of the prestressing strands were retrieved as well for tension tests. The strand samples were about 4-ft long and were tested using a Universal Test Machine in the Virginia Tech lab as per the ASTM A370 standards. Unlike the mild reinforcement, strands consist of smooth seven wires helically wrapped. Therefore, a premature failure might occur at the highly stressed regions near the ends if strands were gripped directly by the testing machine jaws. To avoid this undesired failure, two pieces of an aluminum pipe were cut and attached to the strand ends using an adhesive mix of aluminum oxide and epoxy. More details about the tension test of the strands can be found in research by Loflin (2008). The strain was measured initially using a 9-in. gauge length extensometer until about 1% strain at which the extensometer was removed to prevent it from the potential damage due to the specimen rupture. After the extensometer removal, the strain was taken directly from the testing machine crosshead measurements. The stress-strain curves for the tested strands are shown in Figure 44 and Figure 45.

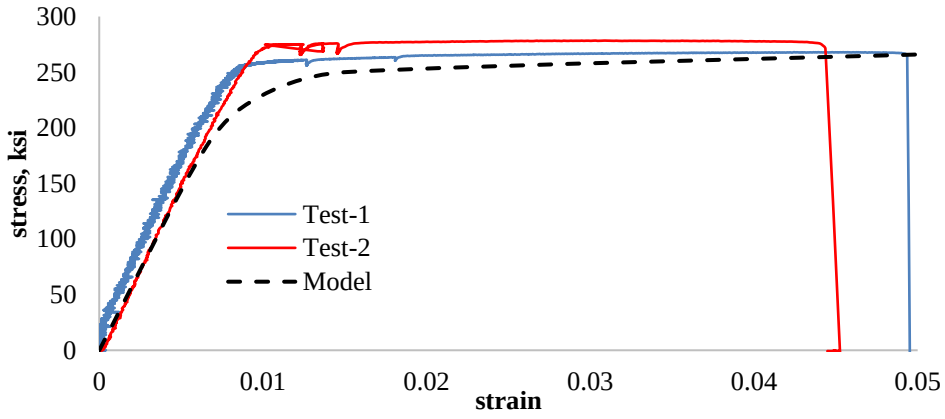

Figure 44 Stress-strain curves for the strands retrieved from the Lesner girder

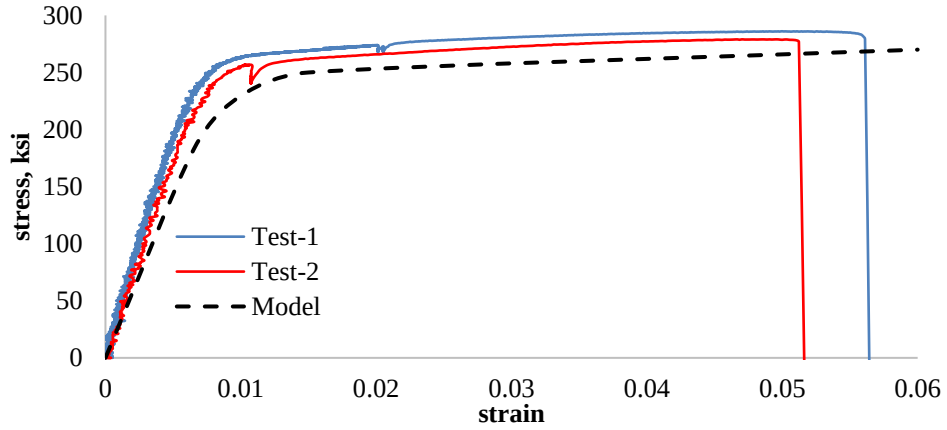

Figure 45 Stress-strain curves for the strands retrieved from the Aden girder

After retrieving strand and stirrup samples, concrete near the failure location for each test was chipped away and a close-up destructive investigation for the corrosion level in strands and stirrups was performed. This type of investigation is not applicable for rating in-service bridges. However, it is meant here to provide information about the girders at hand and to assess the recommendations based on visual inspection proposed by Naito et al. (2011) and Alfailakawi (2020). Results from post-testing investigation is discussed in subsection 5.2.

CHAPTER – 5 RESULTS AND ANALYSIS

5.1. Results from the Destructive Shear Tests

First Lesner Test

The shear span for this test was 8 ft with a shear-span-to-depth ratio of 2.629. Other information is given in Table 8. In this test, the load was applied in 5-kip increments throughout the entire test. The first shear crack was initiated at the middle of the girder's web at a load of 120 kip, and located 46.5 in from the closer end, which was very close to the critical section for shear, 48 in., as per the AASHTO LRFD. The corresponding total shear at this location was 115 kip when the crack initiated. This crack formed from both sides of the girder simultaneously. The corresponding deflection at the loading location was 0.31 in

The first flexural crack was observed in the bay side at a load of 141 kip. The corresponding total moment at this location 1047 kip-ft, while the deflection was 0.40 in. This instance is indicated by a bend in the Load-Displacement plot shown in Figure 46. This crack emerged as an extension from a pre-existing cracks located at 106 in. from the end (See Figure 27 (a)).

After that, several web-shear cracks and flexural cracks opened in both sides. These cracks were almost parallel. Most of these cracks propagated upwards to the top flange of the girder, and some reached the bottom of the deck. Figure 47 shows the cracking pattern for this test. This excessive propagation of developed shear and flexural cracks indicated that both flexural and shear failures were impending. At a load of 258 kip, chunks of concrete located at pre-existing damage fell off and one strand ruptured in the bay side. This rupture is indicated by a small drop-off in the Load-Displacement (Figure 46). Indeed, post-testing investigation showed that one strand in the bay side had fractured (Figure 48(c)). Wide and shallow cracks formed near the location where the strand ruptured (Figure 48(b)). Not long after, the concrete deck crushed near the loading location at 264.8 kip of applied load and the test was stopped. This load corresponds to a total moment of 1882 kip-ft at the loading location, and a total shear of 235.8 kip at the

critical section for shear. The girder attained a maximum deflection of 3.22 in. when the girder failed. Figure 48 shows the failure mechanism of this girder end.

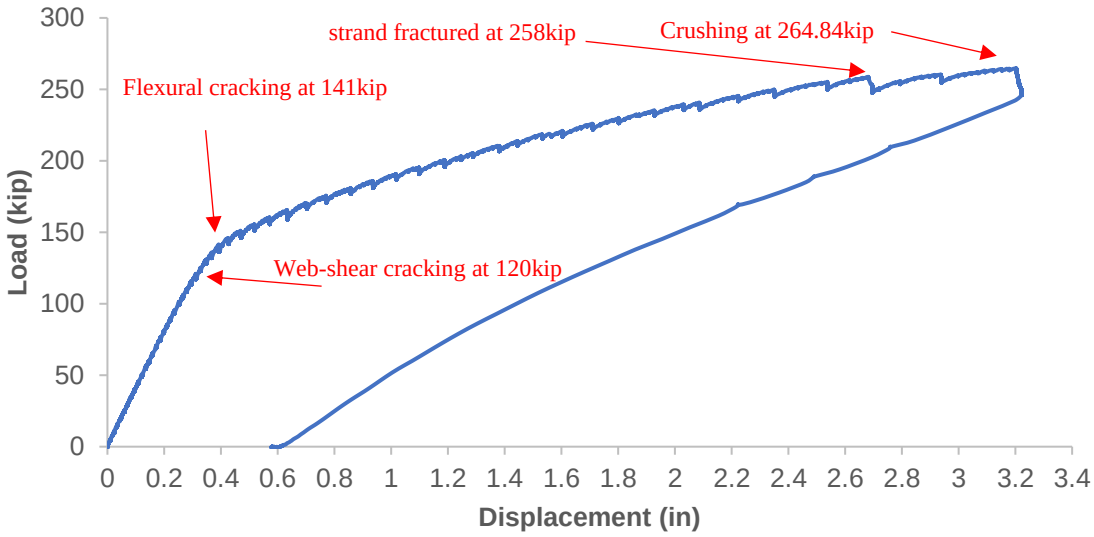

Figure 46 Load-Displacement for the first Lesner test

Figure 47 Cracking pattern for the first Lesner test (inland side)

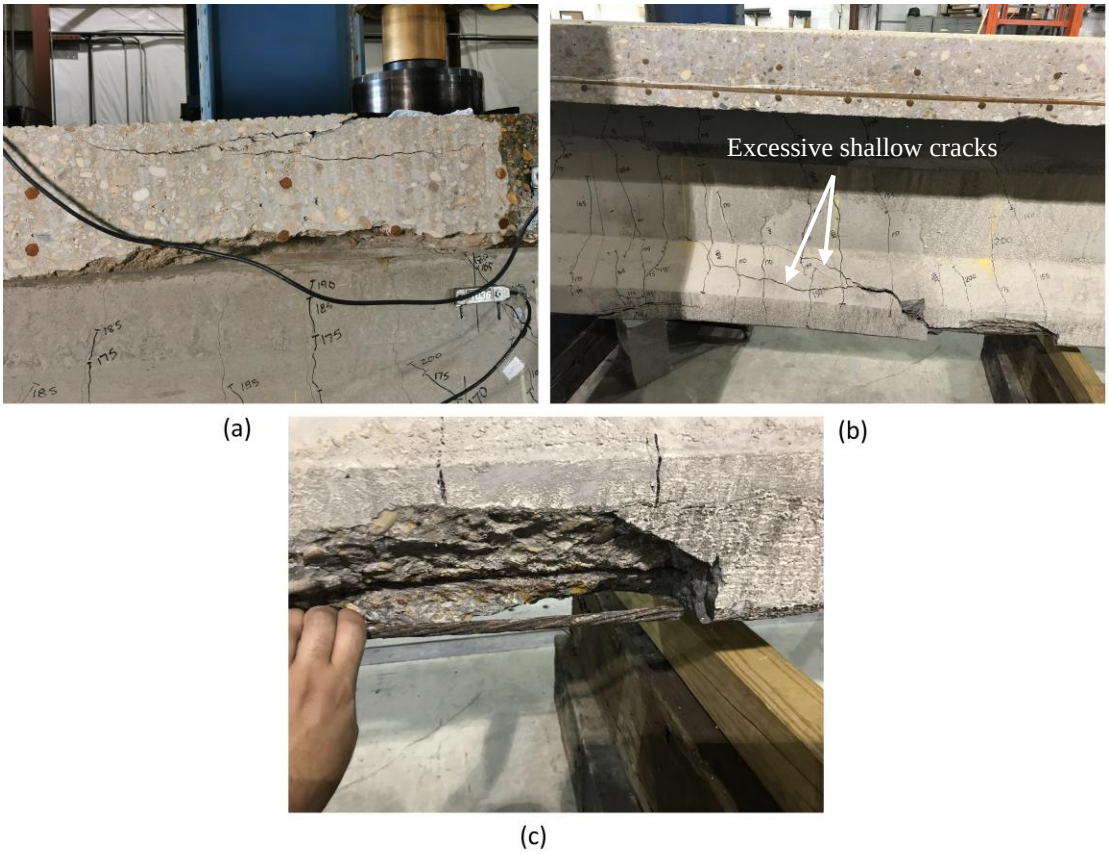

Figure 48 Failure mechanism for the first Lesner test. (a) Top crushing. (b) Excessive cracking in the bay side where the strand ruptured. (c) Strand ruptured in the bay side.

Second Lesner Test

The shear span for this test was 6 ft with a shear-span-to-depth ratio of 1.971. Other information is given in Table 8. In this test, the load was initially applied in 10-kip increments until reaching close to the expected cracking load, at which the load was applied in 5-kip increments. When an additional load caused no opening of new cracks, the loading protocol was returned back to 10-kip increments. The first web-shear crack was observed at a load of 136 kip in the inland side of the girder. This crack was located 43 in. from the closer end, which was 5-in. distant from the critical section for shear, 48 in., as per the AASHTO. The corresponding total shear at this location was 117.6 kip when the crack initiated. The corresponding deflection at the loading location was 0.22

in. The first web-shear crack on the bay side of the girder formed at an applied load of 145 kip at almost the same location as the inland-side shear crack.

The first flexural crack was observed on the bay side of the girder at a load of 206 kip and located approximately at the maximum moment location along the length of the girder. The corresponding total moment at this location 1046.4 kip-ft, while the deflection was 0.34 in.

After that, several web-shear cracks and flexural cracks opened in both sides. These cracks were almost parallel. Some of these cracks propagated upwards reaching to the top flange of the girder. Figure 50 shows the cracking pattern for this test. The BDI instruments, except the wire potentiometer, were removed at a load of 271 kip for safety purposes. After reaching 340 kip of applied load, many "popping" sounds were heard repeatedly. Because there was no a major load drop in the Load-Displacement plot at 340kip (Figure 49), these sounds were attributed to opening of new cracks. In addition, post-testing investigation showed that no strands appeared to be fractured during the test. The load was increased consistently until 382.4 kip at which the diagonal strut crushed in a very explosive and brittle manner. The crushing occurred in the web and was located at the middle of the shear span along the length of the girder. This load corresponds to a total moment of 1910 kip-ft at the loading location, and a total shear of 318.2 kip at the critical section for shear. The girder attained a maximum deflection of 1.92 in. when it failed. Figure 51 shows the failure mode of this girder end. Before the web crushed, cracks were inclined with about 35-degree angle. However, at failure, the web crushed at a steep-angle crack which took a short path from the point load to a close concrete spall instead of extending towards the support as expected.

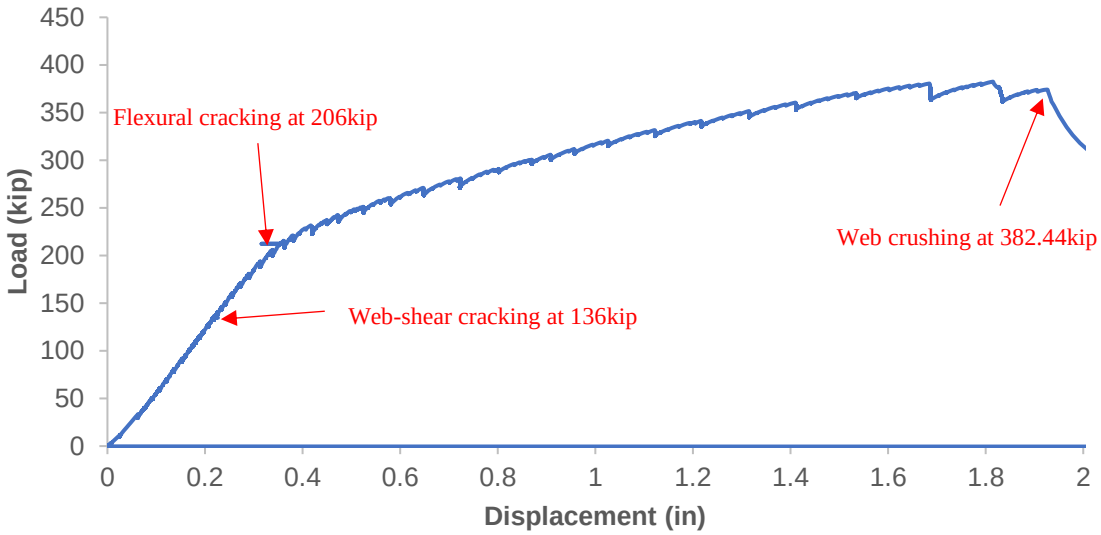

Figure 49 Load-Displacement for the second Lesner test

Figure 50 Cracking pattern for the second Lesner test

Figure 51 Failure mode for the second Lesner test (Web crushing)

First Aden Test

The shear span for this test was 4 ft with a shear-span-to-depth ratio of 2.222. Other information is given in Table 8. In this test, the load was initially applied in 10-kip increments until reaching close to the expected cracking load, at which the load was applied in 5-kip increments until failure. The Load-Displacement for this test is shown in Figure 52. The first web-shear crack was observed at a load of 150 kip in the west side of the girder. This crack was located 46 in from the closer end of the girder. The corresponding total shear at this location was 155.83 kip when the crack initiated. The corresponding deflection at the loading location was 0.26 in.

The first flexural crack was observed on the west side of the girder at a load of 205 kip and located at the maximum moment location along the length of the girder. The corresponding total moment at this location 829.5 kip-ft, while the deflection was 0.56 in. However, generally, the flexural cracks did not propagate extensively to the top of the girder and the behavior was dominated mainly by shear deformations.

Only few parallel web-shear cracks formed on either side of the girder throughout the test. This observation can be noticed in girders with relatively high shear

reinforcement spacing. Figure 53 shows the cracking pattern for this test from the west side of the girder. The BDI instruments, except the wire potentiometer, were removed at a load of 215 kip for safety purposes. After reaching 250 kip of applied load, the critical web shear crack significantly opened and the shear failure seemed imminent. The load was increased until 259.2 kip at which point the girder separated to two portions that slipped against each other due to lack of aggregate interlock and the test was stopped. The failure mechanism of this girder is shown in Figure 54. This load corresponds to a total moment of 1030 kip-ft at the loading location, and a total shear of 257.6 kip at the critical section for shear. The girder attained a maximum deflection of 1.9 in. when the girder failed.

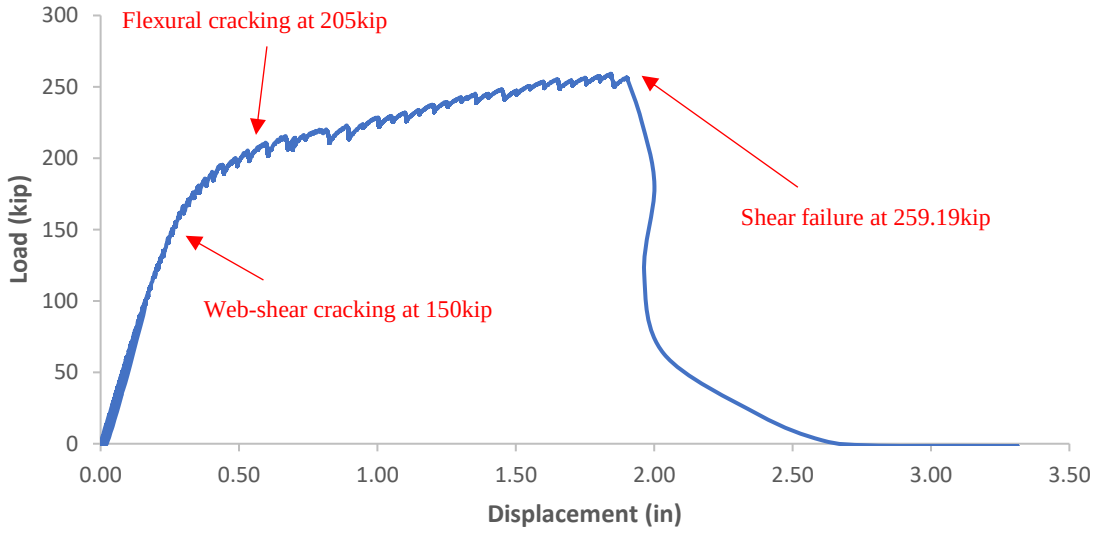

Figure 52 Load-Displacement for the first Aden test

Figure 53 Cracking pattern for the first Aden test

Figure 54 Failure mode for the first Aden test (Diagonal tension)

Second Aden Test

The shear span for this test was 4 ft with a shear-span-to-depth ratio of 2.222. Other information is given in Table 8. In this test, the load was initially applied in 10-kip increments until reaching close to the expected cracking load, at which the load was applied in 5-kip increments until the protocol was changed to deflection control. The Load-Displacement for this test is shown in Figure 55. The first web-shear crack was observed at a load of 150 kip in the east side of the girder. This crack was located near the middle of the shear span, which was close from the critical section for shear, 30.44 in., as per the AASHTO. The corresponding total shear at this location was 150.8 kip when the crack initiated. The corresponding deflection at the loading location was 0.26 in.

The first flexural crack was observed on the west side of the girder at a load of 170.7 kip and located 6in. from the maximum moment location towards the furthest end of the girder from the load. The corresponding total moment at this location 677.0 kip-ft, while the deflection was 0.31 in. This low value of flexural cracking load can be attributed to the excessive pre-existing damage near the soffit of the girder where the bottom concrete cover was completely missing as shown in Figure 56.

Similar to the first Aden test, only few parallel web-shear cracks formed on either side of the girder throughout the test. Figure 56 shows the cracking pattern for this test from the west side of the girder. At 190kip of applied load, a shear crack propagated all the way down, and up close to the loading pad. Until this moment, the behavior of the girder was similar to the first Aden girder. The BDI instruments, except the wire potentiometer, were removed at a load of 210 kip for safety purposes. When the applied load reached 225kip, “popping” sounds were heard many times during the test as the deflection was increased. At each sound, a sudden drop in the Load-Displacement was noticed as shown in Figure 55. In addition, the girder stiffness decreased in the following stages of loading and the loading protocol was changed to displacement-control. Meanwhile, severe flexural cracks propagated from a pre-existing section loss in the bottom of the girder located about 4.5ft from the point load towards the furthest end of the girder as shown in Figure 57 (a). The “popping” sounds with the corresponding drops

in the Load-Displacement were attributed to fracturing of strand wires. Ultimately, strand wires kept fracturing progressively and the behavior of the girder turned to flexural dominated as the curvature significantly increased at that location. Figure 57 (b) shows the condition of strands after the test. The maximum recorded applied load was 230.5kip and the girder could not hold any higher load since then. This load corresponds to a total moment of 896.4 kip-ft at the maximum moment location and a total shear of 224.2 kip at the critical section for shear. The test was terminated when the deflection at the point load location exceeded 3.5in.

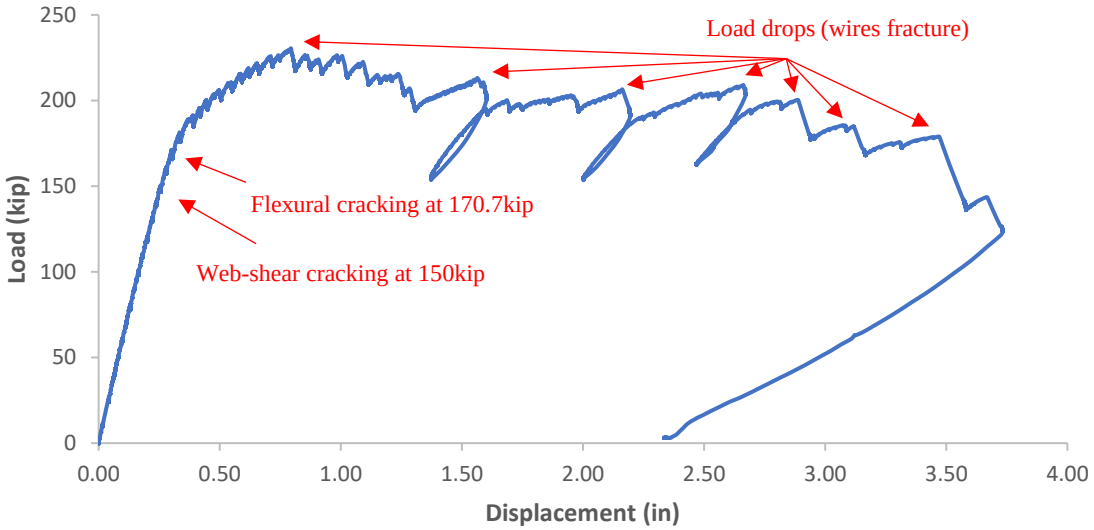

Figure 55 Load-Displacement for the second Aden test

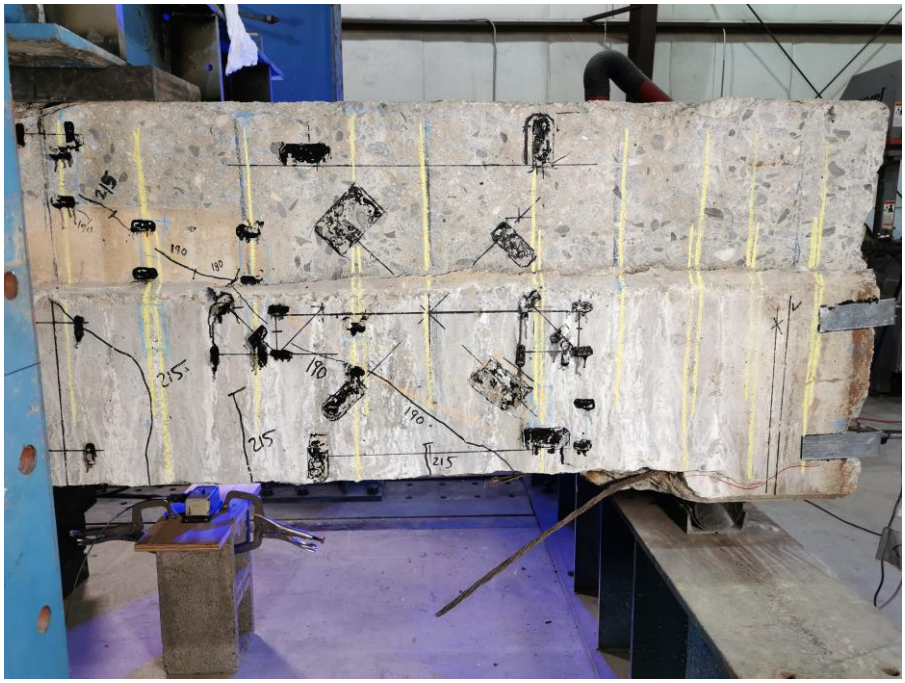

Figure 56 Cracking pattern for the second Aden test

Figure 57 Failure mode for the second Aden test (strands rupturing)

Summary of test results

Table 12 summarizes the results obtained from the four destructive tests discussed previously.

Table 12 Summary of the four tests

	Failure mode	Maximum Load (kip)	Flexural cracking load (kip)	Web-shear cracking load (kip)	a/d
First Lesner	Flexural (crushing)	264.84	141	120	2.629
Second Lesner	Shear	382.44	206	136	1.971
First Aden	Shear	259.19	205	150	2.222
Second Aden	Flexural (wires fracture)	230.53	170.7	150	2.222

5.2. Investigation of the Reinforcement Condition

After completing each test, the concrete at the failure location was chipped off to investigate the condition of the stirrups and strands at that location. In all of the girder ends, the vertical legs of the stirrups were found to be in good condition with no signs of corrosion. This was not unexpected as the girder webs had no surface deterioration. However, in the second Aden end, few stirrups were partially exposed from the bottom of the girder with rust stains in concrete where the horizontal legs intersect with corroded strands as shown in Figure 58. At that location, the girder had a major pre-existing concrete spall with exposed and corroded strands.

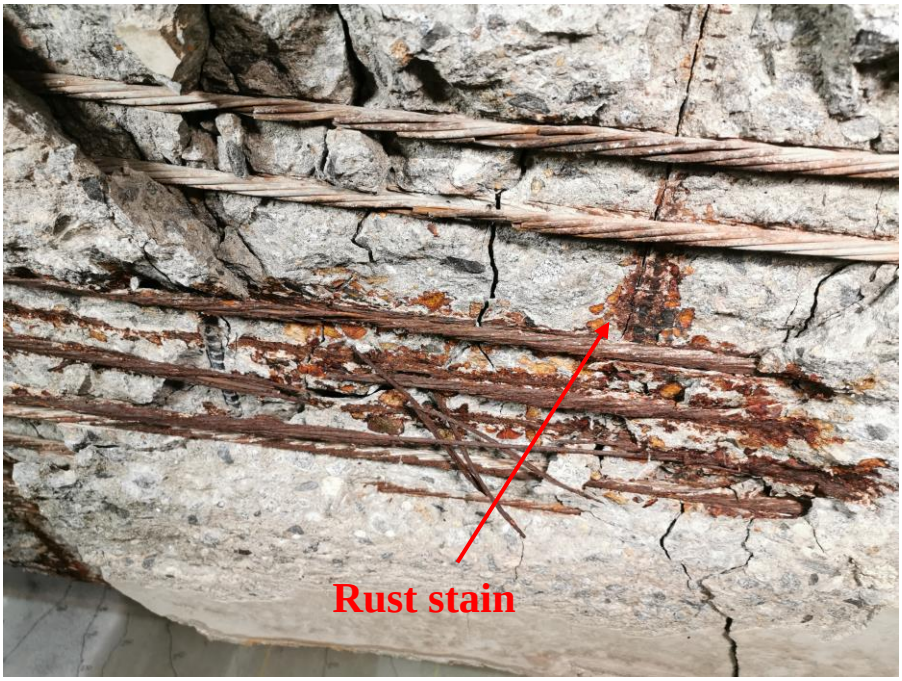

Figure 58 Rust in the horizontal leg of a stirrup in the second Aden end

The strands showed different levels of corrosion for each girder end. Strands that showed signs of corrosion were only in the bottommost and the second bottommost layers of strands. Again, this was anticipated because most of the surface deterioration was in the soffits of the girders near the bottom layers of strands. The level of corrosion for each strand in each girder end is shown in Figure 59.

Strand condition	Color designation
Good condition	Black
Light corrosion	Light green
Medium corrosion	Orange
Heavy corrosion/fractured	Red

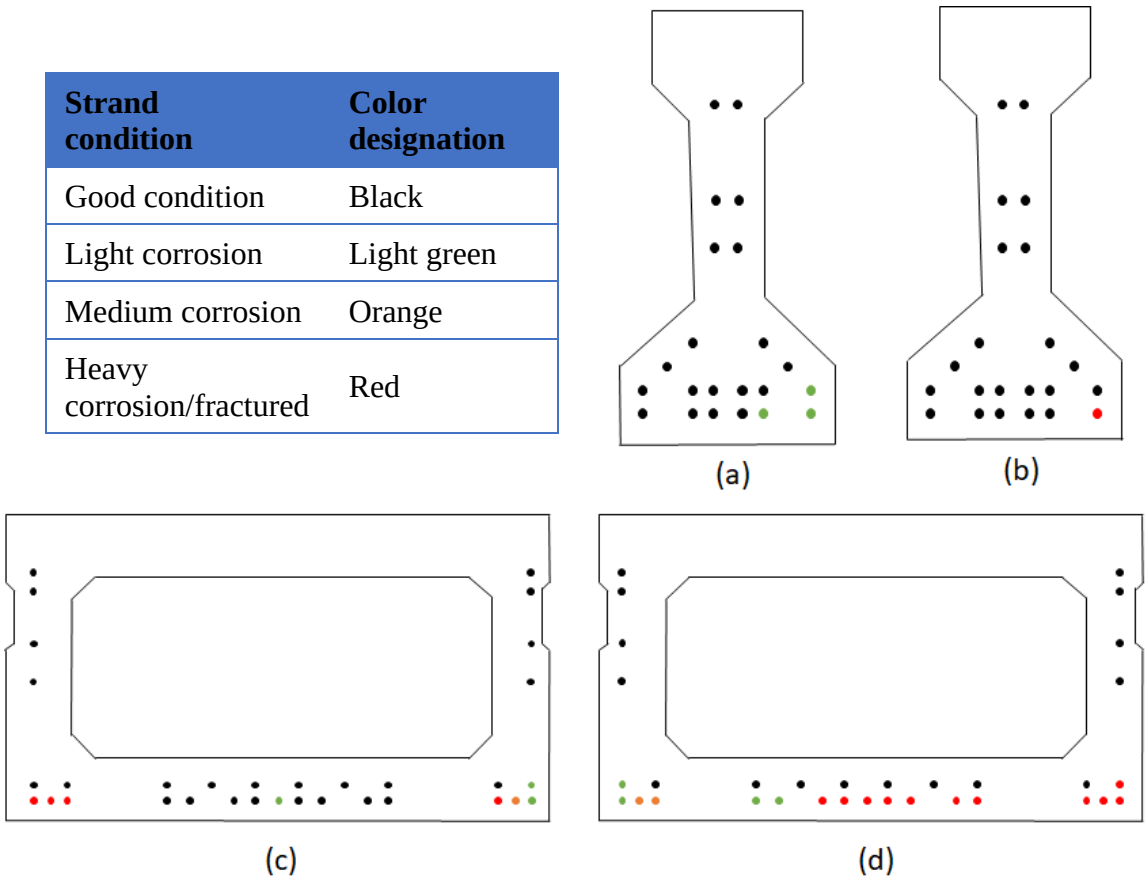

Figure 59 Strands condition after investigation. (a) First Lesner. (b) Second Lesner. (c) First Aden. (d) Second Aden.

By comparing the strands' condition in Figure 59 with the damaged cross-sections, shown in Figure 29 and Figure 30, which were established from visual inspection of the girders, it can be seen that, generally, the level of corrosion in strands correlates to the location and the type of surface deterioration exhibited in the girder. Therefore, recommendations based on visual inspection of the surface damage will be used in the following sections to calculate the flexural and shear strengths of the damaged girders by considering an effective cross-sectional area of any strand adjacent to a surface deterioration such as cracks and section losses. The recommendations that will be used here are those proposed by Naito et al. (2011) and Alfailakawi et al.(2020) outlined in subsection 3.7 and 3.9, respectively. The former will be applied on the Aden girders while the latter will be followed when analyzing the Lesner girder. The Naito et al. recommendations were originally proposed to be used for adjacent box girders. The

applicability of these recommendations was extended to I-beams, such as those in the Lesner Bridge, with some modifications. Comparisons and discussions about the two recommendations are found in (Alfailakawi, 2020).

5.3. Flexural Analysis

The modulus of elasticity for concrete is an important parameter for both flexural and shear analyses. Since, however, no modulus of elasticity test for concrete was performed in the lab, a value of $57000\sqrt{f`_c(psi)}$ was assumed, where the concrete compressive strength was taken from the concrete core tests. To evaluate this assumption, a comparison between the calculated elastic strain profile and measured elastic strain profile is required. The elastic strain distribution was calculated over the depth of the girder using the assumed value for E_c. In Lesner girder, the deck concrete and the prestressing strands were transformed into an equivalent girder concrete using the appropriate modular ratio, n. The measured elastic strain distribution was obtained from the set of horizontal strain gauges placed at the loading location along the length of the girder (subsection 4.5). Comparisons for the Lesner and Aden girders are given in Figure 60 and Figure 61, respectively.

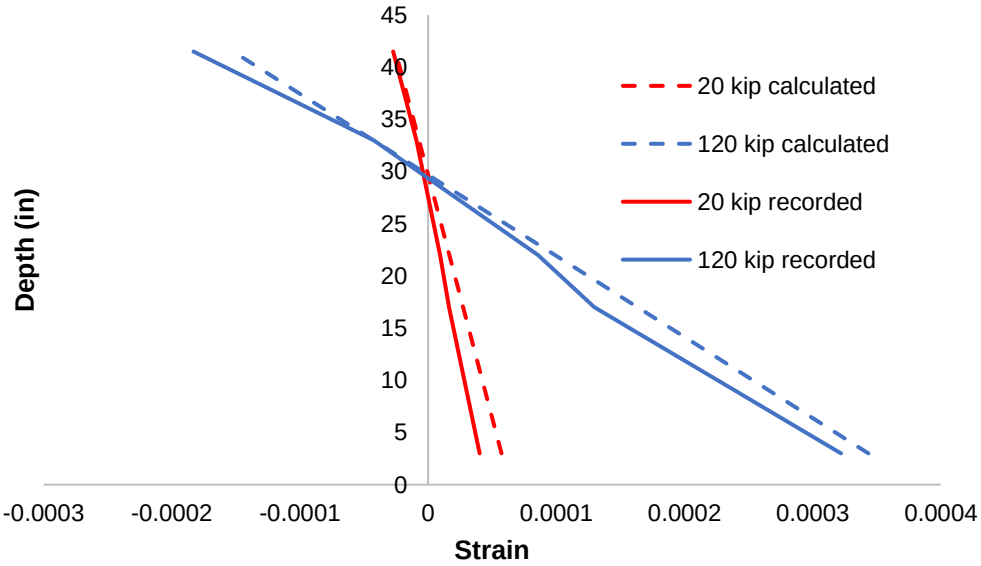

Figure 60 Strain distribution for the Lesner girder (first test)

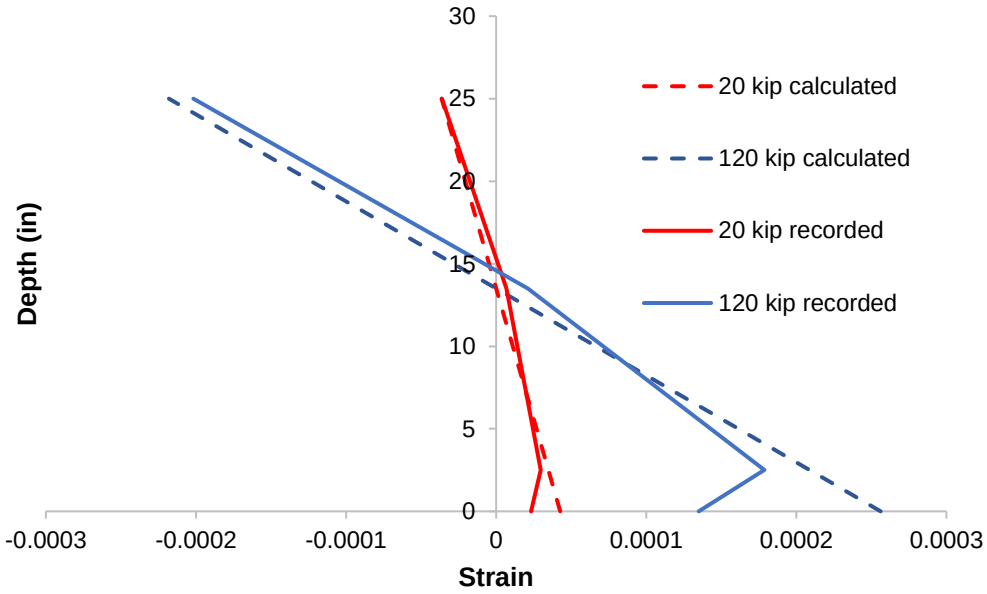

Figure 61 Strain distribution for the Aden girder (first test)

The applied load values used for comparison in Figure 60 and Figure 61 were taken arbitrarily as 20 kip and 120kip for both girders. However, these loads were selected to be less than the cracking load for the girders so that the elastic flexural formula is applicable. The reason for the "kink" present near the bottom of the measured strain distribution for the Aden girder (Figure 61) is not completely known. However, this might be attributed to the fact that the bottommost horizontal strain gauge was placed underneath the girder at the middle of the flange width while the other horizontal strain gauges were placed on the exterior walls of the girder web. Because the load was applied directly on the webs of the girder, this can create an uneven stress distribution over the width of the girder at the loading location, sometimes referred to as shear lag. Based on these comparisons, it can be stated that the values assumed for the modulus of elasticity of concrete for both girders are acceptable.

Another important parameter that needs to be quantified for flexural and shear analyses is the effective prestress in the strands, f_{se}. In the bridge plans, the initial prestress, f_{pi}, was provided. To calculate the effective prestress, long-term losses due to shrinkage, creep, and relaxation of strands need to be accounted for. Several approaches are available in the literature to calculate these losses with different levels of accuracy and simplicity. One method used here is the AASHTO LRFD refined method. The long-

term losses for the two girders are given in Table 5. Another experimental approach is also used in this document. Knowing the applied load value at which the first flexural crack was observed during the test, the effective prestress can be back-calculated at the location of that crack. This effective prestress is denoted by f_{seEx} here and is given below in Table 13. The observed flexural cracking loads in the test are shown in Table 12.

It is important to mention that any strand that was recommended to be taken to 95% of its original cross-sectional area was taken to 100% when back-calculating the effective prestress for the Aden girder. This omission was deemed justifiable for two reasons. First, the recommendations proposed by Naito et al. were suggested to be used to estimate the ultimate flexural strength only and were not examined for the uncracked elastic range. Second, these strands were found to be in good condition when post-testing investigation was performed (Section 5.2). The effective prestress based on the two approaches will be used in analyzing the girders.

Table 13 Prestress for the girders

	Effective Prestress (AASHTO) (ksi)	**Effective Prestress (experimental) (ksi)**
First Lesner	149.7	151.7
Second Lesner		142.0
First Aden	156.7	141.5
Second Aden		160.7

The flexural-cracking load and the flexural capacity of the girders were calculated at the location of maximum moment and shown in Table 14. The table also includes a comparison between the predicted and the observed values, where the observed values are given in Table 12.

The flexural capacity was calculated by assuming plane sections remain plane while the strain at the extreme compression fiber is limited to the crushing strain of concrete, sometimes called the strain compatibility approach. It should be mentioned that these calculations are based on the material properties taken from the laboratory tests. In

addition, the calculation of the flexural strengths and the flexural cracking loads was performed considering both the undamaged and the damaged cross-sectional areas of the strands where the latter was calculated following the recommendations proposed by Naito et al. (2011) and Alfailakawi et al. (2020) (Table 14, damaged strengths are written in red inside parentheses). Again, in the damaged strength calculations, any damage in the girder located within a two-development-length region centered at the section under consideration was considered for strength deduction (Naito et al., 2011).

Table 14 Predicted flexural and flexural-cracking strengths of the girders using tested material properties

		Flexural Strength (kip-ft)	Ultimate Load (kip)	Test/Calc	Cracking Load (kip)	Test/Calc
Using f_{se}	First Lesner	1866(1812)	262.5(254.3)	1.009(1.041)	144.1(138.9)	0.978(1.015)
	Second Lesner	1866(1793)	373.5(358.6)	-----	224.6(215.1)	0.917(0.958)
	First Aden	1480(1343)	357.5(322.7)	-----	235.1(222.2)	0.872(0.923)
	Second Aden	1480(933.5)	354.9(218.0)	0.650(1.058)	242.8(167.4)	0.703(1.020)
Using f_{seEx}	First Lesner	1867(1812)	262.5(254.4)	1.009(1.041)	145.9(140.7)	0.966(1.002)
	Second Lesner	1865(1792)	373.2(358.4)	-----	215.0(206.0)	0.958(1.000)
	First Aden	1476(1341)	337.8(304.9)	-----	216.7(205.0)	0.946(1.000)
	Second Aden	1481(933.9)	360.0(221.2)	0.640(1.042)	247.7(170.4)	0.689(1.002)

Values in parentheses correspond to the damaged, reduced, area of strands

Highlighted cells correspond to the girder ends failed in flexure

In Table 14, the cells highlighted in yellow correspond to the girder ends that failed in flexure. By inspecting the damaged test-to-calculated strength ratio for the girders failed in flexure (inside parentheses), it can by concluded that predicted strengths following the proposed recommendations to account for the corrosion damage almost match the observed strengths from the physical tests with an acceptable margin for safety. When using the effective prestress obtained from the detailed AASHTO losses method for prestress losses, f_{se}, the predicted cracking loads following the recommendations were also close to the values observed in the tests but were unconservative for the second Lesner and the first Aden tests which failed in shear. The discrepancy between the

predicted and the observed cracking loads can be attributed to two facts. First, the recommendations proposed by Naito and Alfailakawi were suggested to be used to estimate the ultimate flexural strength only and were not examined for the uncracked elastic range. Secondly, the cracking load is significantly influenced by the level of the effective prestress in the strands which is not totally understood how it is affected by the corrosion existence in the strands and needs more research. It is intuitive that the predicted cracking loads fairly match the values observed in the tests when using the experimental effective prestress, f_{seEx}, because f_{seEx} was back-calculated based on the first observed flexural crack during the test. A detailed analysis of the girders failed in flexure is given in research by Neeli (2020).

The load-displacement relationship for the first Lesner test is shown in Figure 62. This end of the girder failed due to concrete crush at the top of the deck. The dashed curve lines represent the load-displacement calculated using the virtual load method. The way these plots were constructed was by establishing a moment-curvature relationship for the section then integrating the curvature multiplied by the moment due to a unit applied load at the point of interest over the length of the girder. This process was repeated at multiple stages of loading until the nominal strength of the section. The integration was performed numerically with the aid of an excel spreadsheet. The black dashed curve represents the load-displacement for the girder taking the full, undamaged, cross-sectional area of the strands while the red dashed curve represents the load-displacement for the girder following the recommendations provided by Alfailakawi (2020). From Figure 62, it can be noticed that the actual stiffness of the girder was not affected by the minor corrosion damage existed near that end of the girder (Figure 27).

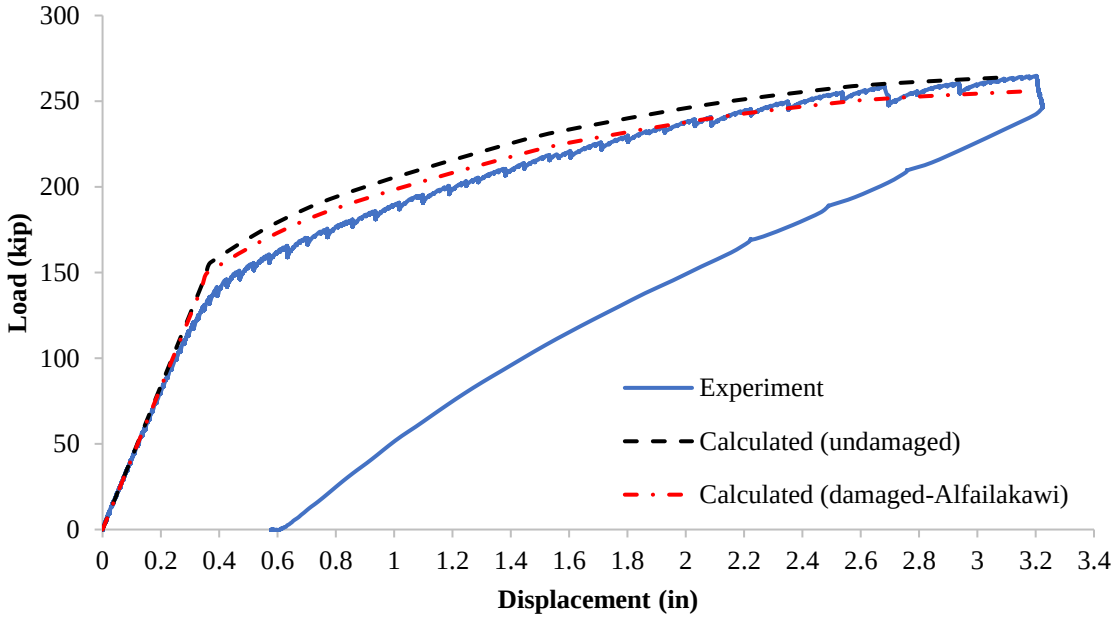

Figure 62 Load-Displacement for the first Lesner test

In the second Aden test, the failure mode was progressive rupture of the strand wires until reaching an excessive deflection at which the test was stopped. Therefore, a single Load-Displacement curve ending with concrete crushing would not the appropriate way to describe the behavior of the girder during that test. Instead, multiple curves were constructed assuming a certain number of strands had been completely lost for each curve from the beginning of the test. These curves are shown dashed lines in Figure 63. The topmost curve represents the behavior of the girder if all strands were intact throughout the test. The bottommost curve represents the behavior of the girder if 18 strands had been lost or fractured since the beginning of the test. The other curves represent the behavior of the girder with an intermediate number of the lost strands.

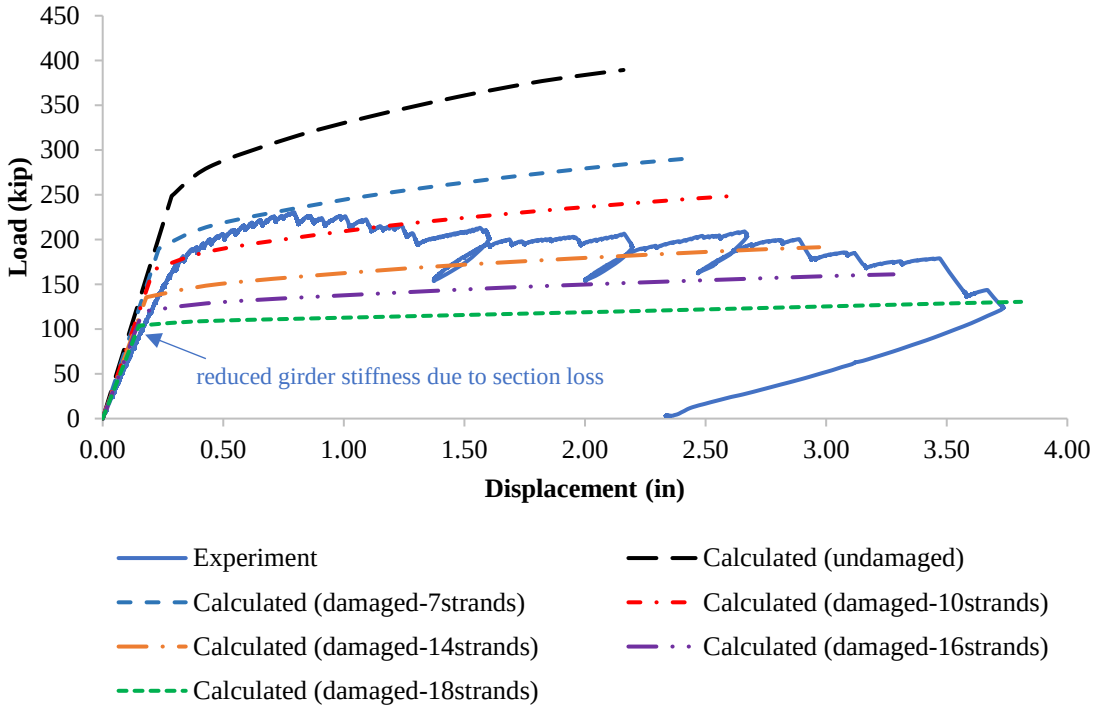

Figure 63 Load-Displacement for the second Aden test

By tracing the actual Load-Displacement curve, it can be seen that the girder behavior closely followed the calculated Load-Displacement curve with 7 strands completely lost (the blue dashed curve). This seems reasonable because the girder had three broken strands and six exposed and corroded strands prior to the test. When the load reached to 230.53 kip (0.8 in. deflection), the strands ruptured progressively and the load kept dropping to the next calculated Load-Displacement curve until the test was stopped. The condition of the bottommost layer of strands is shown in Figure 57(b). In addition, Figure 63 suggests that the actual stiffness of the girder was influenced by the pre-existing damage in the girder. This was expected during the test because the bottom concrete cover was severely cracked, and missing in some parts along the length, as shown in Figure 56. Therefore, the moment-curvature and the Load-Displacement relationships were reconstructed with the bottom concrete cover being completely ignored to account for the reduced moment of inertia of the girder. These new Load-Displacement curves are shown in Figure 64.

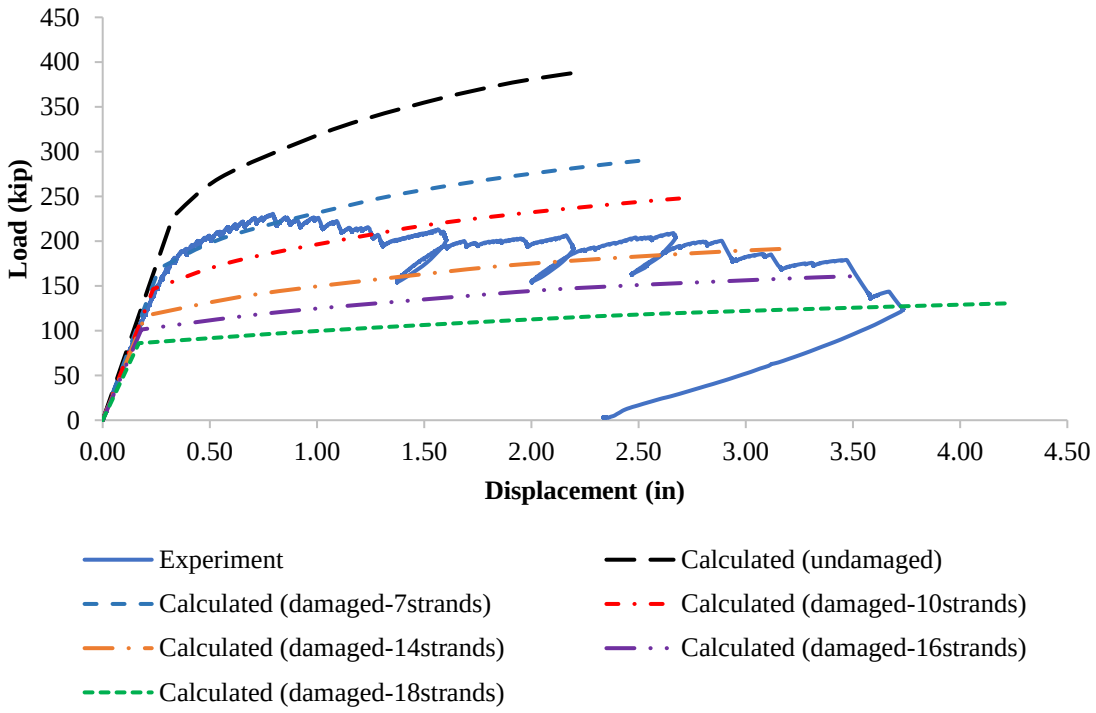

Figure 64 Load-Displacement for the second Aden test (bottom concrete cover is removed)

5.4. Shear Analysis

One key parameter in shear analysis is the cross-sectional area of the shear reinforcement. When corrosion exists in the shear reinforcement, the shear strength contribution provided by the steel is reduced due to the loss in the cross-sectional area (Higgins et al., 2003). As previously mentioned in section 5.2, the stirrups crossed the critical shear crack were found to be in a good condition in all of the tested ends regardless of the amount of corrosion existed in the longitudinal reinforcement. Therefore, the effective cross-sectional area of the shear reinforcement was taken to 100% of the original cross-sectional area when calculating the shear strength of the section provided by the shear reinforcement, V_s. Another key parameter in shear analysis is the width of the web of the girder. When corrosion-induced cracks exist in the web, the shear strength contribution provided by the concrete is reduced due to the reduction in the effective width of the web (Higgins et al., 2003; El-Sayed, 2014). Because there was no noticeable damage on the girder webs, the full width of the web was considered when

calculating the shear strength provided by the concrete section, V_c. Hence, the only factor that may influence the shear strength, in the scope of this research, is the amount of the remaining prestress force in the strands. When using the MCFT, a larger prestress force results in a smaller axial strain, ε_s, which will in turn increase the coefficient of the shear strength provided by the concrete, β, as shown in Eq.(38) and Eq.(39). In addition, a smaller axial strain results in a flatter angle of inclination, θ, engaging more stirrups in shear resistance as shown in Eq.(41). When using the V_{ci}-V_{cw} method, a larger prestress force results in higher compressive stresses f_{pe} and f_{pc} which in turn increase the shear strengths provided by the concrete V_{ci} and V_{cw}, respectively as shown in Eq.(9) and Eq.(13).

The shear strength of each girder was calculated at the critical section for shear and shown in Table 15. The table also includes a comparison between the predicted and the observed values, where the observed values are given in Table 12. The shear strength was calculated using the three sectional methods discussed in Section 2.2. In addition, the shear strength was also calculated using the sectional analysis software developed at the University of Toronto, Response 2000. Much detail can be found in dissertation by Bentz (2000). It should be mentioned that these calculations are based on the material properties taken from the laboratory tests. In addition, the calculation of the shear strengths was performed considering both the undamaged and the damaged cross-sectional areas of the strands where the latter was calculated following the recommendations proposed by Naito et al. (2011) and Alfailakawi et al. (2020) (In Table 15, damaged strengths are written in red inside parentheses). Similar to the flexural strength calculations, any damage in the girder located within a two-development-length region centered at the section under consideration was considered for strength deduction. In Table 15, the effective prestress was taken based on the refined AASHTO method for prestress losses. It was found that using the experimental effective prestress, f_{seEx}, in calculating the shear strength would result in similar values.

Table 15 Predicted shear strengths using the tested material properties

Test	Failure mode	Load at failure (kip)	Shear at failure (kip)	AASHTO A5.8.3.4.2			
				V_c (kip)	V_s (kip)	V_n (kip)	Test/Calc
First Lesner	Flexural (crushing)	264.8	235.9	48.94 (46.83)	183.7 (181.1)	232.6 (227.9)	1.014 (1.035)
Second Lesner	Shear	382.4	318.3	48.94 (46.14)	183.7 (180.2)	232.6 (226.3)	1.368 (1.406)
First Aden	Shear	259.2	257.6	79.20 (77.06)	118.4 (117.8)	197.6 (194.9)	1.303 (1.322)
Second Aden	Flexural (wires fracture)	230.5	224.2	79.20 (61.68)	118.4 (112.7)	197.6 (174.3)	1.134 (1.286)

AASHTO Appendix B5			
V_c (kip)	V_s (kip)	V_n (kip)	Test/Calc
33.58 (33.47)	190.4 (189.8)	224.0 (223.2)	1.053 (1.057)
33.58 (33.43)	190.4 (189.5)	224.0 (222.9)	1.421 (1.428)
40.14 (40.14)	135.5 (135.5)	175.6 (175.6)	1.467 (1.467)
40.14 (39.38)	135.5 (127.4)	175.6 (166.7)	1.277 (1.344)

ACI Vci-Vcw			
V_c (kip)	V_s (kip)	V_n (kip)	Test/Calc
107.9 (107.5)	118.1 (117.5)	226.0 (225.0)	1.044 (1.048)
103.3 (102.8)	118.1 (117.3)	221.4 (220.1)	1.438 (1.446)
130.5 (126.0)	71.79 (71.79)	202.3 (197.8)	1.273 (1.302)
130.5 (113.4)	71.79 (71.79)	202.3 (185.2)	1.108 (1.21)

Response2000	
V_n (kip)	Test/Calc
237.0 (234.8)	0.995 (1.005)
237.2 (235.0)	1.342 (1.354)
204.7 (204.4)	1.258 (1.26)
204.8 (190.8)	1.095 (1.175)

In Table 15, the cells highlighted in yellow correspond to the girder ends that failed in shear. By inspecting the test-to-calculated shear strength ratios, it can by concluded that all the shear analysis methods underestimated the shear strength with a shear strength ratio V_{test}/V_{calc} (1.26-1.47). This margin is comparable to the mean shear strength ratio obtained in the NCHRP Report-549 (1.27-1.44) when the AASHTO LRFD method was used to determine the shear strength for a database composed of 1359 reinforced concrete and prestressed concrete beams. In Kassner (2012), the average shear strength ratio was 1.67, 1.62, and 1.34 when the AASHTO A5.8.3.4.2, the AASHTO Appendix B5, and the V_{ci}-V_{cw} methods were used to determine the shear strength of two prestressed normal-weight concrete girders. In addition, by comparing the two values in each highlighted cell in Table 15, it can be noticed that considering the damaged cross-sectional area of the strands in determining the shear strength has an insignificant effect on the nominal shear capacity. On average, at the critical section for shear, the AASHTO Appendix B5.2 was the most conservative method, while the ACI V_{ci}-V_{cw} and the AASHTO A5.8.3.4.2 resulted in similar but slightly less conservative shear capacities. The high level of conservatism is thought to be a consequence of the small shear span-to-depth ratio used in the shear tests. Girders with small shear span-to-depth ratios resist the load mainly by the arching action. Indeed, strut-and-tie modelling was found to be the most accurate tool to predict the shear capacity of girders with loads applied near the end regions, which will be discussed in a subsequent section.

The shear strengths of the two girder ends that failed in shear were plotted along the shear span using the three sectional shear analysis methods as shown in Figure 65 and Figure 66. The shear strength and the shear demand were plotted for the actual failure load reached in the physical shear test. It can be seen that all the shear methods indicate that the girder had inadequate shear strength along the entire shear span under the actual failure load. Thus, it is suggested that the sectional shear analysis methods are not used to evaluate the shear strength for girders with shear span-to-depth ratios of less than 2.5.

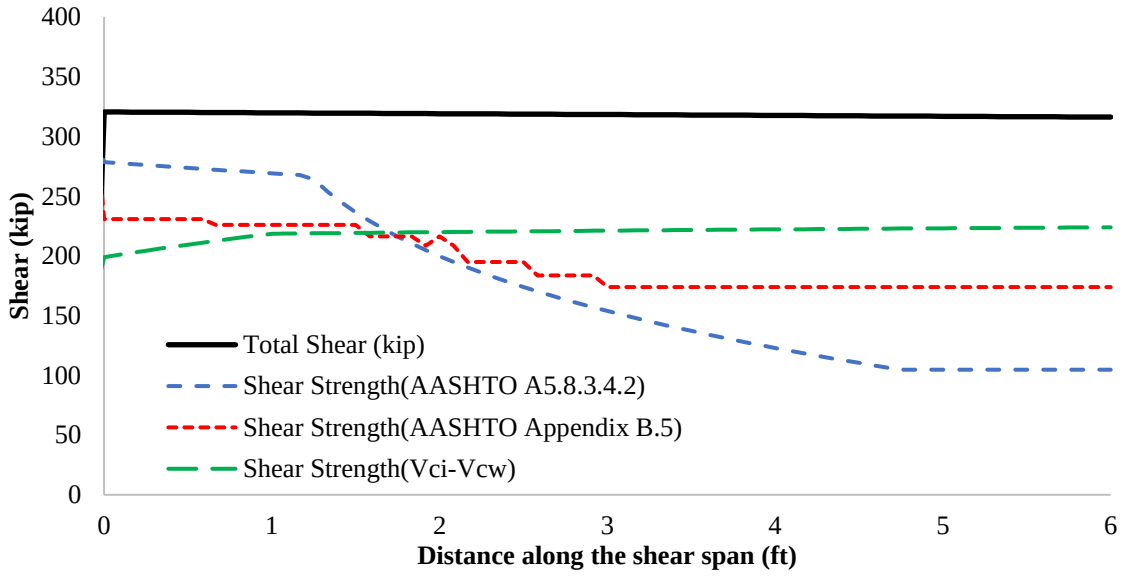

Figure 65 Shear strength and demand for the second Lesner test under the observed failure load

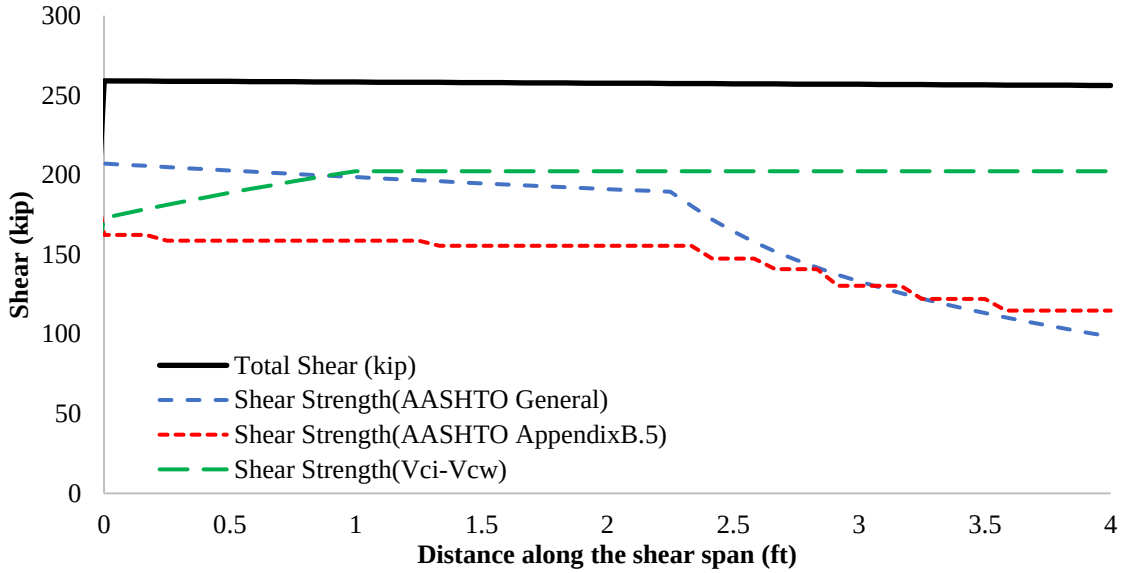

Figure 66 Shear strength and demand for the first Aden test under the observed failure load

Experimental Estimation of the shear Strength using the MCFT

The sectional shear strengths shown in Table 15 were based on the current AASHTO and ACI codes. In this subsection, the sectional shear strengths of the girders

are estimated experimentally in light of the MCFT using the data recorded during the tests by the instrumentation, discussed in Section 4.5. In this experimental approach, the concrete shear strength factor, β, was calculated using the formula given in Eq.(29), where the average principle strain, ε_1, and the principle angle, θ, were obtained indirectly from the DIC and the BDI measurements. First, the shear strain, ε_{xy}, and the normal strain in both directions, ε_{xx} and ε_{yy}, were calculated at the center of the rosette using the LVDT and the DIC measurements as follows

$$\varepsilon_{xx} = \varepsilon_0 + \varepsilon_{pre} \tag{49}$$

$$\varepsilon_{yy} = -\varepsilon_0 + \varepsilon_{-45} + \varepsilon_{45} \tag{50}$$

$$\varepsilon_{xy} = -0.5\,\varepsilon_{-45} + 0.5\,\varepsilon_{45} \tag{51}$$

where the subscript in each term of the above equations represents the direction at which the LVDT, or the DIC extensometer, was oriented with respect to the longitudinal axis. ε_{pre} is the axial strain existed in the concrete at the center of the rosette before the test due to the girder self-weight, the deck weight, and the prestress force. This strain can be calculated as follows

$$\varepsilon_{pre} = \frac{1}{E_c}\left[\frac{-P_e}{A_{bare}} + \frac{P_e\, e\, y_{rosette}}{I_{bare}} + \frac{(M_{girder} + M_{deck})\, y_{rosette}}{I_{bare}}\right] \tag{52}$$

where $y_{rosette}$ is the distance between the centroid of the bare girder and the center of the rosette taken positive when the center of the rosette is above the centroid. Second, the principle strains and angle can then be determined using the following strain transformations

$$\varepsilon_1 = \frac{\varepsilon_{xx} + \varepsilon_{yy}}{2} + \sqrt{\left[\frac{\varepsilon_{xx} - \varepsilon_{yy}}{2}\right]^2 + \left[\varepsilon_{xy}\right]^2} \tag{53}$$

$$\varepsilon_2 = \frac{\varepsilon_{xx} + \varepsilon_{yy}}{2} - \sqrt{\left[\frac{\varepsilon_{xx} - \varepsilon_{yy}}{2}\right]^2 + \left[\varepsilon_{xy}\right]^2} \tag{54}$$

$$\theta_p = \frac{1}{2}\tan^{-1}\left[\frac{2\,\varepsilon_{xy}}{\varepsilon_{xx} - \varepsilon_{yy}}\right] \tag{55}$$

Appendix-B.1 shows the principle strains, the principle angle, and the concrete shear strength factor, β, for the two girder ends failed in shear using the experimental data. The steel contribution to the shear strength, V_s, was estimated in a way similar to

that described in the NCHRP Report-579. This approach starts by selecting a critical, or boundary, shear crack. The critical shear crack is the widest shear crack near the failure location. When multiple cracks satisfy this condition, the critical shear crack to be selected is the one closest to the critical section for shear (Hawkins et al., 2007). The critical shear cracks for the girder ends failed in shear are shown in Figure 67 and Figure 68. Since wide shear cracks developed in the two girders that failed in shear during the test, it was assumed that all the stirrups crossed by the critical shear crack had yielded when the girder failed. Thus, V_s can by calculated by multiplying the number of stirrups across the critical shear crack by the strength of a single stirrup, $A_v f_y$.

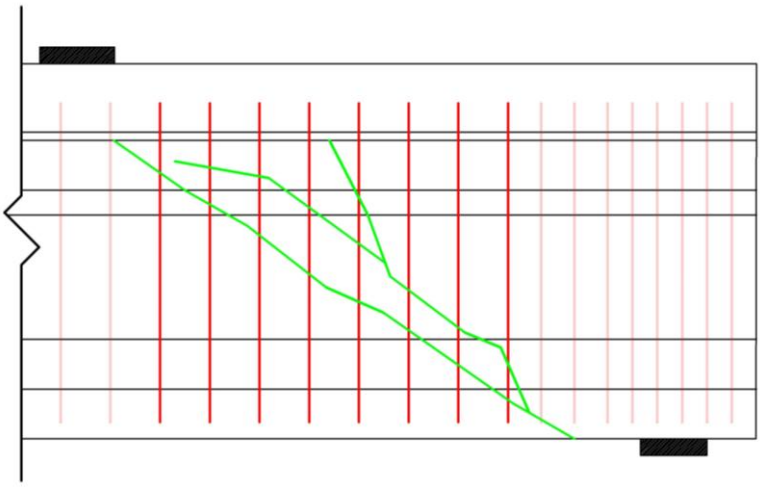

Figure 67 Stirrups crossed by the critical shear crack (Second Lesner Test)

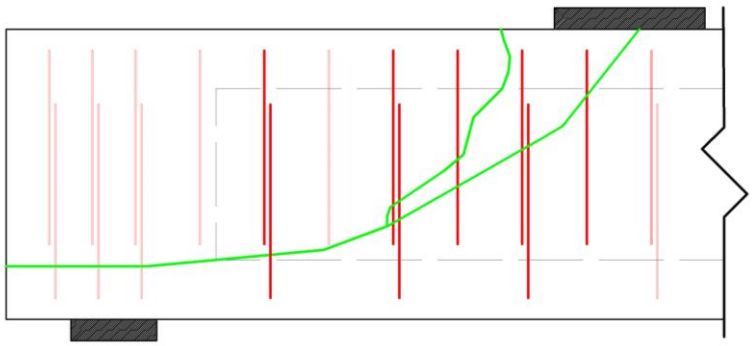

Figure 68 Stirrups crossed by the critical shear crack (First Aden Test)

Finally, the shear strength of a girder is obtained by summing the concrete and the steel contributions to the nominal shear strength. Figure 69 and Figure 70 show the experimental shear strength of the girder ends failed in shear. It should by mentioned that

the ending of the shear strength curves in the figures corresponds to the instant at which the instruments were removed for safety purposes and not necessarily the end of the test. The shear demand and the shear capacity of the girder ends based on this approach are provided in Table 16.

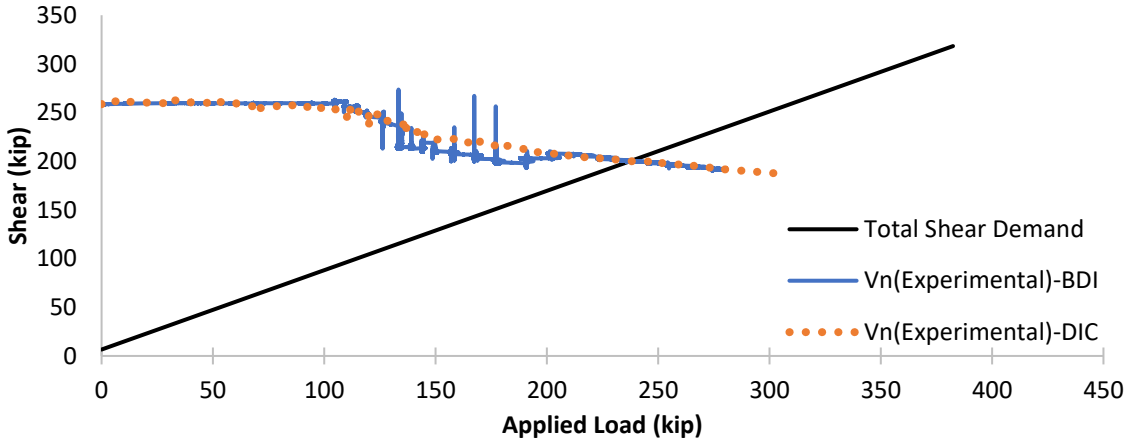

Figure 69 Shear strength of the second Lesner end at the middle of the shear span using an experimental approach

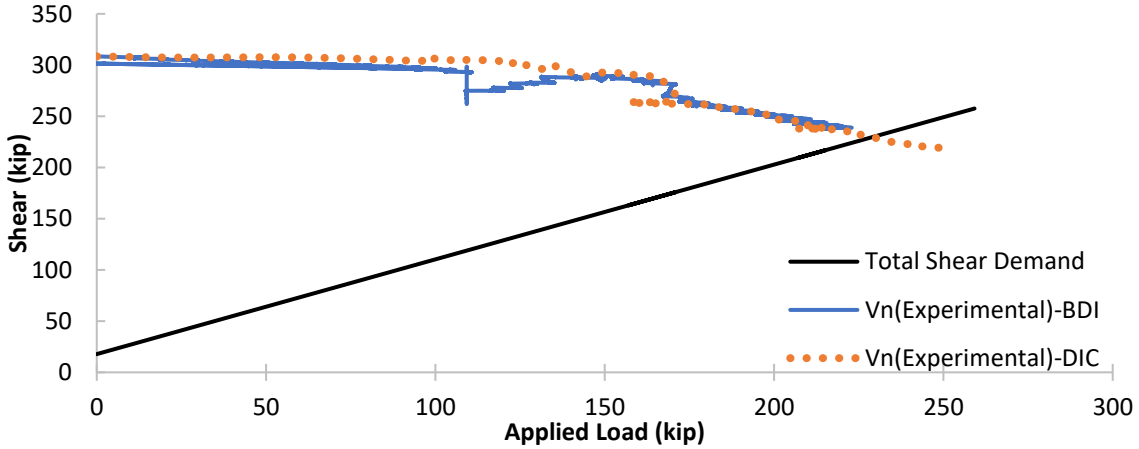

Figure 70 Shear strength of the first Aden end at the middle of the shear span using an experimental approach

Table 16 Predicted shear strengths of the girder ends failed in shear at the middle of the shear span using an experimental approach

	Shear demand at failure (kip)	Shear strength at failure (kip)	$V_{test}/V_{predict}$
Second Lesner	318.3	187.3	1.699
First Aden	257.6	218.9	1.176

From Figure 69 and Figure 70, the shear strength ratios of the second Lesner test and the first Aden test are 1.699 and 1.176, respectively, when the experimental approach for V_n is used. It can be observed that the shear strength ratio of the second Lesner test is still quite high indicating that the shear strength of girders with shear span-to-depth ratios of less than 2.0 are very conservative when predicted by the sectional shear methods. Therefore, analyses for the both girder ends were performed using the Strut-and-Tie Model approach in the subsequent section.

Strut-Tie Model

In this section, the STM is used as an anlysis tool to predict the strength of the second Lesner and the first Aden ends which failed in shear. The STM established for the girders were based on the ACI318-19 code. In this analysis, the tension stiffening of the concrete is completely ignored and the tie forces are carried by the reinforcement alone. In addition, the self-weight of the girder and the deck weight were ignored as they were comparetively insignificant. STMs for the two girder ends were established following the guidelines discussed in Section 2.2.3. To reiterate, the angle between any strut and node was was taken not less than 25 degrees. The geometries of discrete, non-smeared, nodes were determined based on the available dimesnions of the bearing pads and the location of the flexural tension or compression forces intersecting a node. The geometries of struts were determined based on the width of the member and the strut-to-node interface. Finally, the number of stirrups counted in a vertical tie was determined following the

guidelines by Williams et al. (2012) and illustrated in Figure 20. Because the girders at hand can be classified as deep beams, the load is transferred by a combination of an arch action and a truss action. The two final STMs for the girders under the same loading condition during the tests are shown in Figure 71 and Figure 72. The red lines represent the ties while the dashed blue lines represent the struts. Intermediate steps to establishing these STMs can be found in Appendix-B.2. It can be seen that the arch action in these figures are represneted by the strut running between the applied load and the support, strut A-H.

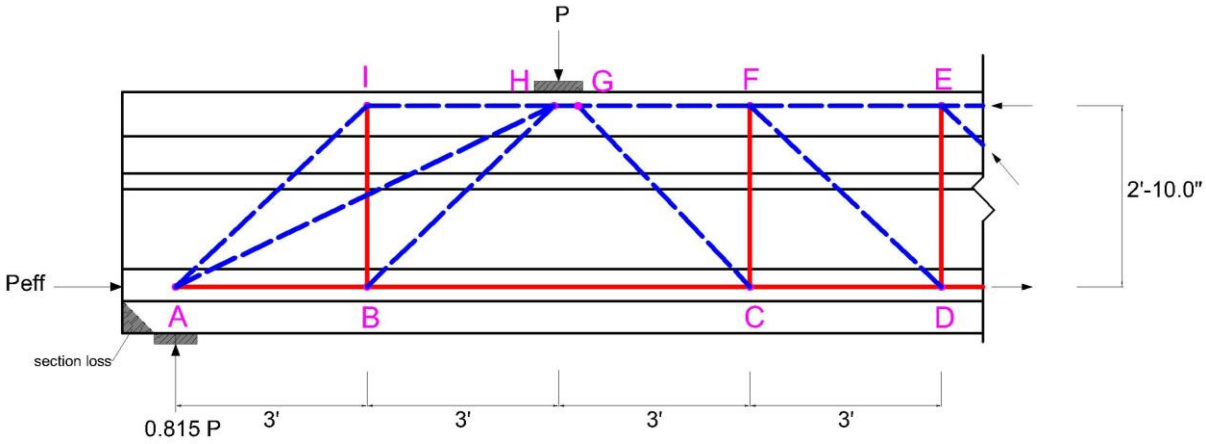

Figure 71 STM for the second Lesner test

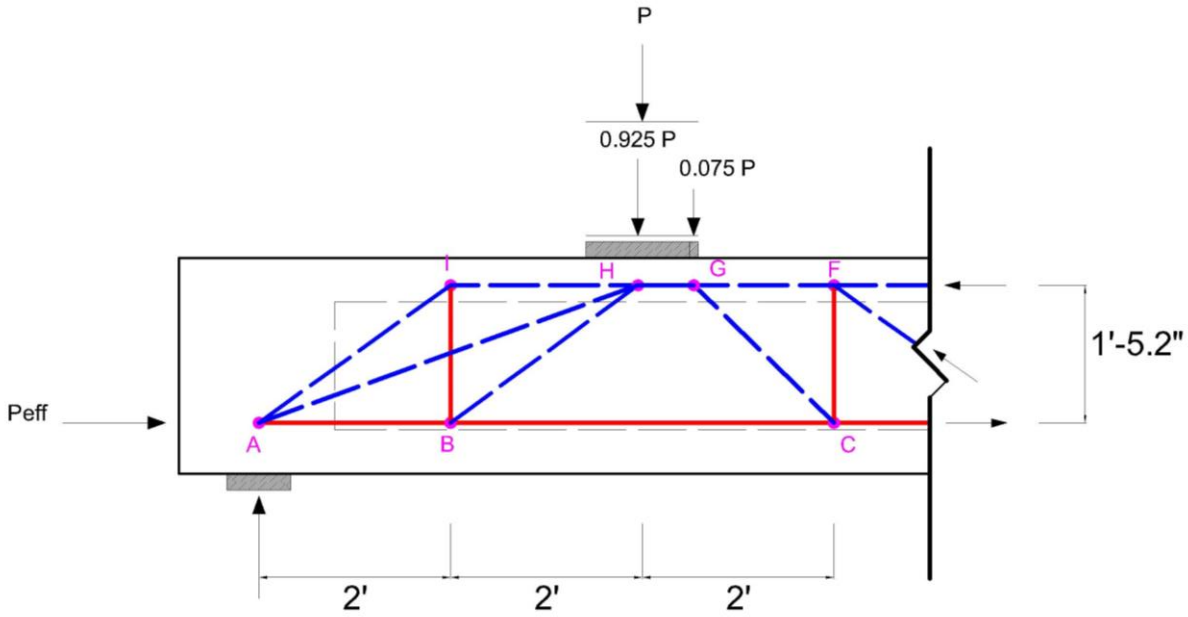

Figure 72 STM for the first Aden test

The STMs shown in Figure 71 and Figure 72 are made up of two superposed statically determinate trusses as illustrated in Figure 73. Truss-1, Figure 73 (b), represnts the resistance mechanism provided by the truss action, while Truss-2, Figure 73 (c), represnets the resistance mechanism provided by the arch action. Each of these trusses was analyzed independantly as discussed in the following paragraph.

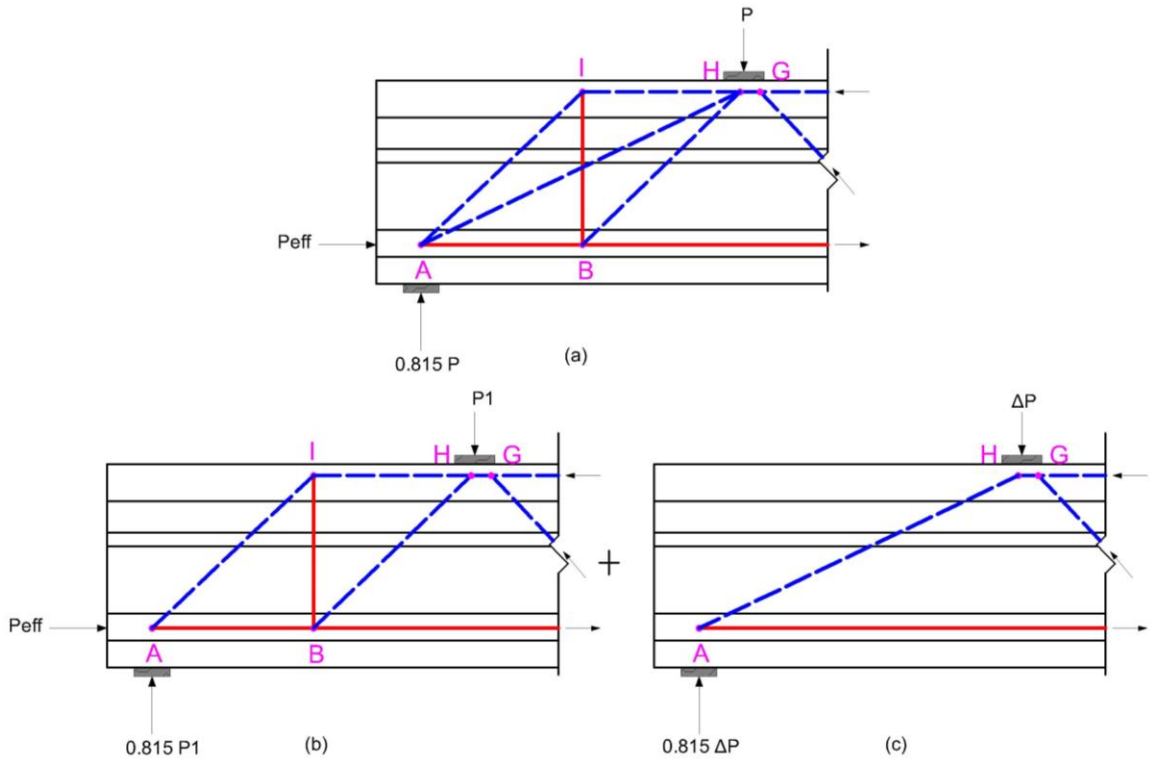

Figure 73 STM for the second Lesner test. (a) combined action. (b) Truss action (Truss-1). (c) Arch action (Truss-2).

First, a load, *P1*, was applied on *Truss-1* until the vertical tie *B-I*, resisted by vertical stirrups in the panel, reached its capacity. In this analysis, an elasto-plastic material law was assumed for the shear reinforcement. After the stirrups yielded, the vertical tie *B-I* was removed along with the effective prestressing force and the struts framing into that tie and any additional load can be carried now by the arch action only in *Truss-2*. An additional load, ΔP, was applied on *Truss-2* until the diagonal strut crushed. Finally, the maximum total load that the system can carry can be found as follows

$$P_{max} = P_1 + \Delta P \qquad (56)$$

The capacity of the struts were evaluated based on Eq.(45) and Eq.(46) at the strut-to-node interface. The geometry of the interfaces for Truss-1 and Truss-2 in each girder is given in Figure 74 and Figure 75. In the *CCT* nodes in the Lesner STM and the *CCC* nodes in the Aden STM, it can be observed that the member width, the bottom bulb in the Lesner girder and the top flange in the Aden girder, is varying along the strut-to-node interface. Therefore, the interface was divided into segments such that each segment had a uniform member width along its length. In the Lesner CCT node, the member width of the intermediate segment was taken as the average between the bottom flange width and the web width. Then, the area of the interface can be calculated by summing the products of the segment length multiplied by the appropriate member width.

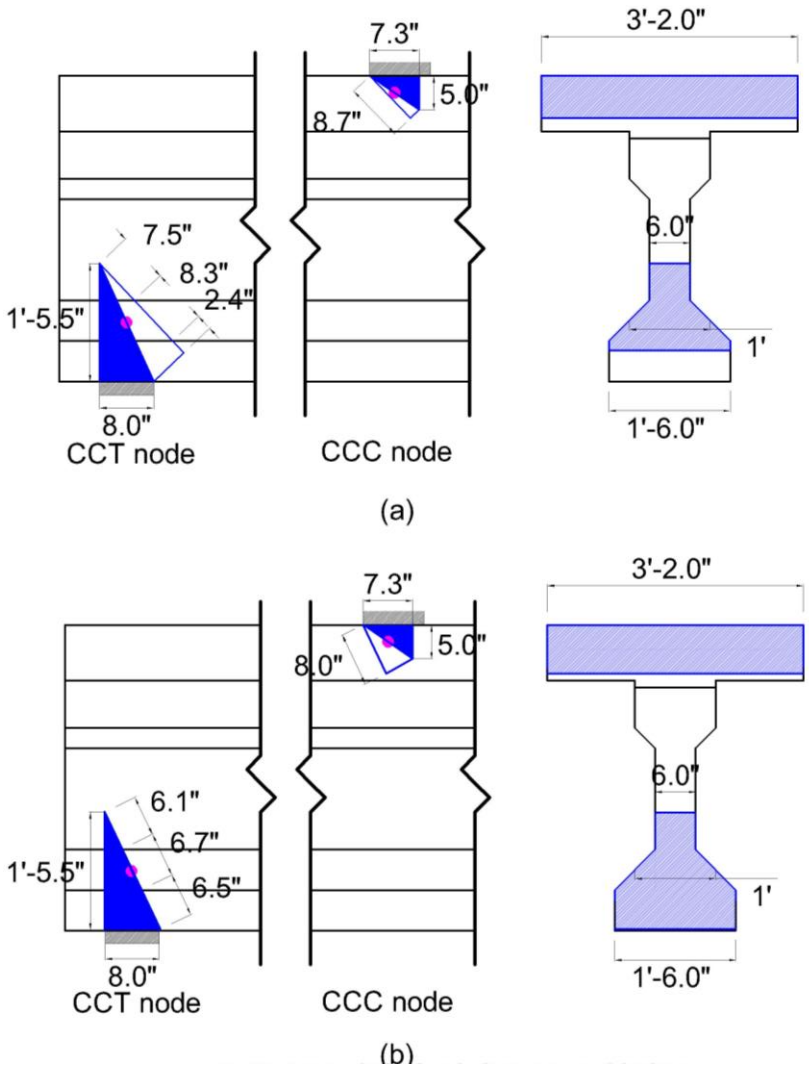

Figure 74 Discrete node geometries for the second Lesner test. (a) Truss-1. (b) Truss-2.

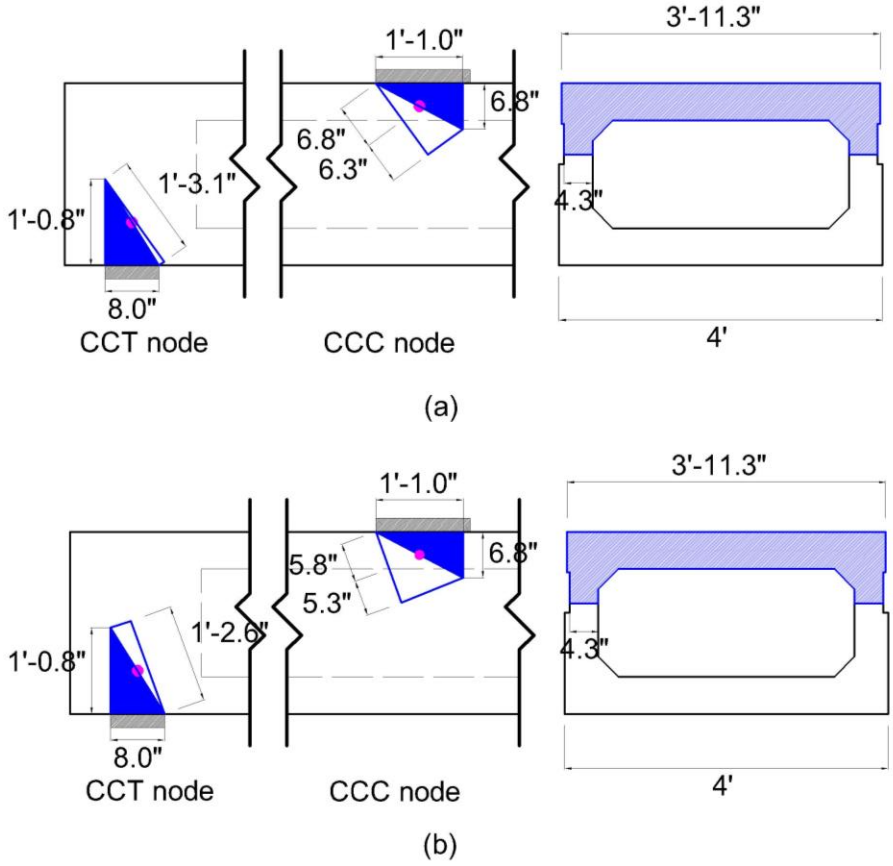

Figure 75 Discrete node geometries for the second Lesner test. (a) Truss-1. (b) Truss-2.

After the total load was determined, the force demand on the horizontal tie *A-B*, resisted by the strands, was calculated under the total applied load on the girder to ensure that the strands can develop that amount of force. The stress in the strands is assumed to build up linearly from zero to f_{se} within the transfer length, and from f_{se} to f_{ps} within the development length minus the transfer length as shown in Figure 16. Table 17 shows the strength of each element in the STM for the second Lesner test and the required applied load on the girder to fail it.

Table 17 STM results for the second Lesner test

Truss 1				Truss 2			
Element		**Strength (kip)**	**Load to fail (kip)**	**Element**		**Strength (kip)**	**Load to fail (kip)**
CCT Node	Strut-Node Interface	633.0	533.3	CCT Node	Strut-Node Interface	788.8	417.0
	Bearing face	485.4	595.6		Bearing face	485.4	595.6
CCC Node	Strut-Node Interface	2299	1959	CCC Node	Strut-Node Interface	2114	1118
	Bearing face	710.6	871.9		Bearing face	710.6	871.9
	Back face	1321	1531	Strut A-H	support end	364.0	192.5
Strut A-I		345.1	290.7		load end	707.9	374.3
Strut B-H		769.8	656.2	Horizontal Tie		405.9	167.8
Strut H-I		660.5	765.4				
Vertical Tie		155.2	190.4				
Horizontal Tie		340.6	446.5				
STM strength controlled by the horizontal tie (kip)				**358.2**			
STM strength controlled by the strut crushing (kip)				**382.9**			

From Table 17, the first element in *Truss-1* to be overloaded is the vertical tie at an applied load of 190.4 kips. *Truss-2* can attain an additional load of 167.8 kips which is controlled by the amount of force that the horizontal tie reinforcement can develop at the critical section, where the tie exits the extended nodal zone, as shown in Appendix-B.2. In this case, the total load-carrying capacity of the STM is 358.2 kips. However, since this particular girder end failed in diagonal crushing, it is of interest to investigate the load-carrying capacity of *Truss-2* if controlled by crushing of the diagonal strut *A-H*. From the table, the additional load required to crush strut *A-H* is 192.5 kips resulting in a total load-carrying capacity of 382.9 kips which is almost the load observed during the test when the girder failed. Figure 76 shows that the force demand on the horizontal tie reinforcement is a little higher than what can be developed by the strands at the critical section, where the tie exits the extended nodal zone. This high force demand can be attributed to two possible reasons. The first reason is that the available tendon force in

Figure 77 was plotted based on the transfer length and the development length of the strands calculated from the AASHTO LRFD equations. In the literature, there is a controversy on whether these equations result in conservative, longer, transfer and development lengths in some situations. Since, however, no strand slip was observed during the test, it is reasonable to assume that the calculated transfer and development lengths are conservative and the strands were able to develop the demand force when the diagonal strut crushed. Secondly, in fact, some of the tension force demand on the horizontal tie is resisted by the uncracked concrete, tension stiffening, which is completely ignored in this analysis.

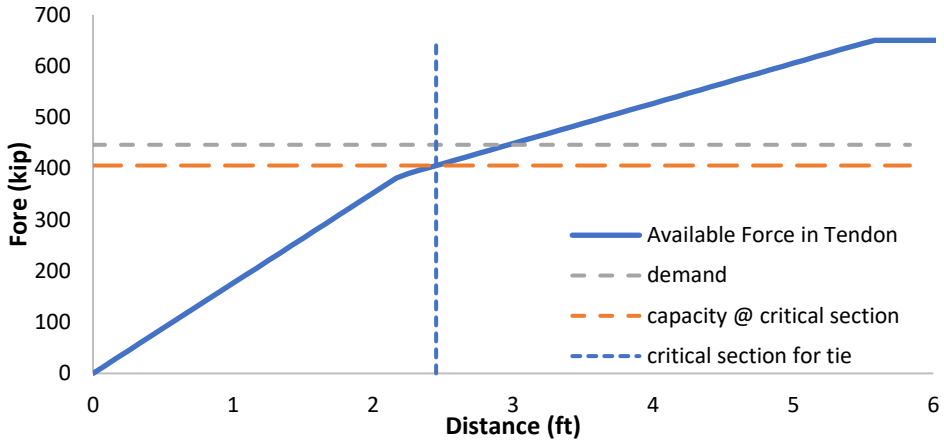

Figure 78 Capacity and demand on the horizontal tie for the strut crushing load (second Lesner test)

Table 18 shows the strength of each element in the STM for the first Aden test and the required applied load on the girder to fail it.

Table 18 STM results for the first Aden test

Truss 1				Truss 2			
Element		**Strength (kip)**	**Load to fail (kip)**	**Element**		**Strength (kip)**	**Load to fail (kip)**
CCT Node	Strut-Node Interface	2997	1887	CCT Node	Strut-Node Interface	2897	1066
	Bearing face	1588	1716		Bearing face	1588	1716
CCC Node	Strut-Node Interface	3088	1971	CCC Node	Strut-Node Interface	2628	967.4
	Bearing face	1924	2080		Bearing face	1924	2080
Strut A-I		312.1	196.6	Strut A-H	support end	301.8	111.1
Strut B-H		430.9	275.1		load end	368.4	135.6
Vertical Tie		119.7	129.4	Horizontal Tie		595.0	195.7
Horizontal Tie		491.3	436.3				
STM strength controlled by the horizontal tie				**240.4**			

From Table 18, the first element in *Truss-1* to be overloaded is the vertical tie at an applied load of 129.4 kips. *Truss-2* can attain an additional load of 111.1 kips which is controlled by the crushing of the diagonal strut *A-H*, at the end closer to the support, resulting in a total load-carrying capacity of the STM of 240.4 kips. In this case, the test-to-calculated strength ratio is 1.078. At this level of applied load, Figure 79 shows that the force demand on the horizontal tie reinforcement can be developed at the critical section, where the tie exits the extended nodal zone.

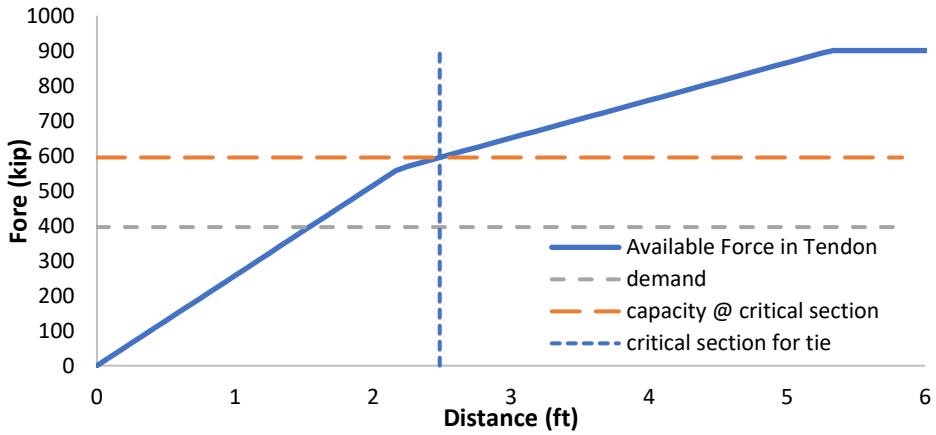

Figure 79 Capacity and demand on the horizontal tie for the strut crushing load (first Aden test)

5.5. Comparison to Finite Element Analysis

Finite element models were created for the girder ends failed in shear using truss elements. While beam elements in finite element models are usually used to predict the flexural capacity, truss elements can be used to predict the shear capacity. These models were created in ongoing research by Aliasghar-Mamaghani (in press) to study the corrosion effect on prestressed concrete girders. This was pursued by creating two models for each corroded girder. The first model, *Model-1*, represents the actual condition of the girder accounting for the existing corrosion damage by reducing the cross-sectional area of the strands. This model was validated against the physically tested girders. Refinements were made to the model to capture the capacity, the failure mode, and the stiffness, if possible, of the girder using the data recorded from the physical tests. The second model, *Model-2*, represents the original condition of the girder without any damage imposed on the strands. Results from the FE analyses are shown in Table 19.

Table 19 Finite element analysis results for the girder ends failed in shear (Aliasghar-Mamaghani, in press)

	Load (kip)				
	Experiment	**Model-1**	**Model-1/Experiment**	**Model-2**	**Model-2/Model-1**
2nd Lesner end	382.4	377.2	0.986	377.2	1
1st Aden end	259.2	260.6	1.005	261.7	0.996

From Table 19, in *Model-1* for the Lesner girder, the original cross-sectional area of the strands was used to validate the model since the damage was insignificant. Therefore, *Model-1* and *Model-2* for the Lesner girder were identical suggesting no loss in the load-carrying capacity due to corrosion. In the Aden girder, the behavior of the physical girder was captured in *Model-1* by excluding two strands in the bottommost layer of strands resulting in a maximum load of 260.9 kips, which is less than 0.60% of the experimental maximum load. *Model-2* for the Aden girder attained a maximum load of 261.7 kips, which is only 0.43% higher than the maximum load obtained from *Model-1*. Therefore, at this level of corrosion damage in both girders, the finite elements analyses do not suggest considerable degradation in the shear strength due to corrosion of strands.

CHAPTER – 6 CONCLUSION AND FUTURE WORK

Conclusions

Many factors affect the shear strength of prestressed concrete girders. This includes the concrete compressive strength, stirrup spacing, beam depth, longitudinal and transverse reinforcement ratios, shear span-to-depth ratio, and the effective prestress. Thus, the following conclusions may apply only for the spectrum of corroded prestressed concrete girders with similar conditions to the ones studied in this research. These conclusions were drawn from the non-destructive tests, the destructive shear tests, post-testing investigation, and the data analysis performed in this research.

- Post-testing investigation of strands near the failure locations showed a strong correlation with the exterior deterioration of girders and the half-cell potential results. Generally, corrosion in strands is indicated by longitudinal cracking or concrete cover spalling and more negative potential difference.
- Although expensive, the DIC provided a great tool to inspect deformations in the girder during the test.
- An I-beam girder end with minor corrosion damage, light pitting on some strands, failed in flexure by concrete crushing at the top of the girder. This indicates that failure was not dominated by the corrosion in the strands. On the other hand, a girder end of an adjacent box prestressed concrete beam with severe condition, heavy pitting with complete loss of some strand wires, failed in flexure by strands rupturing with a considerable loss of the flexural capacity, 35% loss of its original load-carrying capacity. This suggests that using the strain compatibility approach, as described in Section 5.3, by prescribing a value of crushing strain in concrete at the extreme compression fiber may not be appropriate for girders with severe condition. This is due to the fact that the strands may rupture prematurely before the concrete crushes.
- When calculating the initial stiffness of a corroded prestressed concrete girder, it may be desired to ignore the contribution of the concrete cover completely due to

the corrosion-induced cracks and spalls. This can be seen in the Load-Displacement plots in Figure 63 and Figure 64.

- Recommendations proposed by Naito et al. (2011) predicted the flexural strength of the box beam with a tested-to-calculated strength ratio of 1.06. However, this ratio was higher, more conservative estimate, when the Naito's recommendations were used for the I-beam. Modifications to the Naito's recommendations proposed by Alfailakawi et al. (2020) were found to give a close, yet conservative, estimate of the flexural strength of the I-beam with a tested-to-calculated strength ratio of 1.04.
- The effective prestress calculated with the refined AASHTO method slightly differs from the effective prestress calculated based on the first observed flexural crack. While this may have an influence on the accuracy of predicting the cracking load, at serviceability level, it does not seem to significantly influence the accuracy of predicting the flexural and shear strengths, at ultimate level.
- Corrosion in strands seems to not have as much influence on the shear capacity as on the flexural capacity. This was observed in the Aden girder tests. The less damaged end failed in shear at a load of 259 kips while the comparatively more damaged end failed prematurely in flexure at a load of 230.5 kips without strong signs of an imminent shear failure at that level. This observation was also supported by FE analyses performed on both girders by Aliasghar-Mamaghani (in press) and discussed in Section 5.5. However, existing corrosion damage, such as concrete spalls, can deviate the path of the inclined shear cracks as observed in the second Lesner test.
- Reaching the ultimate shear capacity in a shear test with a shear span-to-depth ratio of more than 2.0 can be challenging in girders with corrosion damage at the bottom. In two girder ends tested in this research, flexural failure occurred prematurely. Therefore, to obtain a true shear failure, a short shear span, *a/d* less than 2.0, may be required. However, this short shear span can result in a diagonal crushing caused by the high compressive stresses transferred through the web.
- All girders exceeded their predicted shear capacities with the ACI and the AASHTO codes. The AASHTO Appendix B5.2 was the most conservative

method with an average tested-to-calculated shear strength ratio of 1.44 for girder ends failed in shear, while the ACI V_{ci}-V_{cw} and the AASHTO A5.8.3.4.2 resulted in similar but less conservative shear capacities with average tested-to-calculated shear strength ratios of 1.36 and 1.33, respectively, for girder ends failed in shear. The Response 2000 was also a good tool to predict the shear strength with an average tested-to-calculated shear strength ratio of 1.30. The high level of conservatism is thought to be a consequence of the small shear span-to-depth ratio used in the shear tests. Girders with small shear span-to-depth ratios resist the load mainly by the arching action. Consequently, the STM was found to be the most accurate tool to predict the shear capacity of girders with loads applied near the end regions. The STM resulted in an average tested-to-calculated strength ratio of 1.073 for girder ends failed in shear.

Recommendations for Future Work

The following recommendations are reached based on the previous conclusions and the limitations of this research. They are meant to improve the future research concerning estimating, or retrofitting, the shear strength of corrosion-damaged prestressed concrete girders.

- The girders selected in this research contained no visible deterioration on their webs. To better understand the effect of the corrosion on the shear strength, more tests should be conducted on girders containing visible damage near the webs and/or exposed stirrups. In this case, not only the concrete contribution to the strength is expected to be compromised, but stirrups would also be expected to be corroded affecting the steel contribution to the shear strength.
- If girders with damaged web are not available, imposing artificial damage on the girder webs would be suggested. A similar technique was followed in research by Shafei et al. (2020).
- To avoid premature flexural failure, a shear test can be performed on a strengthened girder in flexure. Flexural strengthening can be in the form of Carbon-Fiber Reinforced Polymer, CFRP, laminates or any other repair

techniques that enhance the flexural strength only. In this case, higher shear span-to-depth ratios would be possible.

- More research is required on how corrosion influences the effective prestress in the strands. Most of the available recommendations for corroded girders are intended to be used to determine the residual strength and not the cracking strength. This issue was discussed in Section 5.4. In addition, more research should be done to study how girders fail by rupture of strand wires. One way this can be achieved is by performing tension tests on strands having different levels of corrosion and monitoring the ultimate strain at which the wires rupture as suggested by Neeli (2020).

REFERENCES

Aguilar, G.; Matamoros, A. B.; Parra-Montesinos, G. J.; Ramirez, J. A.; and Wight, J. K. (2002). Experimental 23 Evaluation of Design Procedures for Shear Strength of Deep Reinforced Concrete Beams. *ACI Structural Journal*, 24 V. 99, No. 4, July-Aug., pp. 539-548.

Alfailakawi, A. (2020). *Experimental and Analytical Evaluation of Residual Capacity and Repair Methods for Corrosion-Damaged Prestressed Concrete Bridge Girders*. (No. FHWA/VTRC 21-R6).

Aliasghar-Mamaghani, M. (in press). *Analytical Study of Corrosion Effect on the Load-Carrying Capacity of Prestressed Concrete Bridge Girders.*

ASTM C39 / C39M-10, Standard Test Method for Compressive Strength of Cylindrical Concrete Specimens, ASTM International, West Conshohocken, PA, 2010, www.astm.org

Barker, R. M., & Puckett, J. A. (2013). *Design of highway bridges: An LRFD approach*. John wiley & sons.

Bentz, E. C. (2000). Sectional analysis of reinforced concrete members (p. 310). Toronto: University of Toronto.

Bentz, E. C., and Collins, M. P., "Response 2000." http://www.ecf.utoronto.ca/~bentz/r2k.htm (2000).

Bentz, E. C., F. J. Vecchio and M. P. Collins (2005). Simplified Modified Compression Field Theory for Calculating Shear Strength of Reinforced Concrete Elements. *ACI Structural Journal*, Vol. 103, No. 4, 2005, pp. 614-624.

Cairns J, Plizzari GA, Du Y, Law DW and Franzoni C (2005). Mechanical properties of corrosion-damaged reinforcement. *ACI Materials Journal* 102(4): 256–264.

Carino, N. J. and H. S. Lew. Re-examination of the Relation between Splitting Tensile and Compressive Strength of Normal Weight Concrete. *ACI Journal, Proceedings*, Vol. 79, No. 3, 1982, pp. 214-219.

Chase, S. B., & Balakumaran, S. S. (2020). Magnetic Flux Leakage Device for Evaluation of Prestressed Concrete Box Bridges (No. VTRC 20-R14). *Virginia Transportation Research Council*.

Collins, M. P., & Mitchell, D. (1991). Prestressed concrete structures (Vol. 9). Englewood Cliffs, NJ: Prentice Hall.

Collins, M. P., & Mitchell, D. (1997). *Prestressed Concrete Structures*. Response Publications. Canada.

Collins, M. P., D. Mitchell, P. Adebar and F. J. Vecchio (1996). A General Shear Design Method. *ACI Structural Journal*, Vol. 93, No. 1, 1996, pp. 36-45.

Coronelli, D., and Gambarova (2004). Structural Assessment of Corroded Reinforced Concrete Beams: Modeling Guidelines. *Journal of Structural Engineering, ASCE,* Vol. 130, No. 8, December, pp. 1214-1224.

El-Sayed, A. K. (2014). Strut and tie modeling for RC short beams with corroded stirrups. *Latin American Journal of Solids and Structures*, 11(12), 2255-2270.

Elzanaty, A. H., A. H. Nilson and F. O. (1986). Slate. Shear Capacity of Reinforced Concrete Beams Using High-Strength Concrete. *Journal of the American Concrete Institute*, Vol. 83, No. 2, 1986, pp. 290-296.

Fereig S.M. and Smith K.N. (1977). Indirect Loading on Beams with Short Shear Spans. *American Concrete Institute (ACI), Journal Proceedings*, Vol.74, No. 5, pp.220-222.

FIB, Structural Concrete, Textbook on Behaviour, Design, and Performance, Volume 3, International Federation for Structural Concrete, Lausanne, Switzerland, 1999, 269 pp.

Hawkins, N. M. and D. A. Kuchma (2007). NCHRP Report 579: Application of LRFD Bridge Design Specifications to High-Strength Structural Concrete: Shear Provisions. *Transportation Research Board of the National Academies*, Washington, D.C., 2007.

Hawkins, N. M., D. A. Kuchma, R. F. Mast, M. L. Marsh and K.-H. Reineck (2005). NCHRP Report 549: Simplified Shear Design of Structural Concrete Members. *Transportation Research Board of the National Academies*, Washington, D.C., 2005.

Higgins, C., Farrow, W.C., Potisuk, T., Miller, T.H., Yim, S.C., Holocomb, G.R., Cramer, S.D., Covino, B.S., and Bullard, S.J. (2003). Shear Capacity Assessment of Corrosion Damaged Reinforced Concrete Beams. *Oregon Department of Transportation*.

Kassner, B. (2012). *Shear Strength of Full-Scale Prestressed Lightweight Concrete Girders with Composite Decks*. Virginia Polytechnic Institute and State University.

Kuchma, D., Yindeesuk, S., Nagle, T., Hart, J., & Lee, H. H. (2008). Experimental validation of strut-and-tie method for complex regions. *ACI Structural Journal*, 105(5), 578.

Laughery, L., and Pujol, S. (2015). Compressive Strength of Unreinforced Struts. *ACI Structural Journal*, V. 112, 4 No. 5, Sept.-Oct., pp. 617-624. doi: 10.14359/51687711

Loflin, B. (2008). *Bond and Material Properties of Grade 270 and Grade 300 Prestressing Strands*. Virginia Polytechnic Institute and State University.

MacGregor, J. G., Sozen, M. A., & Siess, C. P. (1960). Strength and behavior of prestressed concrete beams with web reinforcement. University of Illinois Engineering Experiment Station. College of Engineering. University of Illinois at Urbana-Champaign.

MacGregor, J. G., Sozen, M. A., & Sless, C. P. (1965). Strength of prestressed concrete beams with web reinforcement. *In Journal Proceedings* (Vol. 62, No. 12, pp. 1503-1520).

Maxwell, B. S., and Breen, J. E. (2000). Experimental Evaluation of Strut-and-Tie Model Applied to Deep Beam with 27 Opening. *ACI Structural Journal*, V. 97, No. 1, Jan.-Feb., pp. 142-148

Mörsch, E. Concrete-Steel Construction. McGraw-Hill Book Co., New York, 1909, (English translation of 3rd ed. of Der Eisenbetonbau, 1st ed., 1902).

Naaman, A. E. (2012). *Prestressed concrete analysis and design: Fundamentals*. Techno Press 3000.

Naito, C., Jones, L., & Hodgson, I. (2010). Inspection methods & techniques to determine non visible corrosion of prestressing strands in concrete bridge components: task 3, forensic evaluation and rating methodology (No. ATLSS report no. 09-10). *Pennsylvania. Dept. of Transportation. Bureau of Planning and Research*.

Naito, C., Jones, L., & Hodgson, I. (2011). Development of flexural strength rating procedures for adjacent prestressed concrete box girder bridges. *Journal of Bridge Engineering*, 16(5), 662–670. https://doi.org/10.1061/(ASCE)BE.19435592.0000186

Neeli, Y. (2020). *Use of Photogrammetry Aided Damage Detection for Residual Strength Estimation of Corrosion Damaged Prestressed Concrete Bridge Girders*. Virginia Polytechnic Institute and State University.

Osborn, G. P., Barr, P. J., Petty, D. A., Halling, M. W., & Brackus, T. R. (2012). Residual prestress forces and shear capacity of salvaged prestressed concrete bridge girders. *Journal of Bridge Engineering*, 17(2), 302-309.

Pape, T. M., & Melchers, R. E. (2013). Performance of 45-year-old corroded prestressed concrete beams. *Proceedings of the Institution of Civil Engineers-Structures and Buildings*, 166(10), 547-559.

Pei, J. S., Martin, R. D., Sandburg, C. G., & Kang, T. K. (2008). Rating Precast Prestressed Concrete Bridges for Shear (FHWA-OK-08-08 2186).

Reineck, K. H. (Ed.). (2002). Examples for the design of structural concrete with strut and-tie models (No. 208). *American Concrete Institute.*

Ritter, W. Die Bauweise Hennebique (The Hennebique System of Construction). *Schweizerische Bauzeitung*, Vol. No. 1899, pp. 59-61.

Rogowsky, D.M. and MacGregor, J.G. (1986). Design of Deep Reinforced Concrete Continuous Beams. *Concrete International: Design and Construction*, Vol. 8 (1986), No. 8, August, pp 49-58

Runzell, B., Shield, C., & French, C. (2007). Shear capacity of prestressed concrete beams.

Schlaich, J.; Schäfer, K.; and Jennewein, M. (1987). Toward a Consistent Design of Structural Concrete. *PCI Journal*, V. 32, No. 3, May-June, pp. 74-150

Shafei, B., Phares, B., & Shi, W. (2020). Beam End Repair for Prestressed Concrete Beams (No. IHRB Project TR-715).

Shield, C., & Bergson, P. (2018). BR27568–Experimental Shear Capacity Comparison Between Repaired and Unrepaired Girder Ends.

Sozen, M. A., Zwoyer, E. M., & Siess, C. P. (1959). Investigation of prestressed concrete for highway bridges: Part I strength in shear of beams without web reinforcement. University of Illinois at Urbana Champaign, College of Engineering. Engineering Experiment Station.

Suffern, C., El-Sayed, A. K., and Soudki, K. (2010). Shear Strength of Disturbed Regions with Corroded Stirrups in Reinforced Concrete Beams. *Canadian Journal of Civil Engineering*, Vol 37., No. 8, pp. 1045-1056.

Vecchio, F. J. and M. P. Collins (1986). The Modified Compression-Field Theory for Reinforced Concrete Elements Subjected to Shear. *ACI Journal*, Proceedings, Vol. 83, No. 2, 1986, pp. 219-231.

Walraven, J. C. (1981). Fundamental Analysis of Aggregate Interlock. *Journal of the Structural Division*, Vol. 107, No. 11, 1981, pp.

Wight, J. K., and Parra-Montesinos, G. (2003). Use of Strut-and-Tie Model for Deep Beam Design as per ACI 318 1 Code. *Concrete International*, V. 25, No. 5, May, pp. 63-70.

Williams, C.; Deschenes, D.; and Bayrak, O. (2011). Strut and Tie Model Examples for Bridges: Final Report. Report 3 No 5-5253-01-1, *Center for Transportation Research, University of Texas at Austin*, Austin, TX, Oct.

APPENDICES

APPENDIX-A: Plans and Drawings

APPENDIX-B: Analysis

APPENDIX-C: Calculations

APPENDIX-A: Plans and Drawings

A.1 Plans for Bridge Girders

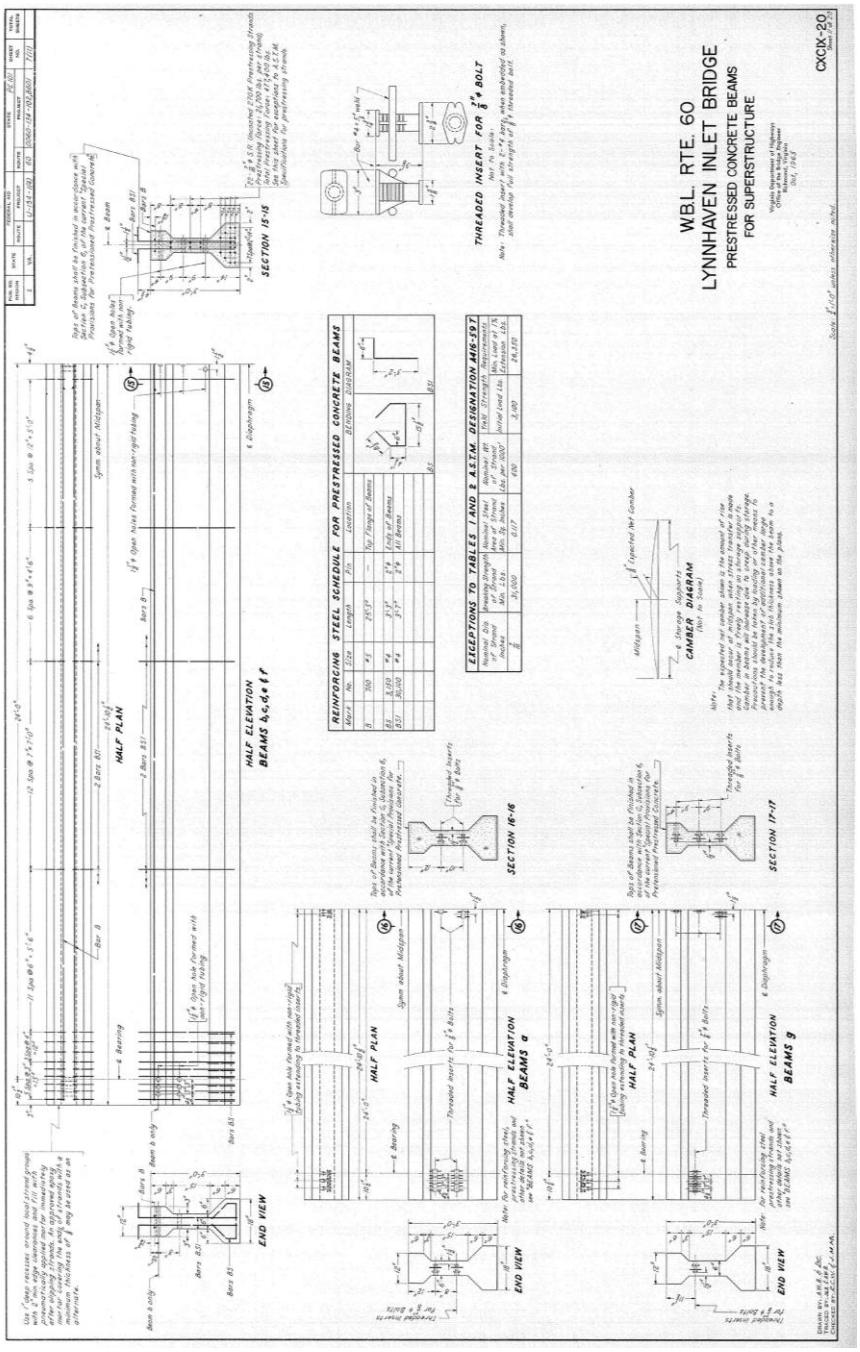

Figure 80 Plans for the Lesner girder

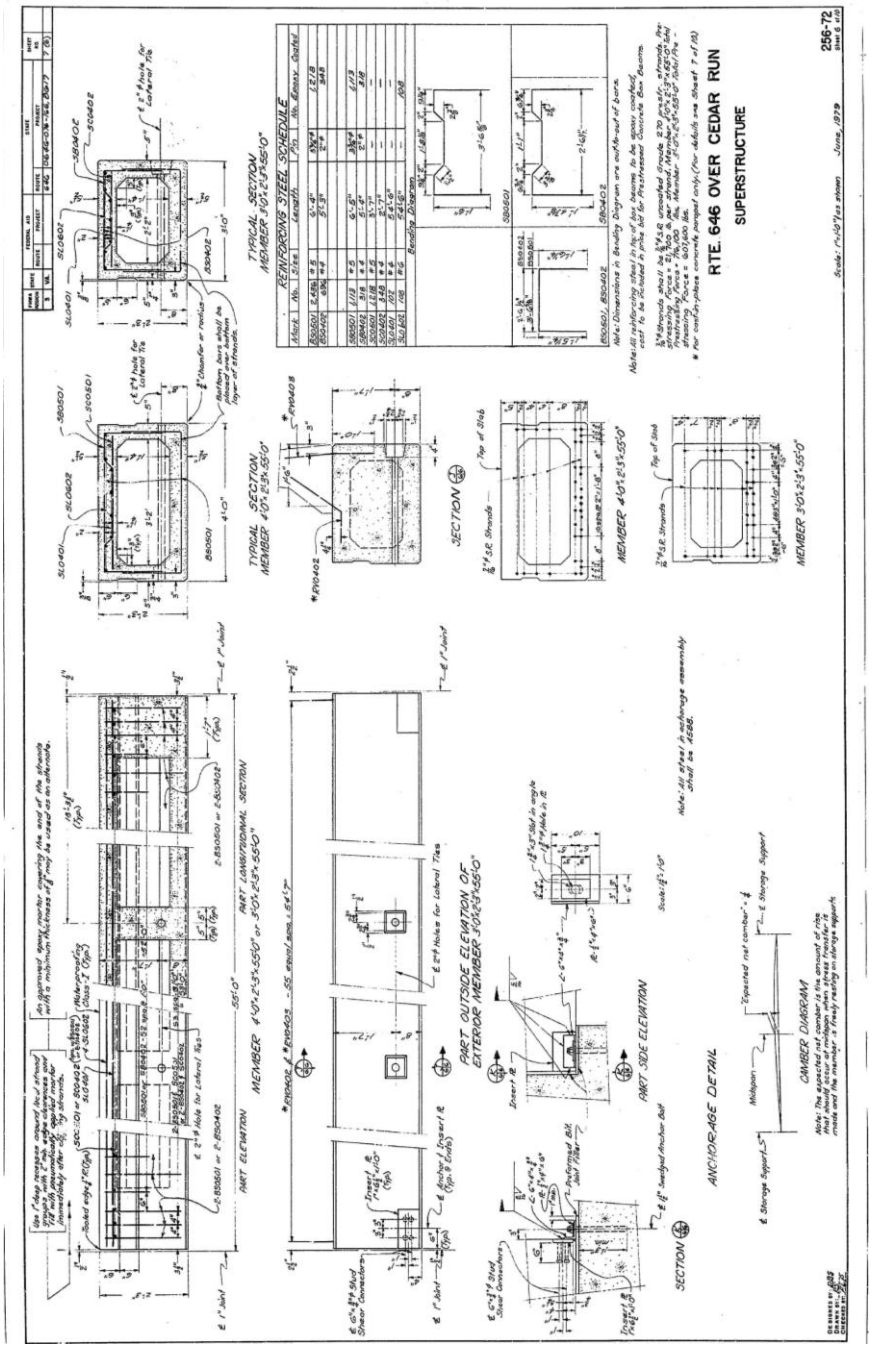

Figure 81 Plans for the Aden girder

A.2 Damage Maps for Girders

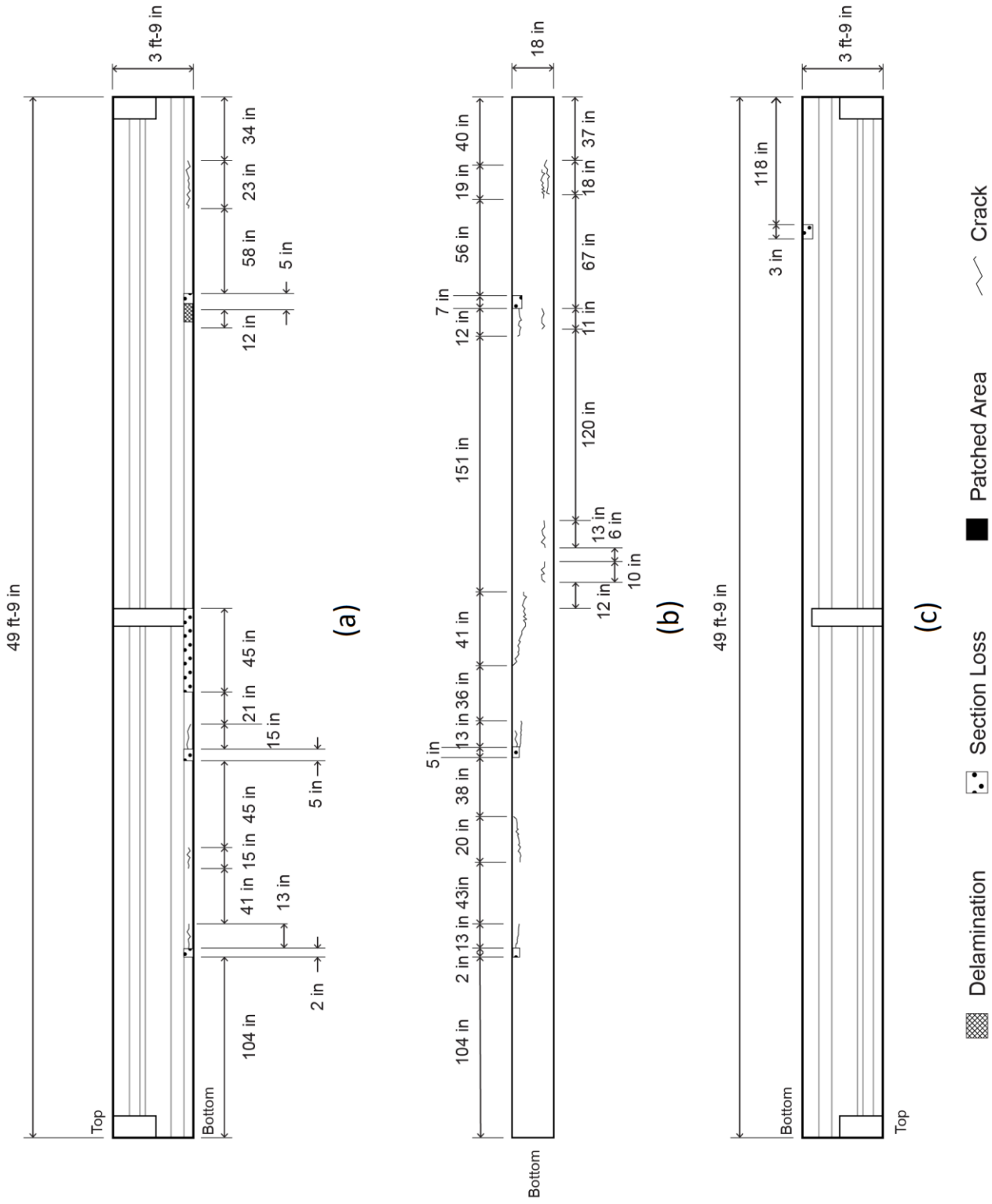

Figure 82 Damage map for the Lesner girder.

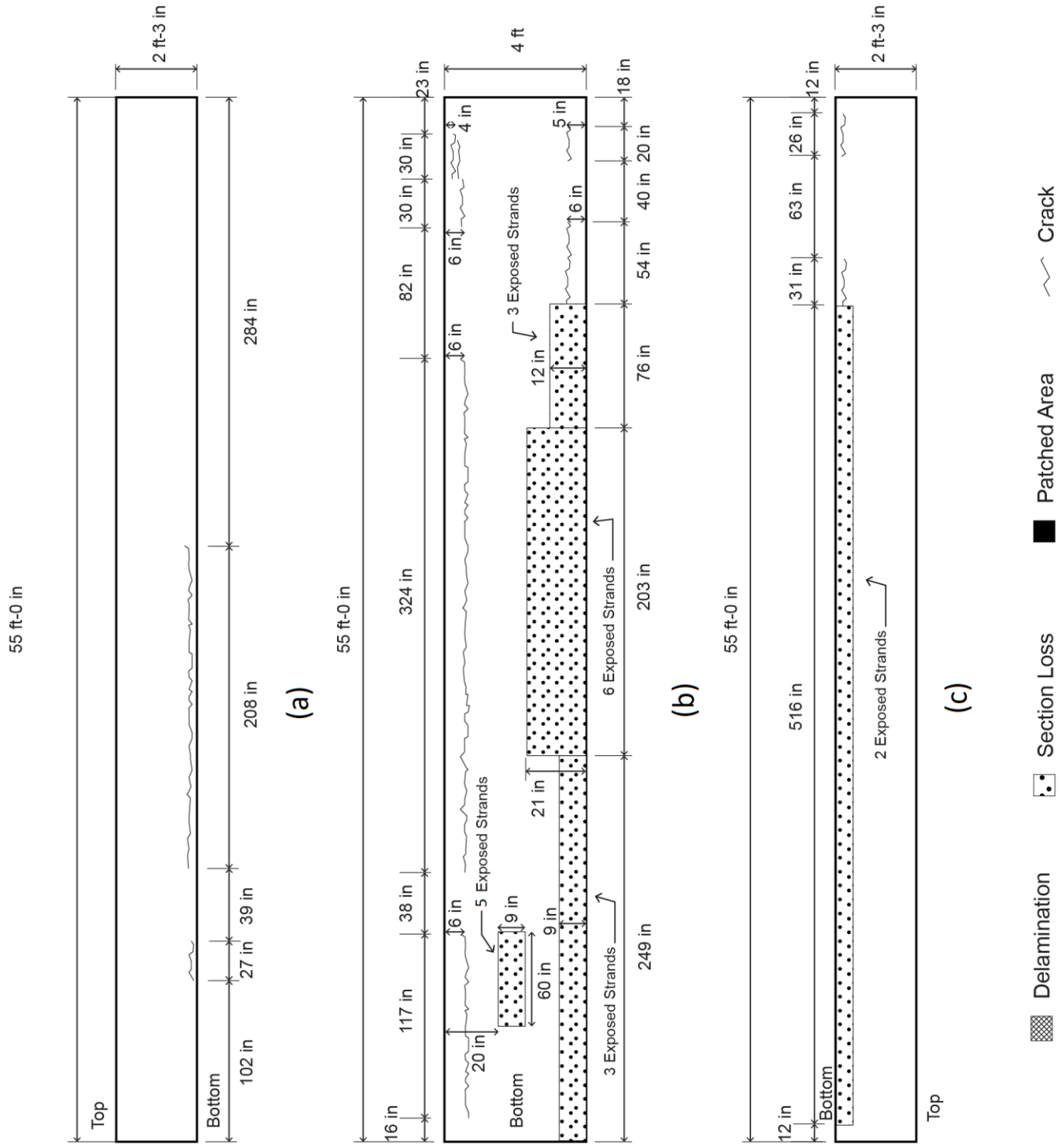

Figure 83 Damage map for the Aden girder.

APPENDIX-B: Analysis

B.1 Experimental Data

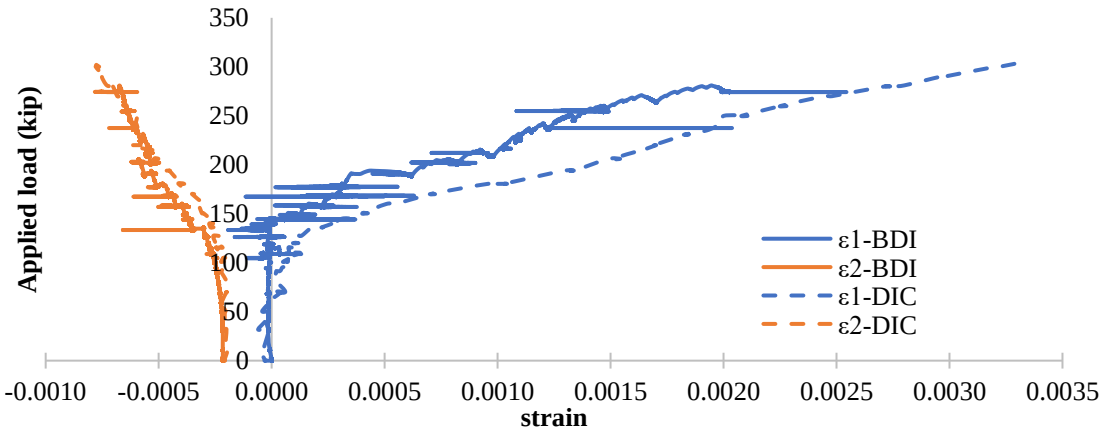

Figure 84 Principle strains for the second Lesner test.

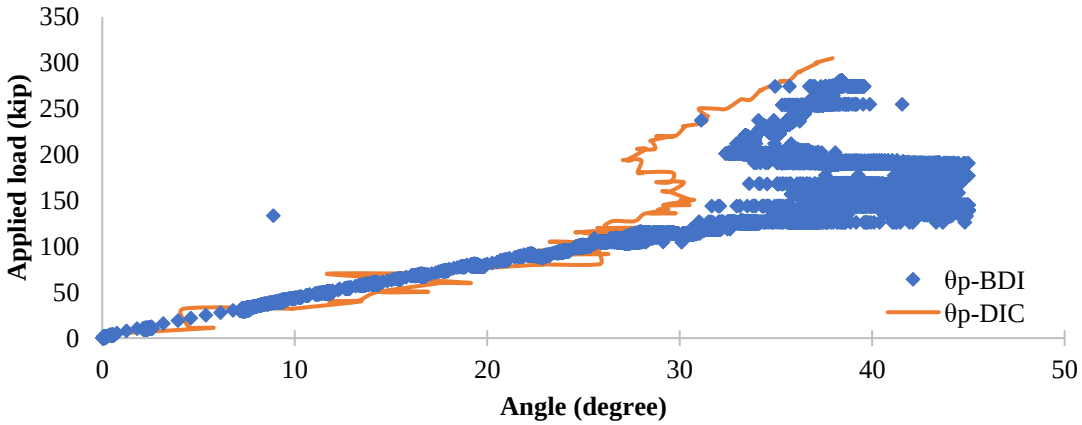

Figure 85 Principle angle for the second Lesner test.

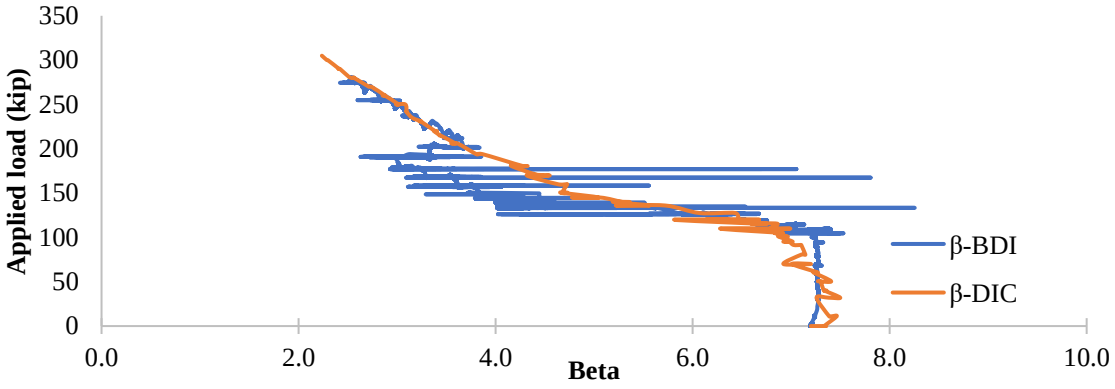

Figure 86 Beta factor for the second Lesner test.

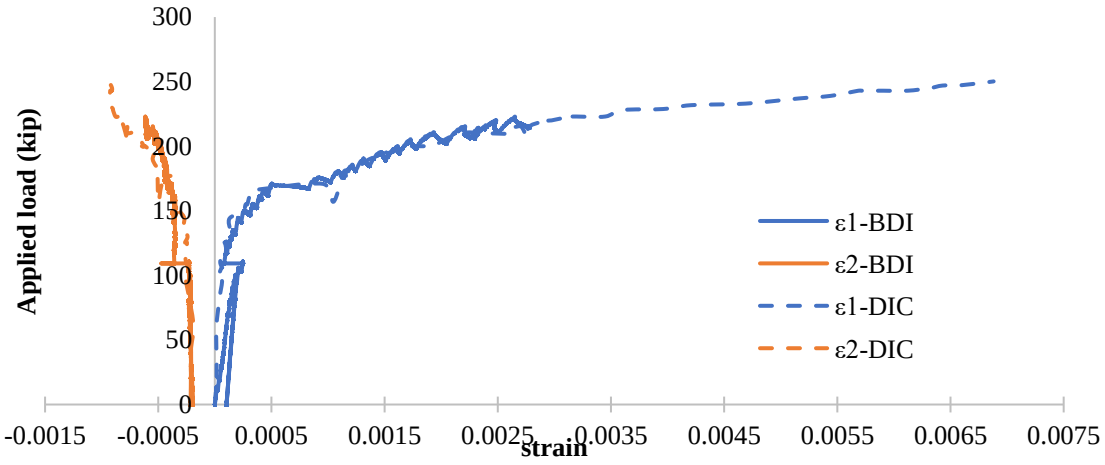

Figure 87 Principle strains for the first Aden test.

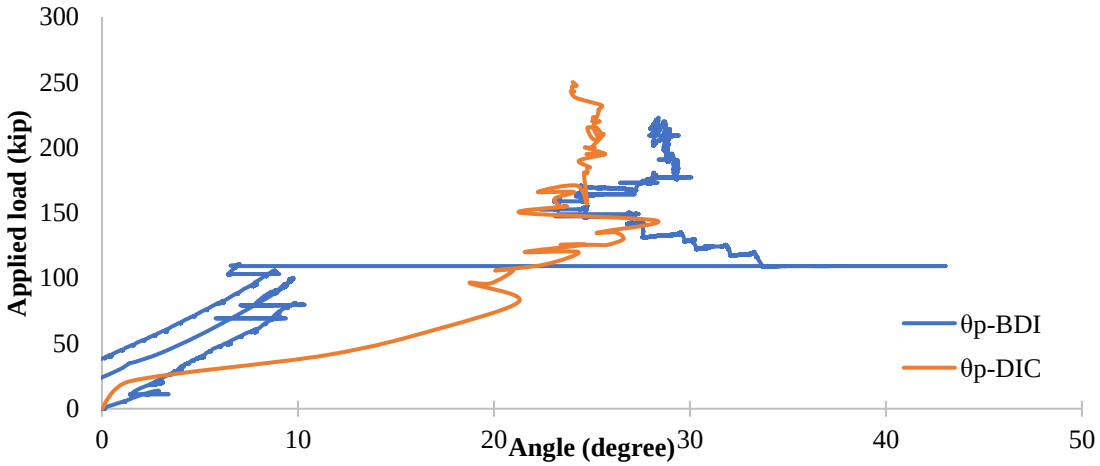

Figure 88 Principle angle for the first Aden test.

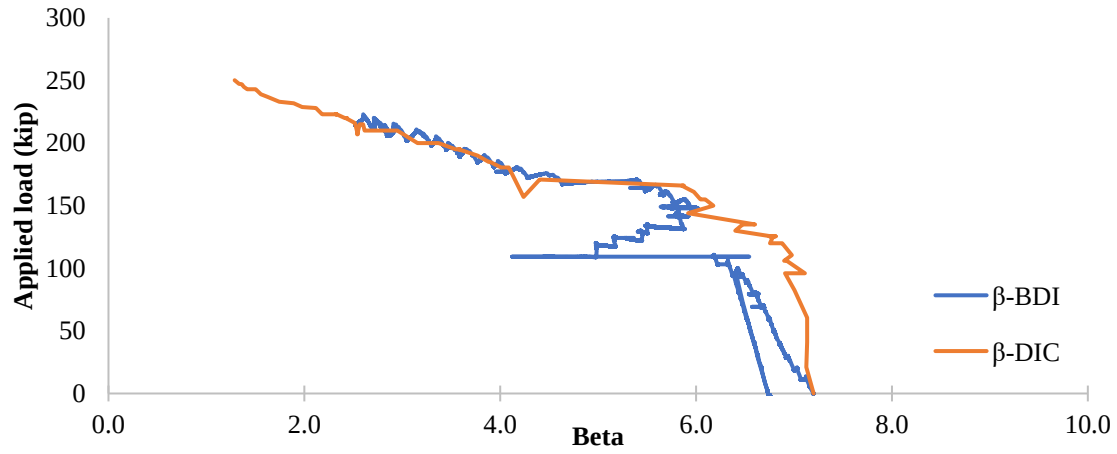

Figure 89 Beta factor for the first Aden test.

B.2 STMs

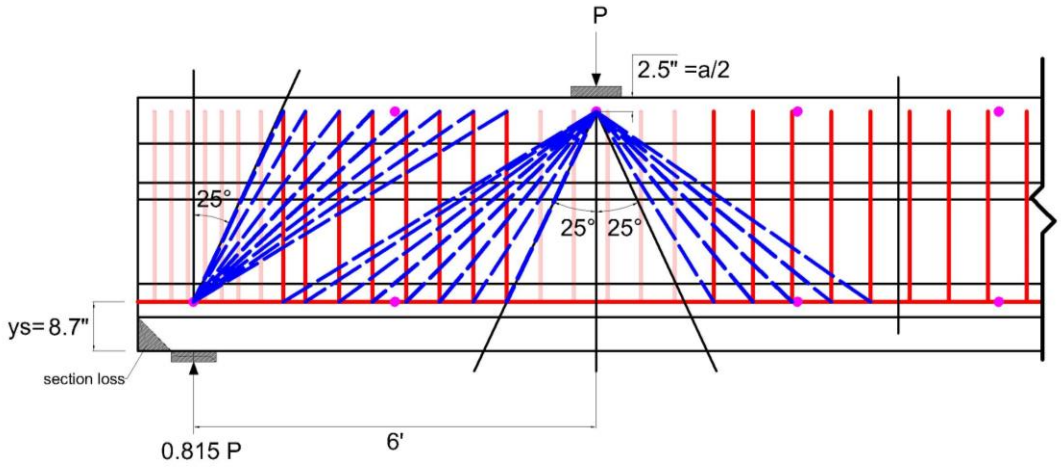

Figure 90 Stirrups comprising the vertical ties for the second Lesner end.

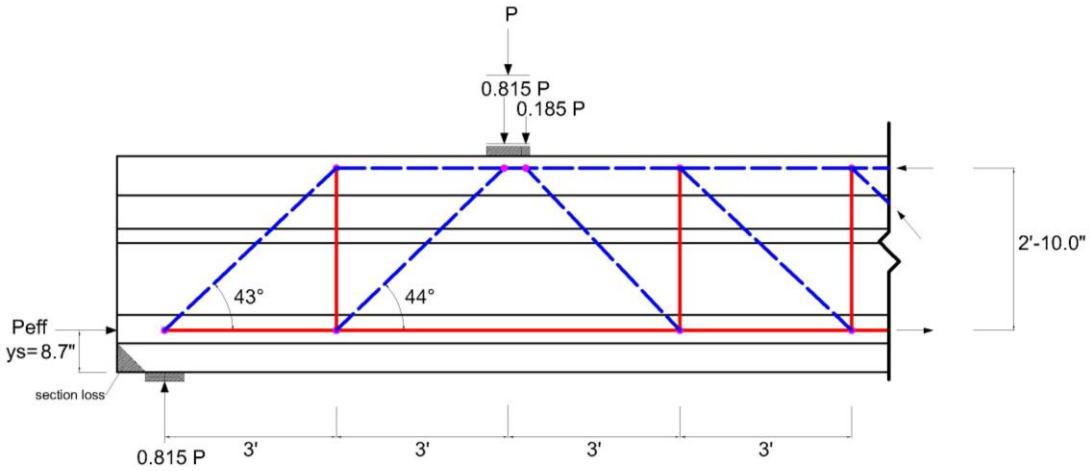

Figure 91 Truss-1 for the second Lesner end.

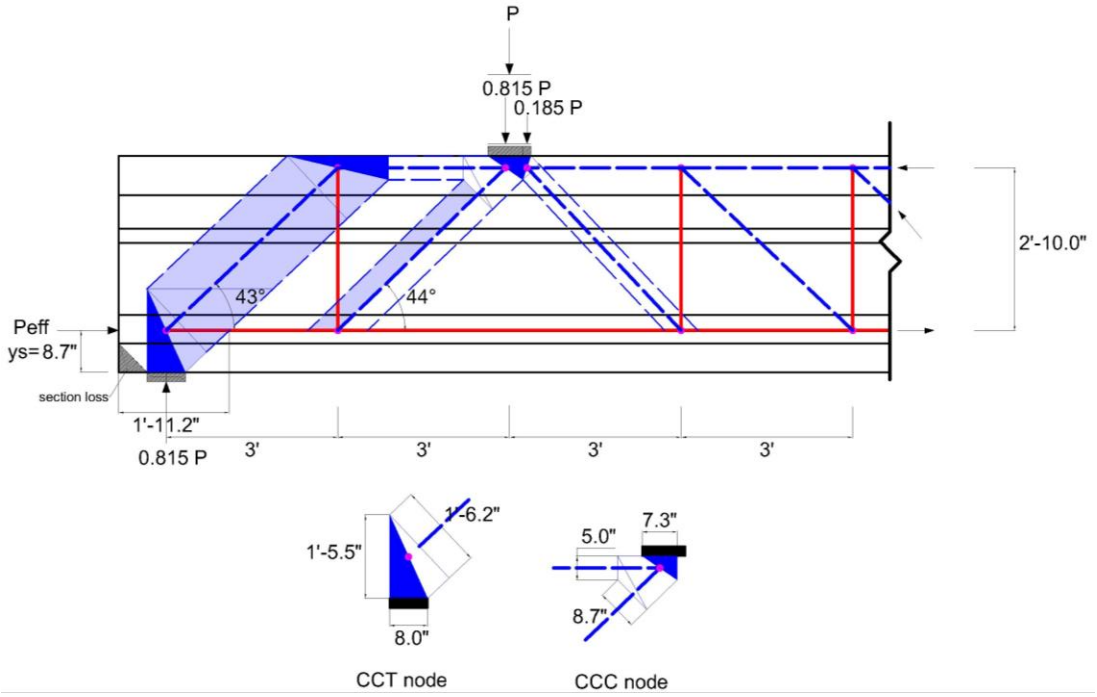

Figure 92 Truss-1 geometries for the second Lesner end.

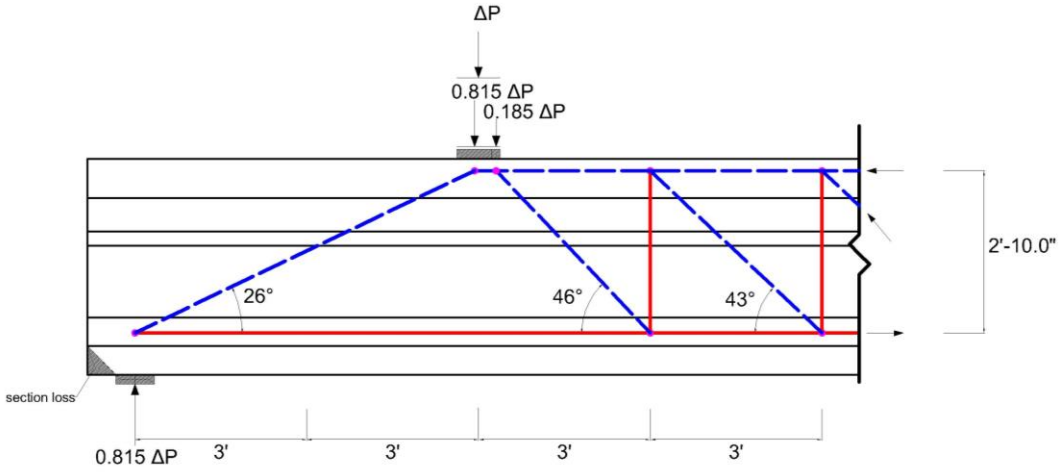

Figure 93 Truss-2 for the second Lesner end.

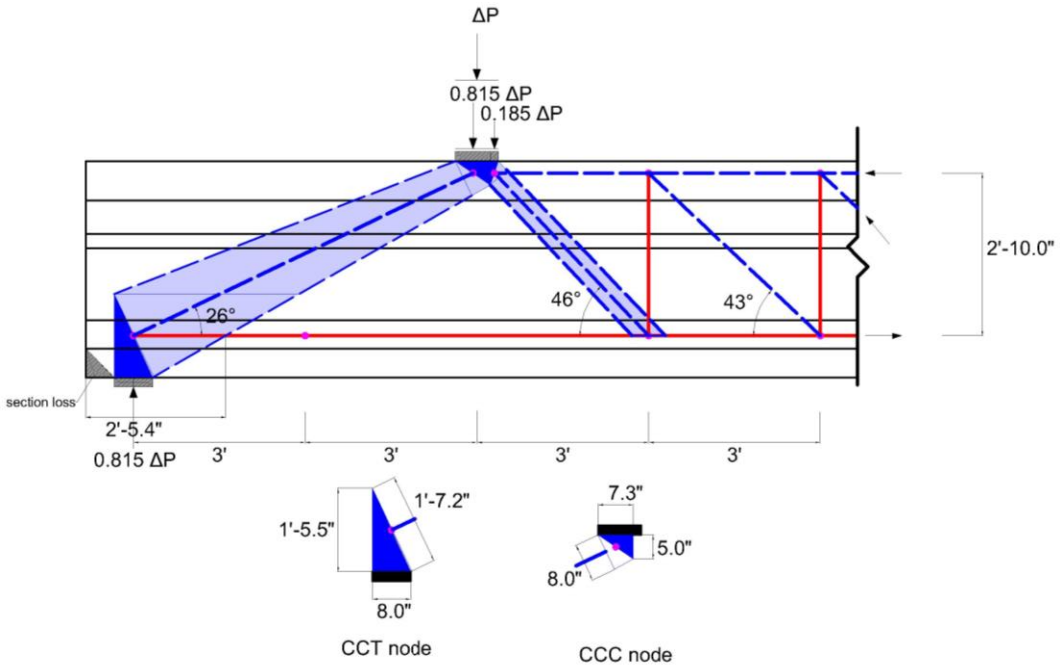

Figure 94 Truss-2 geometries for the second Lesner end.

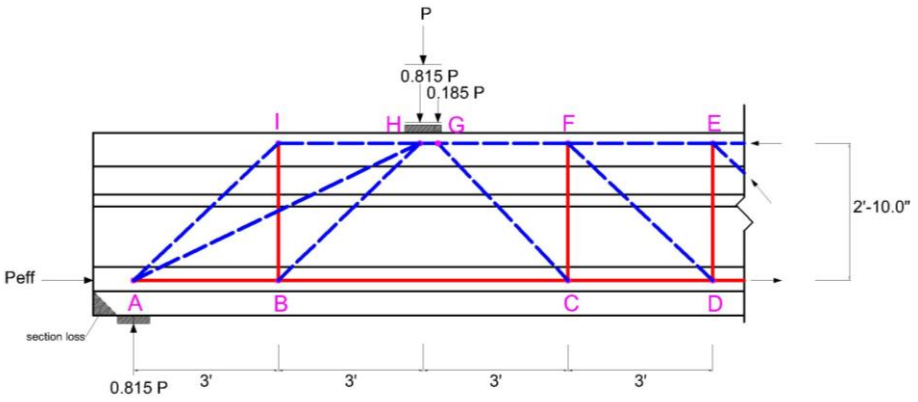

Figure 95 Truss-1 and Truss-2 overlaid for the second Lesner end.

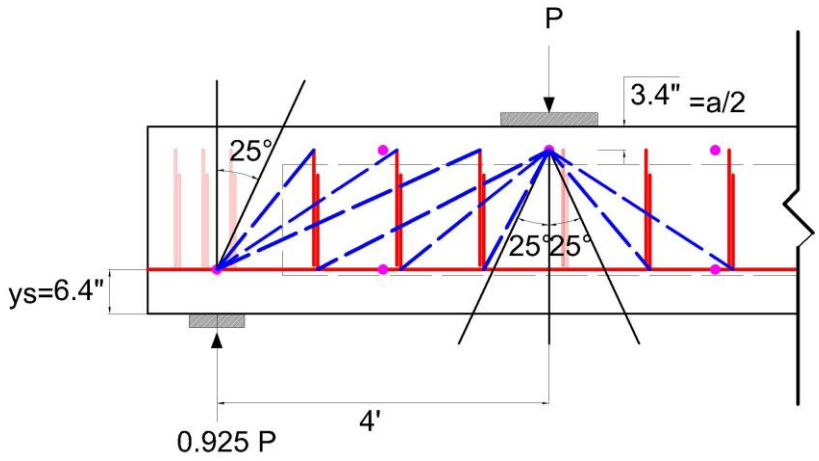

Figure 96 Stirrups comprising the vertical ties for the first Aden end.

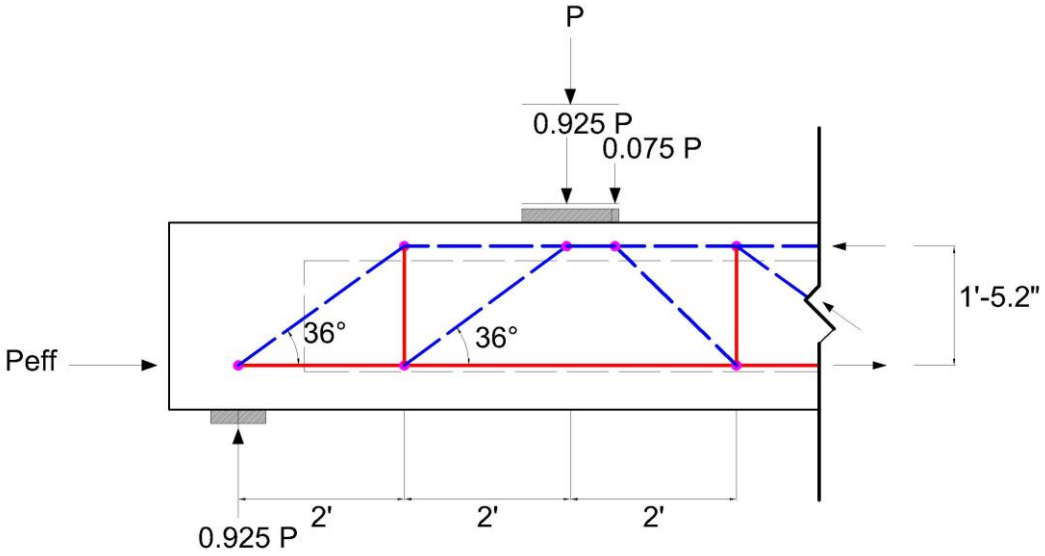

Figure 97 Truss-1 for the first Aden end.

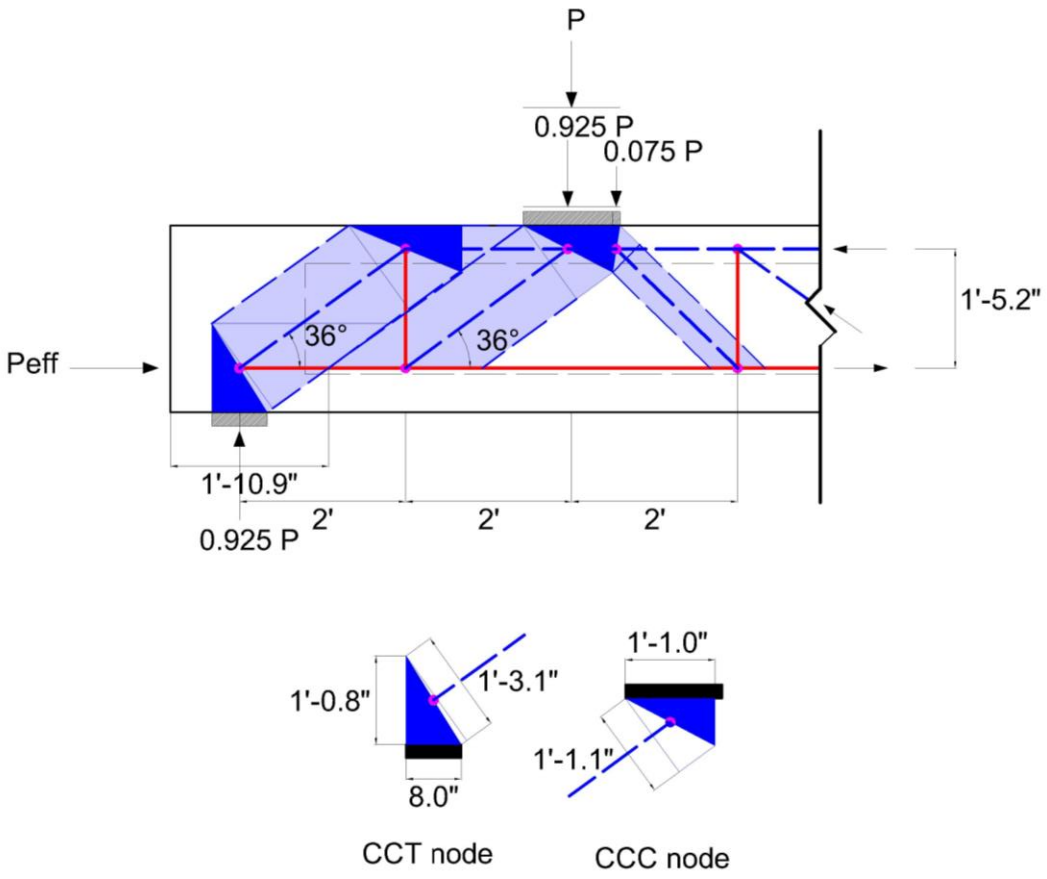

Figure 98 Truss-1 geometries for the first Aden end.

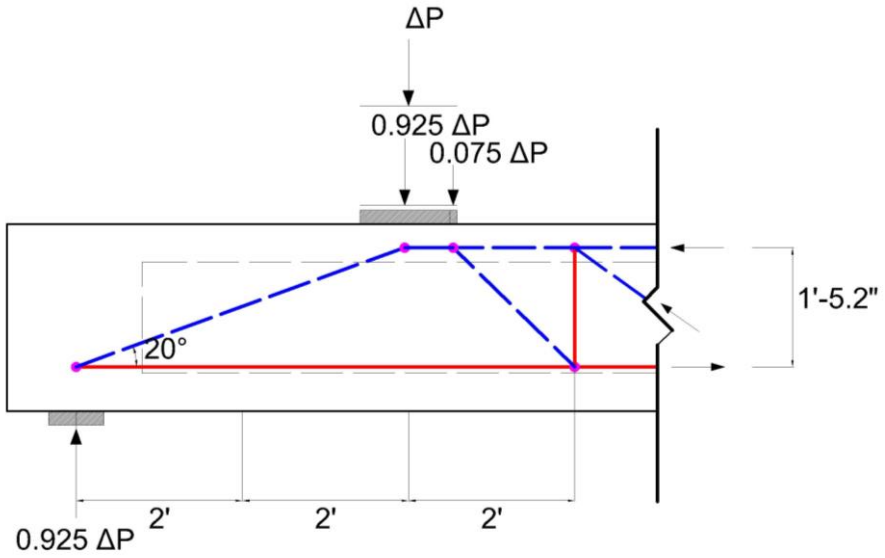

Figure 99 Truss-2 for the first Aden end.

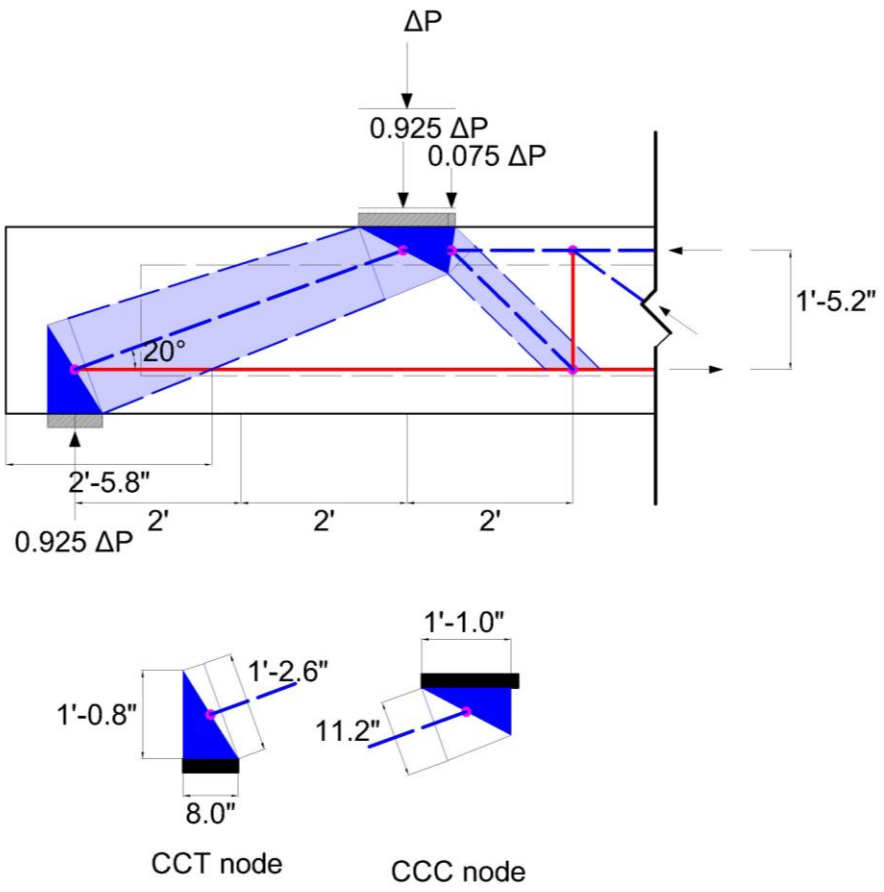

Figure 100 Truss-2 geometries for the first Aden end.

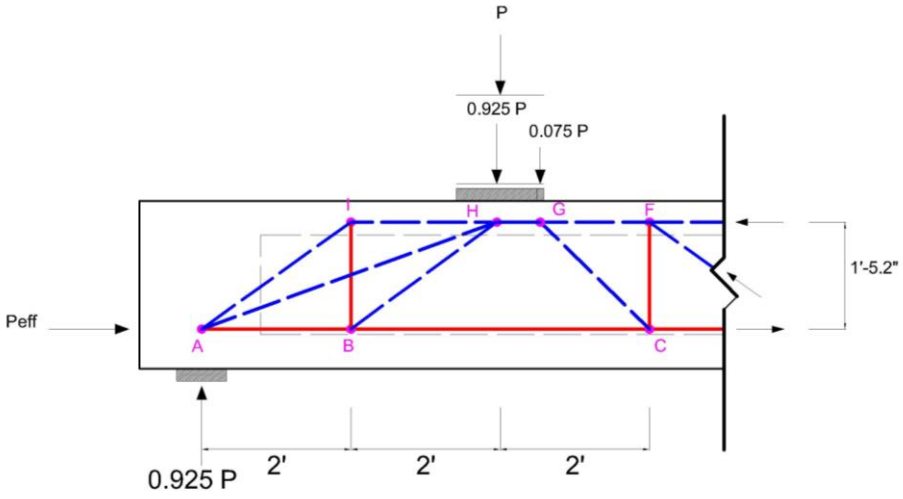

Figure 101 Truss-1 and Truss-2 overlaid for the first Aden end.

APPENDIX-C: Calculations

INPUT FOR THE LESNER GIRDER:

Materials:

Concrete:

Unit weight $\gamma := 150\frac{lbf}{ft^3}$ $\lambda := 1$ "for normal-weight concrete"

Compressive strength for the beam at release $f'_{ci} := 4000psi$

Compressive strength for the beam at service $f'_{c} := 4957psi$

Compressive strength for the slab at service $f'_{cdeck} := 4090psi$

Tendon:

Stress-Relieved 7-wire strands

$f_{pu} := 270ksi$ $E_{ps} := 28000ksi$

$f_{pj} := 195.8ksi$ jacking stress (From Prestress Losses)

$f_{piPLAN} := 185ksi$ (This number is from plans)

Stress at release (initial stress):

$f_{pi} := 185ksi$ from prestress losses

Stress at service (effective stress):

$f_{se} := 149.7ksi$ from prestress losses

Stress-strain relationship for strands

$$f_s(\varepsilon_s) := \begin{cases} (E_{ps}\cdot\varepsilon_s) & \text{if } 0 \le \varepsilon_s \le 0.006535714286 \\ \left[183ksi + \left(\frac{229.5ksi - 183ksi}{0.01 - 0.006535714286}\right)\cdot(\varepsilon_s - 0.006535714286)\right] & \text{if } 0.006535714286 \le \varepsilon_s \le 0.01 \\ \left[229.5ksi + \left(\frac{250ksi - 229.5ksi}{0.015 - 0.01}\right)\cdot(\varepsilon_s - 0.01)\right] & \text{if } 0.01 \le \varepsilon_s \le 0.015 \\ \left[250ksi + \left(\frac{f_{pu} - 250ksi}{0.06 - 0.015}\right)\cdot(\varepsilon_s - 0.015)\right] & \text{if } 0.015 \le \varepsilon_s \le 0.06 \end{cases}$$

Other model, Collins and Mitchel (1991)

$$f_{ss}(\varepsilon_s) := \min\left[\left[E_{ps}\cdot\varepsilon_s\cdot\left[0.03 + \frac{0.97}{\left[1 + (121\cdot\varepsilon_s)^6\right]^{0.167}}\right]\right], f_{pu}\right]$$

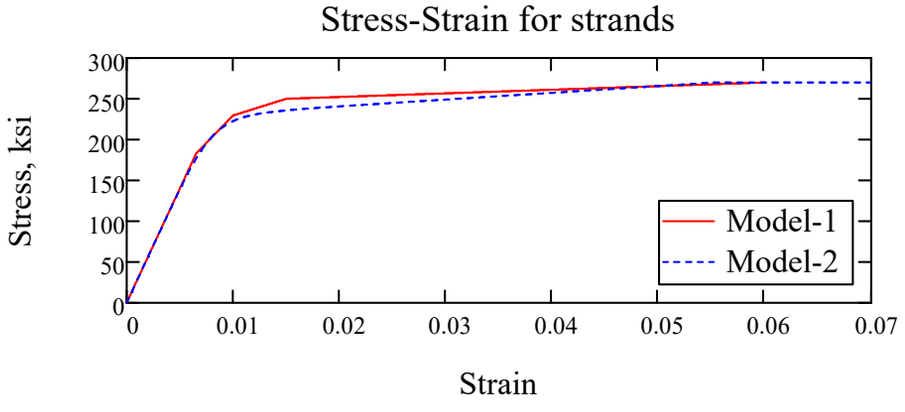

$f_{py} := f_s(0.01) = 229.5\cdot ksi$ Strand yield strength using 1% elongation

Mild reinforcement for beam:

Grade-60 bars $E_s := 29000ksi$

$f_y := 60ksi$

Stress-strain relationship

$f(\varepsilon_s) := \min(f_y, E_s \cdot \varepsilon_s)$

Mild reinforcement for slab:

Grade-40 bars

$f_{ydeck} := 40ksi$

Stress-strain relationship

$f_{deck}(\varepsilon_s) := \min(f_{ydeck}, E_s \cdot \varepsilon_s)$

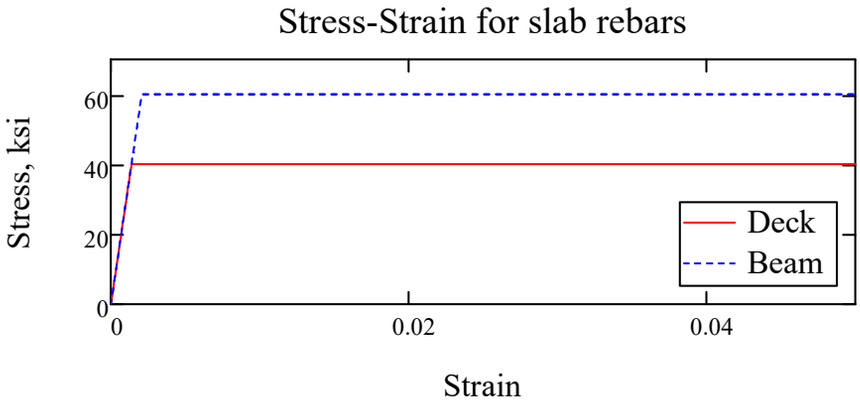

Dimensions:

Beam:

$Length := 49ft + 9in = 49.75\,ft$

$L_1 := 10in$ distance from the left end to the left support (second Lesner test)

$L_{1'} := 10in$ distance from the left end to the left support (first Lesner test)

$L_2 := 6ft$ distance from the left support to the point load (second Lesner test)

$L_{2'} := 8ft$ distance from the left support to the point load (first Lesner test)

$L_4 := 197in$ distance from the right support to the right end (second Lesner test)

$L_{4'} := 10in$ distance from the right support to the right end (first Lesner test)

Slab:

Width $b_{eff} := 38in$ Thickness $h_s := 7in$ Overlay $h_o := 1.25in$

Bolster:

Width $b_b := 12in$ Thickness $h_b := 1in$

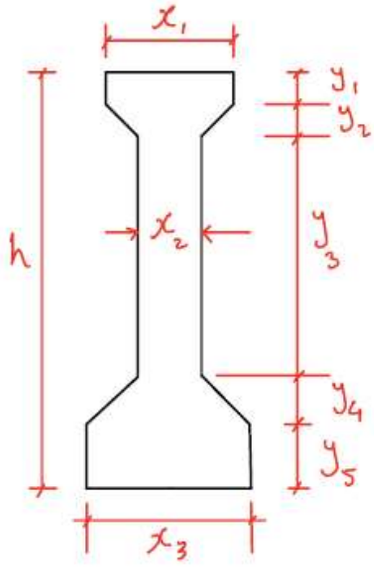

Bare Beam Section:

Hight $h := 36in$

$x_1 := 12in$ $x_2 := 6in$ $x_3 := 18in$

$y_1 := 6in$ $y_2 := 3in$ $y_3 := 15in$ $y_4 := 6in$ $y_5 := 6in$

Reinforcement:

Slab:

3#4 Grade-40 non-prestressed top bars in the longitudinal direction
2#4 Grade-40 non-prestressed bottom bars in the longitudinal direction as follows:

top $A_{s1deck} := 3 \cdot 0.20in^2$ $d'_{1deck} := h_o + 2.75in = 0.333\,ft$ distance from the top of the slab

bot $A_{s2deck} := 2 \cdot 0.20in^2$ $d'_{2deck} := h_o + 4.75in = 0.5\,ft$ distance from the top of the slab

Beam

Rebars:

2#5 Grade-60 non-prestressed top bars as follows:

top $A_{s1} := 2 \cdot 0.31in^2$ $d'_1 := h_o + h_s + h_b + 1.75in = 11 \cdot in$ distance from the top of the slab

Strands:

22 ea. 7/16 diamter Grade270-strands-stress relieved

Unamaged strands configuration:

$n := 7$ "number of layers" $d_{strand_1} := \frac{7}{16}in$

	number of strands	Area of one strand	Distance from bottom
Layer 1	$N_{1,1} := 6$	$A0_1 := 0.117in^2$	$H_1 := 2in$
Layer 2	$N_{2,1} := 6$	$A0_2 := 0.117in^2$	$H_2 := 4in$
Layer 3	$N_{3,1} := 2$	$A0_3 := 0.117in^2$	$H_3 := 6in$
Layer 4	$N_{4,1} := 2$	$A0_4 := 0.117in^2$	$H_4 := 8in$
Layer 5	$N_{5,1} := 2$	$A0_5 := 0.117in^2$	$H_5 := 16in$
Layer 6	$N_{6,1} := 2$	$A0_6 := 0.117in^2$	$H_6 := 20in$
Layer 7	$N_{7,1} := 2$	$A0_7 := 0.117in^2$	$H_7 := 28in$

Damaged strands configuration (Alfailakawi et al. (2020): $d_{strand_2} := \frac{7}{16}in$

	number of strands (second Lesner end)	number of strands (first Lesner end)
Layer 1	$N_{1,2} := 4 + 0.6 \cdot (1) + 0.8 \cdot (1) = 5.4$	$N_{1,2} := 5 + 0.6 \cdot (1) = 5.6$
Layer 2	$N_{2,2} := 5 + 0.8 \cdot (1) = 5.8$	$N_{2,2} := 5 + 0.8 \cdot (1) = 5.8$
Layer 3	$N_{3,2} := 2$	$N_{3,2} := 2$
Layer 4	$N_{4,2} := 2$	$N_{4,2} := 2$
Layer 5	$N_{5,2} := 2$	$N_{5,2} := 2$
Layer 6	$N_{6,2} := 2$	$N_{6,2} := 2$
Layer 7	$N_{7,2} := 2$	$N_{7,2} := 2$

Stirrups:

#4 double-legged stirrups $A_v := 2 \cdot 0.20in^2$ $f_{yt} := 48.5ksi$

CALCULATIONS FOR THE LESNER GIRDER:

Pre-Calculations:

$b_v := x_2$ $\quad b := x_1$

$L_3 := Length - (L_1 + L_4 + L_2)$ L3 is the distance from the point load to the right support

Properties of the strands:

$g := 1 .. cols(N)$ damage index

Total number of strands:

$$Num_g := \sum_{i=1}^{n} N_{i,g}$$

Total strands area:

$$A_{ps_g} := \sum_{i=1}^{n} \left(N_{i,g} \cdot A0_i\right)$$

Strands C.G from the bottom:

$$y'_{s_g} := \frac{N_{1,g} \cdot A0_1 \cdot H_1 + N_{2,g} \cdot A0_2 \cdot H_2 + N_{3,g} \cdot A0_3 \cdot H_3 + N_{4,g} \cdot A0_4 \cdot H_4 + N_{5,g} \cdot A0_5 \cdot H_5 + N_{6,g} \cdot A0_6 \cdot H_6 + N_{7,g} \cdot A0_7 \cdot H_7}{A_{ps_g}}$$

Properties of the bare beam:

Area:

$$A := (x_1 \cdot y_1) + (x_3 \cdot y_5) + \left[x_2 \cdot (y_3 + y_2 + y_4)\right] + 2 \cdot \left[0.5 \cdot \left(\frac{x_1 - x_2}{2}\right) \cdot y_2\right] + 2 \cdot \left[0.5 \cdot \left(\frac{x_3 - x_2}{2}\right) \cdot y_4\right] = 369 \cdot in^2$$

Centroid from the bottom:

$$y'_b := \frac{(x_1 \cdot y_1) \cdot \left(h - \frac{y_1}{2}\right) + (x_3 \cdot y_5) \cdot \left(\frac{y_5}{2}\right) + \left[x_2 \cdot (y_3 + y_2 + y_4)\right] \cdot \left(y_5 + \frac{y_4 + y_3 + y_2}{2}\right) + \left[2 \cdot \left[0.5 \cdot \left(\frac{x_1 - x_2}{2}\right) \cdot y_2\right]\right] \cdot \left(h - y_1 - \frac{y_2}{3}\right) + 2 \cdot \left[0.5 \cdot \left(\frac{x_3 - x_2}{2}\right) \cdot y_4\right] \cdot \left(y_5 + \frac{y_4}{3}\right)}{A} = 15.829 \cdot in$$

Moment of inertia:

$$I_1 := \frac{x_1 \cdot y_1^3}{12} + (x_1 \cdot y_1) \cdot \left[\left(h - \frac{y_1}{2}\right) - y'_b\right]^2 = 2.144 \times 10^4 \cdot in^4$$

$$I_2 := \frac{x_3 \cdot y_5^3}{12} + (x_3 \cdot y_5) \cdot \left(y'_b - \frac{y_5}{2}\right)^2 = 1.81 \times 10^4 \cdot in^4$$

$$I_3 := \frac{x_2 \cdot (y_3 + y_2 + y_4)^3}{12} + \left[x_2 \cdot (y_3 + y_2 + y_4)\right] \cdot \left[\left(y_5 + \frac{y_4 + y_3 + y_2}{2}\right) - y'_b\right]^2 = 7.591 \times 10^3 \cdot in^4$$

$$I_4 := \frac{\left(\frac{x_1 - x_2}{2}\right) \cdot y_2^3}{36} + \left[0.5 \cdot \left(\frac{x_1 - x_2}{2}\right) \cdot y_2\right] \cdot \left[\left(h - y_1 - \frac{y_2}{3}\right) - y'_b\right]^2 = 782.857 \cdot in^4$$

$$I_5 := \frac{\left(\frac{x_3 - x_2}{2}\right) \cdot y_4^3}{36} + \left[0.5 \cdot \left(\frac{x_3 - x_2}{2}\right) \cdot y_4\right] \cdot \left[y'_b - \left(y_5 + \frac{y_4}{3}\right)\right]^2 = 1.139 \times 10^3 \cdot in^4$$

$$I := I_1 + I_2 + I_3 + 2 \cdot I_4 + 2 \cdot I_5 = 5.098 \times 10^4 \cdot in^4$$

Shape modulus:

$$St := \frac{I}{h - y'_b} = 2.527 \times 10^3 \cdot in^3 \qquad Sb := \frac{I}{y'_b} = 3.221 \times 10^3 \cdot in^3$$

eccentricity:

$$e_g := y'_b - y'_{s_g}$$

Properties of the composite beam:

Using the transformed area method, convert the slab concrete to its equivalent of the beam concrete. We will convert the slab area by converting its width.

Note: We will ignore the deck rebars and the strands.

Find the modular ratio between deck and beams:

$E_c := 57000 \cdot \sqrt{f'_c \cdot 1psi} = 4.013 \times 10^3 \cdot ksi$ $E_{cdeck} := 57000 \cdot \sqrt{f'_{cdeck} \cdot 1psi} = 3.645 \times 10^3 \cdot ksi$

$n_{deck} := \frac{E_{cdeck}}{E_c} = 0.90835$ $n_{strand} := \frac{E_{ps}}{E_c} = 6.977$ $n_{steel} := \frac{E_s}{E_c} = 7.226$

$b_{tr} := n_{deck} \cdot b_{eff} = 2.876\,ft$ The transformed effective width of the slab

$b_{b.tr} := n_{deck} \cdot b_b = 10.9 \cdot in$ The transformed effective width of the haunch

$A_{deck} := b_{eff} \cdot (h_s + h_o) + b_b \cdot h_b = 325.5 \cdot in^2$ deck area with haunch

Find the transformed composite section properties (excluding the effect of strands):

Area:

$A_{Com} := A + n_{deck} \cdot A_{deck} = 664.667 \cdot in^2$

Centroid from the bottom:

$$y'_{Com} := \frac{(A \cdot y'_b) + \left[\left[b_{tr} \cdot (h_s + h_o)\right] \cdot \left[h + h_b + \frac{(h_s + h_o)}{2}\right]\right] + (b_{b.tr} \cdot h_b) \cdot \left(h + \frac{h_b}{2}\right)}{A_{Com}} = 27.006 \cdot in$$

Moment of inertia:

$$I_{Com} := \left[I + A \cdot (y'_{Com} - y'_b)^2\right] + \left[\left[\frac{b_{tr} \cdot (h_s + h_o)^3}{12}\right] + \left[b_{tr} \cdot (h_s + h_o)\right] \cdot \left(h + h_b + \frac{h_s + h_o}{2} - y'_{Com}\right)^2\right] + \left[\left(\frac{b_{b.tr} \cdot h_b^3}{12}\right) + (b_{b.tr} \cdot h_b) \cdot \left(h + \frac{h_b}{2} - y'_{Com}\right)^2\right] = 1.5643977 \times 10^5 \cdot in^4$$

Shape modulus:

$St_{Com} := \frac{I_{Com}}{h - y'_{Com}} = 1.739 \times 10^4 \cdot in^3$ $Sb_{Com} := \frac{I_{Com}}{y'_{Com}} = 5.793 \times 10^3 \cdot in^3$

eccentricity:

$e_{Com_g} := y'_{Com} - y'_{s_g}$

transfer length of strands AASHTO:

$l_{t_g} := 60 \cdot d_{strand_g}$

$$f'_{se}(x) := \begin{cases} f_{se} & \text{if } \left(Length - l_{t_1}\right) \geq x \geq l_{t_1} \\ \left(\frac{f_{se}}{l_{t_1}} \cdot x\right) & \text{if } x \leq l_{t_1} \\ \left[f_{se} - \left[\frac{f_{se}}{l_{t_1}} \cdot \left[x - \left(Length - l_{t_1}\right)\right]\right]\right] & \text{if } x \geq \left(Length - l_{t_1}\right) \end{cases}$$

Assume effective stress varies linearly from zero to fse within the transfer length

$P_{e_g} := f_{se} \cdot A_{ps_g}$ "effective force beyond the transfer length"

$P'_e(g, x) := f'_{se}(x) \cdot A_{ps_g}$

self weight:

$w_o := A \cdot \gamma = 0.384 \cdot \frac{kip}{ft}$

deck weight:

$w_{deck} := (A_{deck}) \cdot \gamma = 0.339 \cdot \frac{kip}{ft}$

Find shear and moment along the beam:

$$RB_d := \frac{(w_o + w_{deck}) \cdot Length \cdot \left(\frac{Length}{2} - L_1\right)}{L_2 + L_3}$$

Right support reaction due to unfactored self weight and deck weight

$$RA_d := \left[(w_o + w_{deck}) \cdot Length\right] - RB_d$$

Left support reaction due to unfactored self weight and deck weight

$$V_d(x) := \begin{cases} \left[-(w_o + w_{deck}) \cdot x\right] & \text{if } 0 \le x \le L_1 \\ \left[-(w_o + w_{deck}) \cdot x\right] + RA_d & \text{if } L_1 \le x \le (L_1 + L_2 + L_3) \\ \left[-(w_o + w_{deck}) \cdot x\right] + RA_d + RB_d & \text{if } (L_1 + L_2 + L_3) \le x \le Length \end{cases}$$

shear due to unfactored self weight and deck weight

$$M_d(x) := \begin{cases} \left[\frac{-(w_o + w_{deck})}{2} \cdot x^2\right] & \text{if } 0 \le x \le L_1 \\ \left[\frac{-(w_o + w_{deck})}{2} \cdot x^2\right] + \left[RA_d \cdot (x - L_1)\right] & \text{if } L_1 \le x \le (L_1 + L_2 + L_3) \\ \left[\frac{-(w_o + w_{deck})}{2} \cdot x^2\right] + \left[RA_d \cdot (x - L_1)\right] + \left[RB_d \cdot (x - L_1 - L_2 - L_3)\right] & \text{if } (L_1 + L_2 + L_3) \le x \le Length \end{cases}$$

Moment due to unfactored self weight and deck weight

$$RB_{applied}(P_{applied}) := \frac{P_{applied} \cdot L_2}{L_2 + L_3}$$

Right support reaction due to unfactored applied load

$$RA_{applied}(P_{applied}) := P_{applied} - RB_{applied}(P_{applied})$$

Left support reaction due to unfactored applied load

$$V_{applied}(x, P_{applied}) := \begin{cases} 0 & \text{if } 0 \le x \le L_1 \\ RA_{applied}(P_{applied}) & \text{if } L_1 \le x \le (L_1 + L_2) \\ RA_{applied}(P_{applied}) - P_{applied} & \text{if } (L_1 + L_2) \le x \le (L_1 + L_2 + L_3) \\ 0 & \text{if } (L_1 + L_2 + L_3) \le x \le Length \end{cases}$$

shear due to unfactored applied load

$$M_{applied}(x, P_{applied}) := \begin{cases} 0 & \text{if } 0 \le x \le L_1 \\ RA_{applied}(P_{applied}) \cdot (x - L_1) & \text{if } L_1 \le x \le (L_1 + L_2) \\ \left[RA_{applied}(P_{applied}) \cdot (x - L_1)\right] - \left[P_{applied} \cdot (x - L_1 - L_2)\right] & \text{if } (L_1 + L_2) \le x \le (L_1 + L_2 + L_3) \\ 0 & \text{if } (L_1 + L_2 + L_3) \le x \le Length \end{cases}$$

Moment due to unfactored applied load

$$V_{tot}(x, P_{applied}) := V_d(x) + V_{applied}(x, P_{applied})$$

shear due to all unfactored loads

$$M_{tot}(x, P_{applied}) := M_d(x) + M_{applied}(x, P_{applied})$$

Moment due to all factored loads

Calculate the flexural strength by the strain compatibility method:

$$d_{e_g} := h + h_s + h_o + h_b - y'_{s_g}$$

Find the depth of the compression block, a:

Assume the NA falls in the deck (i.e. a<hs+ho):

Find strains at failure:

-Strands (tension):

$$\varepsilon_1 := \frac{f_{se}}{E_{ps}}$$

$$\varepsilon_2(g) := \left| \begin{array}{l} \text{for } q \in 1 .. \text{rows}(N) \\ \quad \varepsilon_{2_q} \leftarrow \frac{1}{E_c} \cdot \left[\frac{P_{e_g}}{A} + \frac{P_{e_g} \cdot e_g \cdot \left(y'_b - H_q\right)}{I} \right] \\ \varepsilon_2 \end{array} \right.$$

the compatible strain component "from similar traingles"

$$\varepsilon_3(c) := \left| \begin{array}{l} \text{for } q \in 1 .. \text{rows}(N) \\ \quad \varepsilon_{3_q} \leftarrow \frac{\left[\left(h + h_s + h_o + h_b - H_q\right) - c\right]}{c} \cdot 0.003 \\ \varepsilon_3 \end{array} \right.$$

$$\varepsilon_{ps}(g, c) := \varepsilon_1 + \varepsilon_2(g) + \varepsilon_3(c)$$

-bottom rebars in deck (tension):

$$\varepsilon_{sdeckB}(c) := \frac{d'_{2deck} - c}{c} \cdot 0.003$$

-top rebars in deck (tension):

$$\varepsilon_{sdeckT}(c) := \frac{d'_{1deck} - c}{c} \cdot 0.003$$

-top rebars in beam (tension):

$$\varepsilon_s(c) := \frac{d'_1 - c}{c} \cdot 0.003$$

Find stresses at failure from stress-strain curves:

-Strands (tension):

$$f_{ps}(g, c) := \left| \begin{array}{l} \text{for } q \in 1 .. \text{rows}(N) \\ \quad f_{ps_q} \leftarrow f_s\left(\varepsilon_{ps}(g, c)_q\right) \\ f_{ps} \end{array} \right.$$

-top rebars in deck (tension):

$$f_{stdeckT}(c) := f_{deck}\left(\varepsilon_{sdeckT}(c)\right)$$

-top rebars in beam (tension):

$$f_{st}(c) := f\left(\varepsilon_s(c)\right)$$

-bottom rebars in deck (tension):

$$f_{stdeckB}(c) := f_{deck}\left(\varepsilon_{sdeckB}(c)\right)$$

Find Forces at failure:

-Strands (tension):

$$T_{ps}(g, c) := \left| \begin{array}{l} \text{for } q \in 1 .. \text{rows}(N) \\ \quad T_{ps_q} \leftarrow f_{ps}(g, c)_q \cdot \left(N_{q,g} \cdot A0_q\right) \\ T_{ps} \end{array} \right.$$

-bottom rebars in deck (tension):

$$T_{stdeckB}(c) := f_{stdeckB}(c) \cdot A_{s2deck}$$

-top rebars in deck (tension):

$$T_{stdeckT}(c) := f_{stdeckT}(c) \cdot A_{s1deck}$$

-top rebars in beam (tension):

$$T_{st}(c) := f_{st}(c) \cdot A_{s1}$$

-compression concrete block (compression):

$$\beta_{1deck} := \max\left[\left[0.85 - \left(\frac{f'_{cdeck} - 4000psi}{1000psi}\right) \cdot 0.05\right], 0.65\right] = 0.845$$

$$C_c(c) := 0.85 \cdot f'_{cdeck} \cdot b_{eff} \cdot \beta_{1deck} \cdot c$$

Here, we ignored subtracting the holes from the concrete area for simplicity

Total tensile force

$$T(g,c) := \sum_{q=1}^{rows(N)} T_{ps}(g,c)_q + T_{stdeckB}(c) + T_{stdeckT}(c) + T_{st}(c)$$

Total compressive force

$$C(c) := C_c(c)$$

Now, iterate on the Neutral Axis location for the undamaged section, c, until equilibrium:

Initial Values $c := 5in$

Given

$$T(g,c) = C(c)$$

$$c(g) := Find(c)$$

$$c_g := c(g) \qquad a_g := \beta_{1deck} \cdot c_g$$

Back calculate strains at failure based on c: "positive indicates tension"

-strands (tension):

$$\varepsilon_{ps_g} := \varepsilon_{ps}(g, c_g)$$

-bottom rebars in deck :

$$\varepsilon_{sdeckB_g} := \varepsilon_{sdeckB}(c_g)$$

-top rebars in deck:

$$\varepsilon_{sdeckT_g} := \varepsilon_{sdeckT}(c_g)$$

-top rebars in beam:

$$\varepsilon_{s_g} := \varepsilon_s(c_g)$$

Back calculate stresses at failure based on c: "positive indicates tension"

-Strands:

$$f_{ps_g} := f_{ps}(g, c_g)$$

-bottom rebars in deck:

$$f_{stdeckB_g} := f_{stdeckB}(c_g)$$

-top rebars in deck:

$$f_{stdeckT_g} := f_{stdeckT}(c_g)$$

-top rebars in beam:

$$f_{st_g} := f_{st}(c_g)$$

Back calculate forces at failure based on c: "positive indicates tension"

-Strands:

$T_{ps_g} := T_{ps}(g, c_g)$

-bottom rebars in deck:

$T_{stdeckB_g} := T_{stdeckB}(c_g)$

-compression concrete block:

$C_{c_g} := C_c(c_g)$

-top rebars in deck:

$T_{stdeckT_g} := T_{stdeckT}(c_g)$

-top rebars in beam:

$T_{st_g} := T_{st}(c_g)$

Total tensile force

$T_g := T(g, c_g)$

Total compressive force

$C_g := C(c_g)$

Calculate the nominal flexural strength "sum moment about extreme top fiber":

-Strands:

$$M_{n1}(g) := \left| \begin{array}{l} \text{for } q \in 1 .. \text{rows}(N) \\ \quad M_{n1_q} \leftarrow \left(T_{ps_g}\right)_q \cdot \left(h + h_s + h_o + h_b - H_q\right) \\ M_{n1} \end{array} \right.$$

-bottom rebars in deck:

$M_{n2}(g) := T_{stdeckB_g} \cdot d'_{2deck}$

-top rebars in deck:

$M_{n3}(g) := T_{stdeckT_g} \cdot d'_{1deck}$

-top rebars in beam:

$M_{n4}(g) := T_{st_g} \cdot d'_1$

-compression concrete block:

$M_{n5}(g) := \left(-C_c\right)_g \cdot \frac{a_g}{2}$

Moment capacity beyond the development length:

$$M_{n_g} := \sum_{q=1}^{\text{rows}(N)} M_{n1}(g)_q + M_{n2}(g) + M_{n3}(g) + M_{n4}(g) + M_{n5}(g)$$

development length of strands AASHTO 5.9.4.3.2-1:

$$l_{d_g} := \left(\frac{f_{psLumped_1} - \frac{2}{3} \cdot f_{se}}{ksi} \right) \cdot d_{strand_g}$$

ignore k factor

Now, find the moment capacity taking into account the transfer and development lengths:

$$f'_{ps}(g,x) := \left| \begin{array}{l} \text{for } q \in 1..\text{rows}(N) \\ \quad \left(f'_{ps}\right)_q \leftarrow \left(\frac{f_{se}}{l_{t_1}} \cdot x \right) \text{ if } 0 \le x \le l_{t_1} \\ \quad \left(f'_{ps}\right)_q \leftarrow f_{se} + \left[\frac{\left(f_{ps_g}\right)_q - f_{se}}{l_{d_1} - l_{t_1}} \cdot \left(x - l_{t_1}\right) \right] \text{ if } l_{t_1} \le x \le l_{d_1} \\ \quad \left(f'_{ps}\right)_q \leftarrow \left(f_{ps_g}\right)_q \text{ if } l_{d_1} \le x \le \left(\text{Length} - l_{d_1}\right) \\ \quad \left(f'_{ps}\right)_q \leftarrow \left(f_{ps_g}\right)_q - \left[\frac{\left(f_{ps_g}\right)_q - f_{se}}{l_{d_1} - l_{t_1}} \cdot \left[x - \left(\text{Length} - l_{d_1}\right)\right] \right] \text{ if } \left(\text{Length} - l_{d_1}\right) \le x \le \left(\text{Length} - l_{t_1}\right) \\ \quad \left(f'_{ps}\right)_q \leftarrow f_{se} - \left[\frac{f_{se}}{l_{t_1}} \cdot \left[x - \left(\text{Length} - l_{t_1}\right)\right] \right] \text{ if } \left(\text{Length} - l_{t_1}\right) \le x \le (\text{Length}) \\ f'_{ps} \end{array} \right.$$

Assume strand stress at the failure, fps, varies linearly from fse at the end of the transfer length to fps at the end of the development length.

$$T'_{ps}(g,x) := \left| \begin{array}{l} \text{for } q \in 1..\text{rows}(N) \\ \quad T'_{ps_q} \leftarrow f'_{ps}(g,x)_q \cdot \left(N_{q,g} \cdot A0_q\right) \\ T'_{ps} \end{array} \right.$$

$$M'_{n1}(g,x) := \left| \begin{array}{l} \text{for } q \in 1..\text{rows}(N) \\ \quad M'_{n1_q} \leftarrow T'_{ps}(g,x)_q \cdot \left(h + h_s + h_o + h_b - H_q\right) \\ M'_{n1} \end{array} \right.$$

$$M'_n(g,x) := \sum_{q=1}^{\text{rows}(N)} M'_{n1}(g,x)_q + \left(M_{n2}(g) + M_{n3}(g) + M_{n4}(g) + M_{n5}(g)\right)$$

Guess Value $\quad Pkill_{moment} := 150kip$

Given

$$M_{tot}\left(L_1 + L_2, Pkill_{moment}\right) = M'_n\left(g, L_1 + L_2\right)$$

$$PPkill_{moment}(g) := \text{Find}\left(Pkill_{moment}\right)$$

$$PPkill_{moment_g} := PPkill_{moment}(g)$$

Calculate the cracking moment :

Find the modulus of rupture for the concrete

$$f_r := 7.5 \cdot \sqrt{f'_c \cdot psi} = 0.528 \cdot ksi$$

Find the stress at the bottom fiber:

$$f_{bot}(g, x, P_{applied}) := \frac{-P_{e_g}}{A} + \frac{-P_{e_g} \cdot e_g \cdot y'_b}{I} + \frac{M_d(x) \cdot y'_b}{I} + \frac{M_{applied}(x, P_{applied}) \cdot y'_{Com}}{I_{Com}}$$

Now, solve for the cracking moment by setting the bottom tensile stresses equal to the concrete modulus of rupture:

$$\frac{-P_{e_g}}{A} + \frac{-P_{e_g} \cdot e_g \cdot y'_b}{I} + \frac{M_d(x) \cdot y'_b}{I} + \frac{M_{cr} \cdot y'_{Com}}{I_{Com}} = f_r$$

$$M_{crApplied}(g, x) := \frac{I_{Com}}{y'_{Com}} \cdot \left[f_r - \left(\frac{-P'_e(g, x)}{A} + \frac{-P'_e(g, x) \cdot e_g \cdot y'_b}{I} + \frac{M_d(x) \cdot y'_b}{I} \right) \right]$$

applied moment by actuator to cause cracking

$$M_{crTotal}(g, x) := M_{crApplied}(g, x) + M_d(x)$$

total moment (by dead load and actuator) to cause cracking

Load to cause flexural crack:

Guess Value $P_{CR} := 10kip$

Given

$$M_{crApplied}(g, L_1 + L_2) = M_{applied}(L_1 + L_2, P_{CR})$$

$$P_{CR}(g) := Find(P_{CR})$$

$$P_{CR_g} := P_{CR}(g)$$

Calculate the shear strength using the AASHTO A5.8.3.4.2 :

$$d_{v_g} := \max\left[\left(d_{e_g} - \frac{a_g}{2}\right), \left(0.9 \cdot d_{e_g}\right), \left[0.72 \cdot \left(h + h_s + h_o + h_b\right)\right]\right]$$

$V_p(x) := 0$ All strands are straight. No shear is carried by the vertical component of the strands.

$N_{tot} := 0$ No axial load

$As := 0$ area of the nonprestreesed bars on the flexural tension side

$$Aps_g := \sum_{i=1}^{6} \left(N_{i,g} \cdot A0_i\right)$$ "6 layers of strands are in the flexural tensile side"

$f_{po} := f_{pj}$

$$Ac := \left(x_3 \cdot y_5\right) + 2 \cdot \left[0.5 \cdot \left(\frac{x_3 - x_2}{2}\right) \cdot y_4\right] + \left[\left(\frac{h + h_s + h_o + h_b}{2} - y_5\right) \cdot x_2\right] = 243.75 \cdot in^2$$

$$\varepsilon_s\left(g, x, P_{applied}\right) := \frac{\left(\frac{\left|M_{tot}\left(x, P_{applied}\right)\right|}{d_{v_g}}\right) + 0.5 \cdot N_{tot} + \left|V_{tot}\left(x, P_{applied}\right) - V_p(x)\right| - Aps_g \cdot f_{po}}{E_s \cdot As + E_{ps} \cdot Aps_g}$$

$$\varepsilon_s\left(g, x, P_{applied}\right) := \begin{cases} \varepsilon_s\left(g, x, P_{applied}\right) & \text{if } \varepsilon_s\left(g, x, P_{applied}\right) \geq 0 \\ \dfrac{\left(\frac{\left|M_{tot}\left(x, P_{applied}\right)\right|}{d_{v_g}}\right) + 0.5 \cdot N_{tot} + \left|V_{tot}\left(x, P_{applied}\right) - V_p(x)\right| - Aps_g \cdot f_{po}}{E_s \cdot As + E_{ps} \cdot Aps_g + E_c \cdot Ac} & \text{if } \varepsilon_s\left(g, x, P_{applied}\right) < 0 \end{cases}$$

$$\varepsilon_s\left(g, x, P_{applied}\right) := \min\left(\varepsilon_s\left(g, x, P_{applied}\right), 6 \cdot 10^{-3}\right)$$

$$\beta\left(g, x, P_{applied}\right) := \frac{4.8}{1 + 750 \cdot \varepsilon_s\left(g, x, P_{applied}\right)}$$

$\theta\left(g, x, P_{applied}\right) := 29 + 3500 \cdot \varepsilon_s\left(g, x, P_{applied}\right)$ angle in degree

$$V_c\left(g, x, P_{applied}\right) := 0.0316 \cdot \beta\left(g, x, P_{applied}\right) \cdot \sqrt{f'_c \cdot ksi} \cdot b_v \cdot d_{v_g}$$

$$V_s\left(g, x, P_{applied}\right) := \frac{A_v \cdot f_{yt} \cdot d_{v_g}}{6in} \cdot \cot\left(\theta\left(g, x, P_{applied}\right) \cdot \frac{\pi}{180}\right)$$

$V_n\left(g, x, P_{applied}\right) := V_c\left(g, x, P_{applied}\right) + V_s\left(g, x, P_{applied}\right)$

Now, calculate the shear strength at the critical section for shear:

$x_{o_g} := L_1 + 4in + d_{v_g}$

$V_{demand}\left(x, P_{applied}\right) := \left|V_{tot}\left(x, P_{applied}\right)\right|$

$V_{capacity}\left(g, x, P_{applied}\right) := \left|V_n\left(g, x, P_{applied}\right)\right|$

Iterate on the applied load :

Initial value $P_{applied} := 150kip$

Given $V_{demand}\left(x_{o_g}, P_{applied}\right) = V_{capacity}\left(g, x_{o_g}, P_{applied}\right)$

$P_{kill}(g) := \text{Find}\left(P_{applied}\right)$

$PP_{kill_g} := P_{kill}(g)$ Load to kill

$VV_{n_g} := V_n\left(g, x_{o_g}, PP_{kill_g}\right)$ Shear strength

Calculate the shear strength using the AASHTO Appendix B.5 :

$$d_{v_g} := \max\left[\left(d_{e_g} - \frac{a_g}{2}\right), \left(0.9 \cdot d_{e_g}\right), \left[0.72 \cdot \left(h + h_s + h_o + h_b\right)\right]\right]$$

$V_p(x) := 0$ All strands are straight. No shear is carried by the vertical component of the strands.

$N_{tot} := 0$ No axial load

$As := 0$ area of the nonprestreesed bars on the flexural tension side

$$Aps_g := \sum_{i=1}^{6} \left(N_{i,g} \cdot A0_i\right)$$ "6 layers of strands are in the flexural tensile side"

$f_{po} := f_{pj}$

$$Ac := \left(x_3 \cdot y_5\right) + 2 \cdot \left[0.5 \cdot \left(\frac{x_3 - x_2}{2}\right) \cdot y_4\right] + \left[\left(\frac{h + h_s + h_o + h_b}{2} - y_5\right) \cdot x_2\right] = 243.75 \cdot in^2$$

$$\nu_u\left(g, x, P_{applied}\right) := \frac{\left|V_{tot}\left(x, P_{applied}\right)\right|}{b_v \cdot d_{v_g}}$$

$$\nu uByfc\left(g, x, P_{applied}\right) := \frac{\nu_u\left(g, x, P_{applied}\right)}{f'_c}$$

$$\varepsilon_s\left(g, x, P_{applied}, \theta\right) := \frac{\left(\frac{\left|M_{tot}\left(x, P_{applied}\right)\right|}{d_{v_g}}\right) + 0.5 \cdot N_{tot} + 0.5\left|V_{tot}\left(x, P_{applied}\right) - V_p(x)\right| \cdot \cot\left(\theta \cdot \frac{\pi}{180}\right) - Aps_g \cdot f_{po}}{2\left(E_s \cdot As + E_{ps} \cdot Aps_g\right)}$$

$$\varepsilon_s\left(g, x, P_{applied}, \theta\right) := \begin{cases} \varepsilon_s\left(g, x, P_{applied}, \theta\right) & \text{if } \varepsilon_s\left(g, x, P_{applied}, \theta\right) \geq 0 \\ \dfrac{\left(\frac{\left|M_{tot}\left(x, P_{applied}\right)\right|}{d_{v_g}}\right) + 0.5 \cdot N_{tot} + 0.5\left|V_{tot}\left(x, P_{applied}\right) - V_p(x)\right| \cdot \cot\left(\theta \cdot \frac{\pi}{180}\right) - Aps_g \cdot f_{po}}{2\left(E_s \cdot As + E_{ps} \cdot Aps_g + E_c \cdot Ac\right)} & \text{if } \varepsilon_s\left(g, x, P_{applied}, \theta\right) < 0 \end{cases}$$

Use Table 14.9 to estimate the values for θ and β:

$\theta\text{and}\beta(g, x, P_{applied}, \theta) :=$

$\frac{v_u}{f'_c}$	$\varepsilon_x \times 1{,}000$								
	≤−0.20	≤−0.10	≤−0.05	≤0	≤0.125	≤0.25	≤0.50	≤0.75	≤1.00
≤0.075	22.3 6.32	20.4 4.75	21.0 4.10	21.8 3.75	24.3 3.24	26.6 2.94	30.5 2.59	33.7 2.38	36.4 2.23
≤0.100	18.1 3.79	20.4 3.38	21.4 3.24	22.5 3.14	24.9 2.91	27.1 2.75	30.8 2.50	34.0 2.32	36.7 2.18
≤0.125	19.9 3.18	21.9 2.99	22.8 2.94	23.7 2.87	25.9 2.74	27.9 2.62	31.4 2.42	34.4 2.26	37.0 2.13
≤0.150	21.6 2.88	23.3 2.79	24.2 2.78	25.0 2.72	26.9 2.60	28.8 2.52	32.1 2.36	34.9 2.21	37.3 2.08
≤0.175	23.2 2.73	24.7 2.66	25.5 2.65	26.2 2.60	28.0 2.52	29.7 2.44	32.7 2.28	35.2 2.14	36.8 1.96
≤0.200	24.7 2.63	26.1 2.59	26.7 2.52	27.4 2.51	29.0 2.43	30.6 2.37	32.8 2.14	34.5 1.94	36.1 1.79
≤0.225	26.1 2.53	27.3 2.45	27.9 2.42	28.5 2.40	30.0 2.34	30.8 2.14	32.3 1.86	34.0 1.73	35.7 1.64
≤0.250	27.5 2.39	28.6 2.39	29.1 2.33	29.7 2.33	30.6 2.12	31.3 1.93	32.8 1.70	34.3 1.58	35.8 1.50

$\theta(g, x, P_{applied}) :=$ start with 30 degrees

$\theta_{ini} \leftarrow 30$

$\theta_1 \leftarrow \theta\text{and}\beta(g, x, P_{applied}, \theta_{ini})$

$\theta_2 \leftarrow \theta\text{and}\beta(g, x, P_{applied}, \theta_{1_1})$

$\theta_3 \leftarrow \theta\text{and}\beta(g, x, P_{applied}, \theta_{2_1})$

$\theta_4 \leftarrow \theta\text{and}\beta(g, x, P_{applied}, \theta_{3_1})$

$\theta_5 \leftarrow \theta\text{and}\beta(g, x, P_{applied}, \theta_{4_1})$

$\theta_6 \leftarrow \theta\text{and}\beta(g, x, P_{applied}, \theta_{5_1})$

$\theta \leftarrow \theta_6$

θ

$\beta(g, x, P_{applied}) := \theta(g, x, P_{applied})2$

$\theta(g, x, P_{applied}) := \theta(g, x, P_{applied})1$

$V_c(g, x, P_{applied}) := 0.0316 \cdot \beta(g, x, P_{applied}) \cdot \sqrt{f'_c \cdot ksi} \cdot b_v \cdot d_{v_g}$

$V_s(g, x, P_{applied}) := \frac{A_v \cdot f_{yt} \cdot d_{v_g}}{6in} \cdot \cot\left(\theta(g, x, P_{applied}) \cdot \frac{\pi}{180}\right)$

$V_n(g, x, P_{applied}) := V_c(g, x, P_{applied}) + V_s(g, x, P_{applied})$

Now, calculate the shear strength at the critical section for shear:

$x_{o_g} := L_1 + 4in + d_{v_g}$

$V_{demand}(x, P_{applied}) := |V_{tot}(x, P_{applied})|$

$V_{capacity}(g, x, P_{applied}) := |V_n(g, x, P_{applied})|$

Iterate on the applied load :

$Diff(P, g) := |V_{capacity}(g, x_{o_g}, P) - V_{demand}(x_{o_g}, P)|$

$P_{kill.guess} := 200kip$

$PP_{kill}(g) := Minimize(Diff, P_{kill.guess})$

$PP_{kill_g} := PP_{kill}(g)$ Load to kill

$VV_{n_g} := V_n(g, x_{o_g}, PP_{kill_g})$ Shear strength

Calculate the shear strength using the ACI Vci-Vcw :

$$d_{p_g} := \max\left[d_{p_g}, \left[0.8 \cdot \left(h + h_s + h_o + h_b\right)\right]\right]$$

Calculate Vcw:

$$f_{pc}(g,x) := \frac{-P'_e(g,x)}{A} + \frac{P'_e(g,x) \cdot e_g \cdot \left(y'_{Com} - y'_b\right)}{I} - \frac{M_d(x) \cdot \left(y'_{Com} - y'_b\right)}{I}$$

Defintion of fpc for composite section

$$f_{pc}(g,x) := \left|f_{pc}(g,x)\right|$$

$$V_p(x) := 0$$

All strands are straight. No shear is carried by the vertical component of the strands.

$$V_{cw}(g,x) := \left[\left(3.5 \cdot \lambda \cdot \sqrt{f'_c \cdot psi} + 0.3 \cdot f_{pc}(g,x)\right) b_w \cdot d_{p_g}\right] + V_p(x)$$

$$V_{cw}(g,x) := \left[\left(4 \cdot \sqrt{f'_c \cdot psi} \cdot \sqrt{1 + \frac{f_{pc}(g,x)}{4 \cdot \sqrt{f'_c \cdot psi}}}\right) b_w \cdot d_{p_g}\right] + V_p(x)$$

Calculate Vci:

$$f_{pe}(g,x) := \frac{P'_e(g,x)}{A} + \frac{P'_e(g,x) \cdot e_g \cdot y'_b}{I}$$

concrete comp. stress due to effective prestress at tension face

$$f_d(x) := \frac{M_d(x) \cdot y'_b}{I}$$

concrete tensile stress due to unfactored self weight and deck weight at tension face

$$M_{cre}(g,x) := \frac{I_{Com}}{y'_{Com}} \cdot \left(\lambda \cdot \ 6 \ \cdot \sqrt{f'_c \cdot psi} + f_{pe}(g,x) - f_d(x)\right)$$

$$VibyMmax\left(x, P_{applied}\right) := \frac{\left|V_{tot}\left(x, P_{applied}\right) - V_d(x)\right|}{\left|M_{tot}\left(x, P_{applied}\right) - M_d(x)\right|}$$

$$V_{ci}\left(g, x, P_{applied}\right) := \left(0.6 \cdot \lambda \cdot \sqrt{f'_c \cdot psi} \cdot b_w \cdot d_{p_g}\right) + \left(M_{cre}(g,x) \cdot VibyMmax\left(x, P_{applied}\right)\right) + \left|V_d(x)\right|$$

$$Vmin_{ci}(g,x) := 2 \cdot \lambda \cdot \sqrt{f'_c \cdot psi} \cdot b_w \cdot d_{p_g}$$

Calculate the controlling Vc:

Now, calculate the controlling concrete shear strength contribution:

Shear strength:

$$V'_c\left(g, x, P_{applied}\right) := \min\left(V_{cw}(g,x), V_{ci}\left(g, x, P_{applied}\right)\right)$$

$$V_c\left(g, x, P_{applied}\right) := \max\left(V'_c\left(g, x, P_{applied}\right), Vmin_{ci}(g,x)\right)$$

Calculate the Vs:

Now, find the contribution of stirrups to the shear strength of the section:

$$V_s(g) := \frac{A_v \cdot f_{yt} \cdot d_{p_g}}{6in}$$

Calculate the Vn:

$$V_n\left(g, x, P_{applied}\right) := V_c\left(g, x, P_{applied}\right) + V_s(g)$$

Now, calculate the shear strength at the critical section for shear (per AASHTO):

$$x_{o_g} := L_1 + 4in + \left(d_{p_g} - \frac{a_g}{2} \right)$$

$$V_{demand}(x, P_{applied}) := \left| V_{tot}(x, P_{applied}) \right|$$

$$V_{capacity}(g, x, P_{applied}) := \left| V_n(g, x, P_{applied}) \right|$$

Iterate on the applied load :

Initial value $P_{applied} := 150kip$

Given $V_{demand}(x_{o_g}, P_{applied}) = V_{capacity}(g, x_{o_g}, P_{applied})$

$P_{kill}(g) := Find(P_{applied})$

$PP_{kill_g} := P_{kill}(g)$ Load to kill

$VV_{n_g} := V_n(g, x_{o_g}, PP_{kill_g})$ Shear strength

OUTPUT FOR THE LESNER GIRDER (FIRST TEST) :

FLEXURAL CALCS :

$M_{n_1} = 1.866 \times 10^3 \cdot kip \cdot ft$ Unamaged moment capacity

$M_{n_2} = 1.812 \times 10^3 \cdot kip \cdot ft$ Damaged moment capacity

$PPkill_{moment_1} = 262.482 \cdot kip$ Load to cause flexural failure at the point load location for undamaged condition

$PPkill_{moment_2} = 254.326 \cdot kip$ Load to cause flexural failure at the point load location for damaged condition

$P_{CR_1} = 144.102 \cdot kip$ Load to cause flexural cracking at the point load location for undamaged condition

$P_{CR_2} = 138.931 \cdot kip$ Load to cause flexural cracking at the point load location for damaged condition

SHEAR CALCS USING AASHTO A5.8.3.4.2 :

$VV_{n_1} = 232.605 \cdot kip$ Undamaged shear strength at the critical section for shear

$VV_{n_2} = 227.919 \cdot kip$ Damaged shear strength at the critical section for shear

$PP_{kill_1} = 260.913 \cdot kip$ Load to cause shear failure at the critical section for undamaged condition

$PP_{kill_2} = 255.285 \cdot kip$ Load to cause shear failure at the critical section for damaged condition

Shear strength and shear demand along the shear span under the actual failure load:

$P_{test} := 264.84kip$ Failure load from test

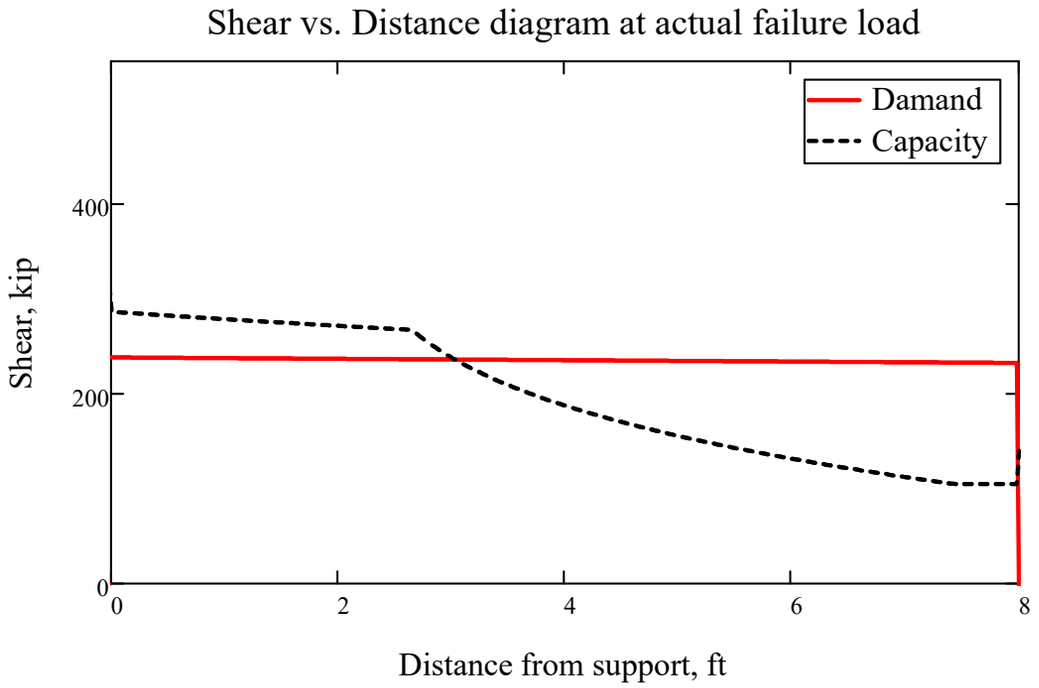

SHEAR CALCS USING AASHTO APPENDIX B.5 :

$VV_{n_1} = 223.979 \cdot kip$ Undamaged shear strength at the critical section for shear

$VV_{n_2} = 223.246 \cdot kip$ Damaged shear strength at the critical section for shear

$PP_{kill_1} = 250.795 \cdot kip$ Load to cause shear failure at the critical section for undamaged condition

$PP_{kill_2} = 249.678 \cdot kip$ Load to cause shear failure at the critical section for damaged condition

Shear strength and shear demand along the shear span under the actual failure load:

$P_{test} := 264.84kip$ Failure load from test

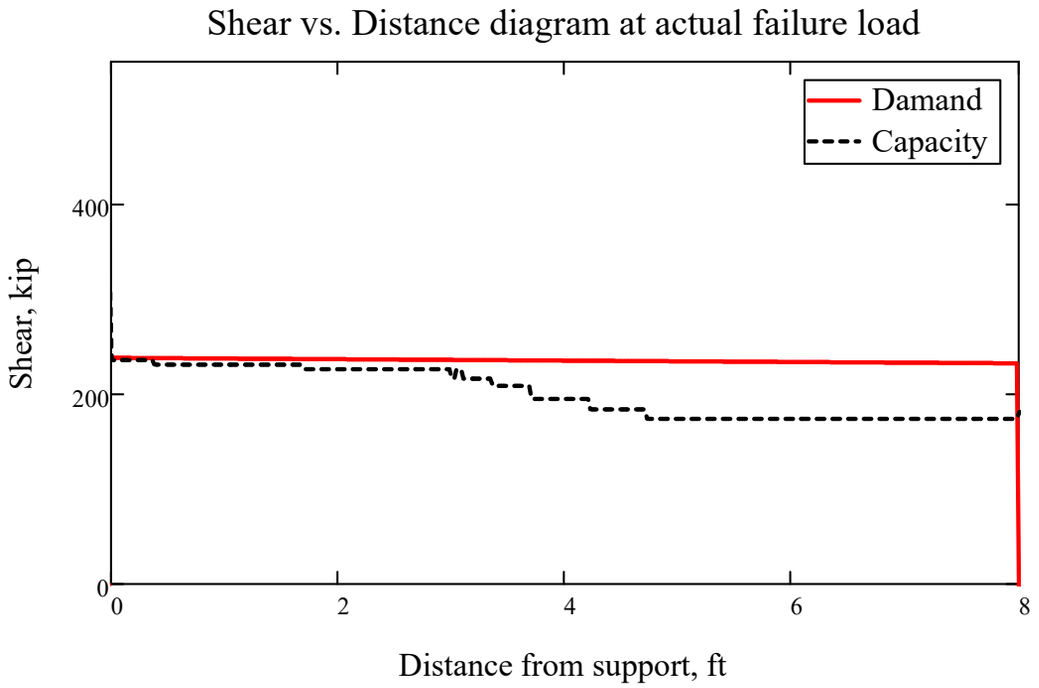

SHEAR CALCS USING ACI Vci-Vcw :

$VV_{n_1} = 225.972 \cdot kip$ Undamaged shear strength at the critical section for shear

$VV_{n_2} = 225.013 \cdot kip$ Damaged shear strength at the critical section for shear

$PP_{kill_1} = 252.956 \cdot kip$ Load to cause shear failure at the critical section for undamaged condition

$PP_{kill_2} = 251.797 \cdot kip$ Load to cause shear failure at the critical section for damaged condition

Shear strength and shear demand along the shear span under the actual failure load:

$P_{test} := 264.84kip$ Failure load from test

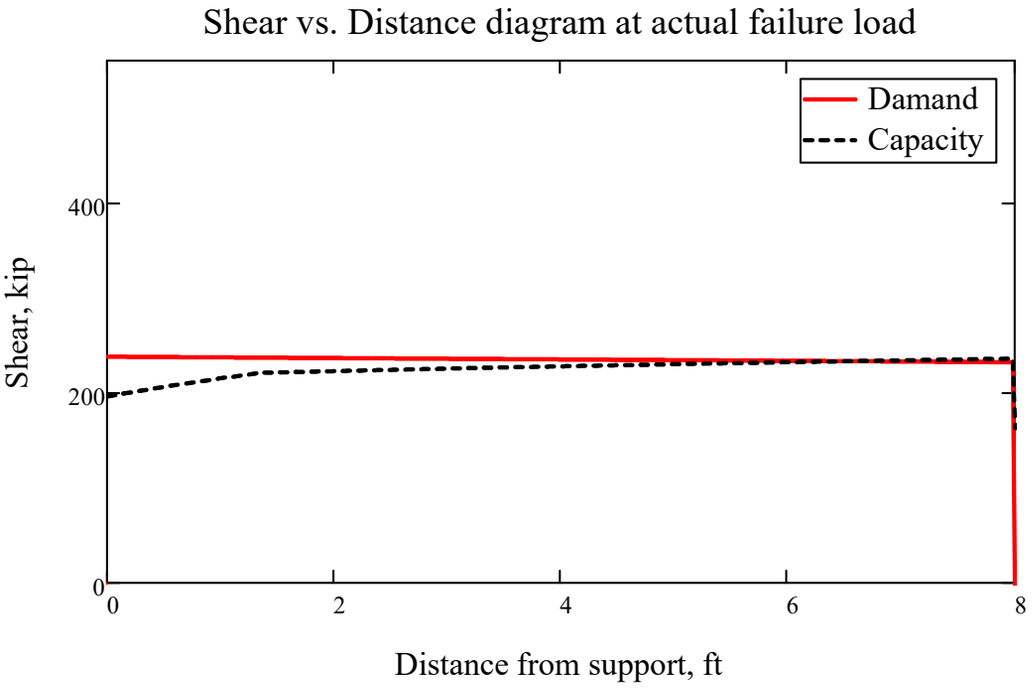

OUTPUT FOR THE LESNER GIRDER (SECOND TEST) :

FLEXURAL CALCS :

$M_{n_1} = 1.866 \times 10^3 \cdot kip \cdot ft$ Unamaged moment capacity

$M_{n_2} = 1.793 \times 10^3 \cdot kip \cdot ft$ Damaged moment capacity

$PPkill_{moment_1} = 373.426 \cdot kip$ Load to cause flexural failure at the point load location for undamaged condition

$PPkill_{moment_2} = 358.525 \cdot kip$ Load to cause flexural failure at the point load location for damaged condition

$P_{CR_1} = 224.533 \cdot kip$ Load to cause flexural cracking at the point load location for undamaged condition

$P_{CR_2} = 215.064 \cdot kip$ Load to cause flexural cracking at the point load location for damaged condition

SHEAR CALCS USING AASHTO A5.8.3.4.2 :

$VV_{n_1} = 232.605 \cdot kip$ Undamaged shear strength at the critical section for shear

$VV_{n_2} = 226.332 \cdot kip$ Damaged shear strength at the critical section for shear

$PP_{kill_1} = 277.331 \cdot kip$ Load to cause shear failure at the critical section for undamaged condition

$PP_{kill_2} = 269.627 \cdot kip$ Load to cause shear failure at the critical section for damaged condition

Shear strength and shear demand along the shear span under the actual failure load:

$P_{test} := 382.44kip$ Failure load from test

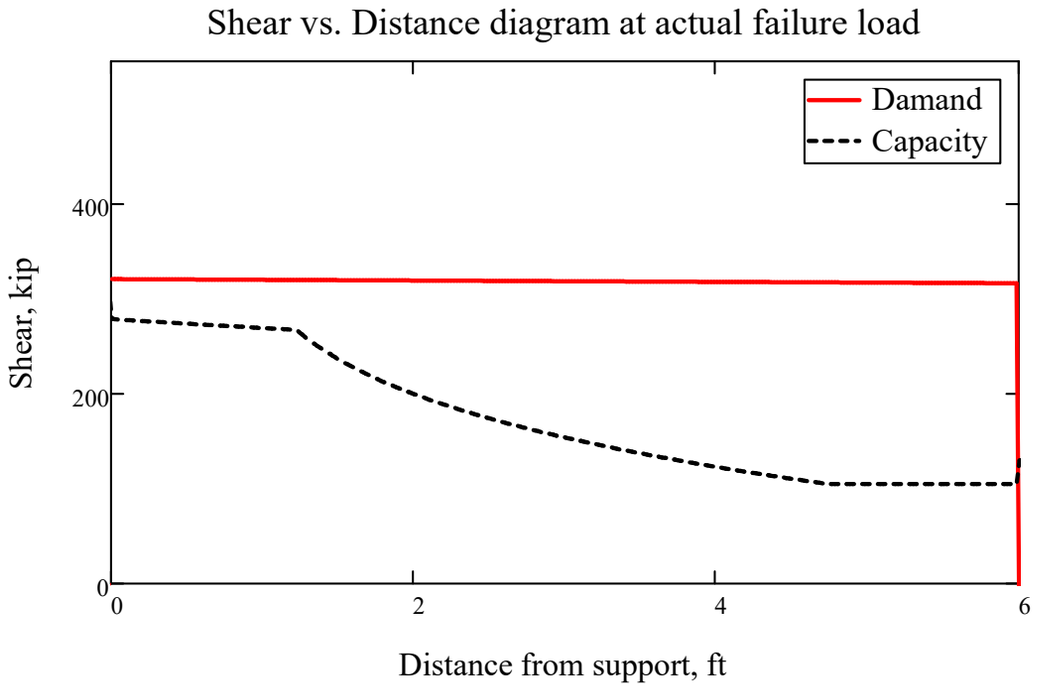

SHEAR CALCS USING AASHTO APPENDIX B.5 :

$VV_{n_1} = 223.979 \cdot kip$ Undamaged shear strength at the critical section for shear

$VV_{n_2} = 222.946 \cdot kip$ Damaged shear strength at the critical section for shear

$PP_{kill_1} = 266.987 \cdot kip$ Load to cause shear failure at the critical section for undamaged condition

$PP_{kill_2} = 265.474 \cdot kip$ Load to cause shear failure at the critical section for damaged condition

Shear strength and shear demand along the shear span under the actual failure load:

$P_{test} := 382.44kip$ Failure load from test

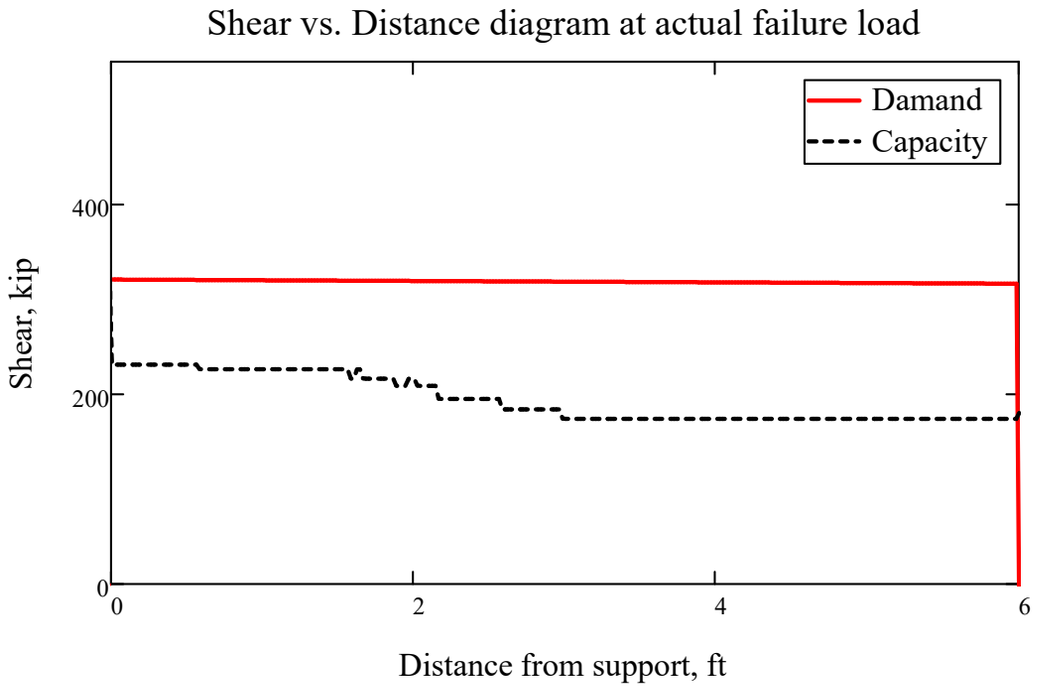

SHEAR CALCS USING ACI Vci-Vcw :

$VV_{n_1} = 221.368 \cdot kip$ Undamaged shear strength at the critical section for shear

$VV_{n_2} = 220.123 \cdot kip$ Damaged shear strength at the critical section for shear

$PP_{kill_1} = 263.55 \cdot kip$ Load to cause shear failure at the critical section for undamaged condition

$PP_{kill_2} = 262.011 \cdot kip$ Load to cause shear failure at the critical section for damaged condition

Shear strength and shear demand along the shear span under the actual failure load:

$P_{test} := 382.44kip$ Failure load from test

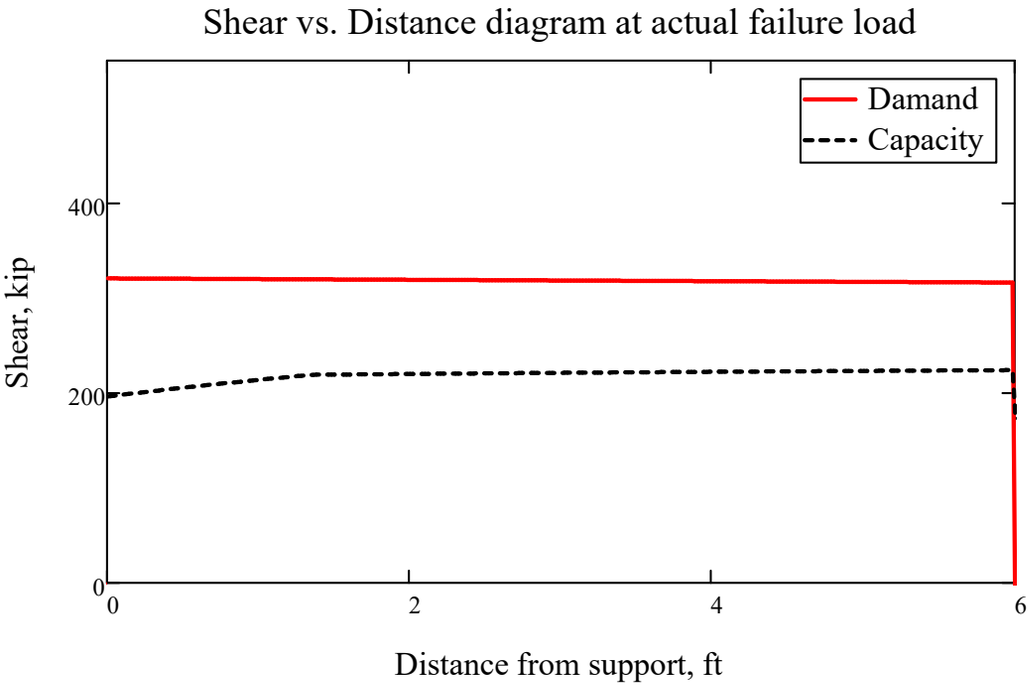

OUTPUT FOR THE ADEN GIRDER (FIRST TEST) :

FLEXURAL CALCS :

$M_{n_1} = 1.48 \times 10^3 \cdot kip \cdot ft$ Unamaged moment capacity

$M_{n_2} = 1.343 \times 10^3 \cdot kip \cdot ft$ Damaged moment capacity

$PPkill_{moment_1} = 357.504 \cdot kip$ Load to cause flexural failure at the point load location for undamaged condition

$PPkill_{moment_2} = 322.71 \cdot kip$ Load to cause flexural failure at the point load location for damaged condition

$P_{CR_1} = 235.138 \cdot kip$ Load to cause flexural cracking at the point load location for undamaged condition

$P_{CR_3} = 222.167 \cdot kip$ Load to cause flexural cracking at the point load location for damaged condition

SHEAR CALCS USING AASHTO A5.8.3.4.2 :

$VV_{n_1} = 197.622 \cdot kip$ Undamaged shear strength at the critical section for shear

$VV_{n_2} = 194.902 \cdot kip$ Damaged shear strength at the critical section for shear

$PP_{kill_1} = 194.359 \cdot kip$ Load to cause shear failure at the critical section for undamaged condition

$PP_{kill_2} = 191.418 \cdot kip$ Load to cause shear failure at the critical section for damaged condition

Shear strength and shear demand along the shear span under the actual failure load:

$P_{test} := 259.19kip$ Failure load from test

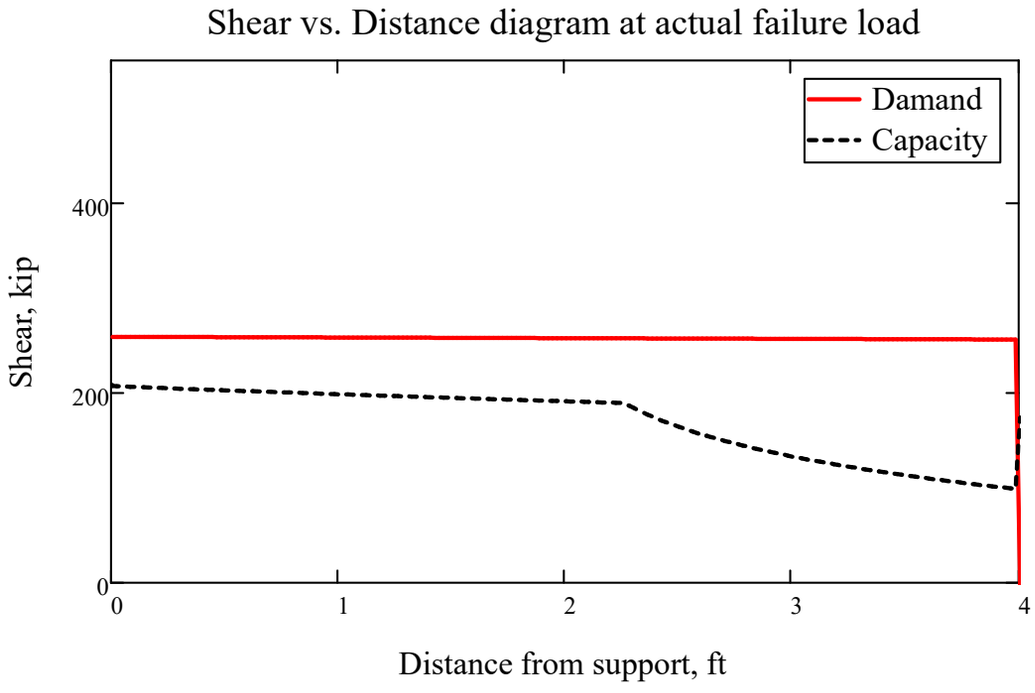

SHEAR CALCS USING AASHTO APPENDIX B.5 :

$VV_{n_1} = 175.604 \cdot kip$ Undamaged shear strength at the critical section for shear

$VV_{n_2} = 179.764 \cdot kip$ Damaged shear strength at the critical section for shear

$PP_{kill_1} = 172.382 \cdot kip$ Load to cause shear failure at the critical section for undamaged condition

$PP_{kill_2} = 172.381 \cdot kip$ Load to cause shear failure at the critical section for damaged condition

Shear strength and shear demand along the shear span under the actual failure load:

$P_{test} := 259.19kip$ Failure load from test

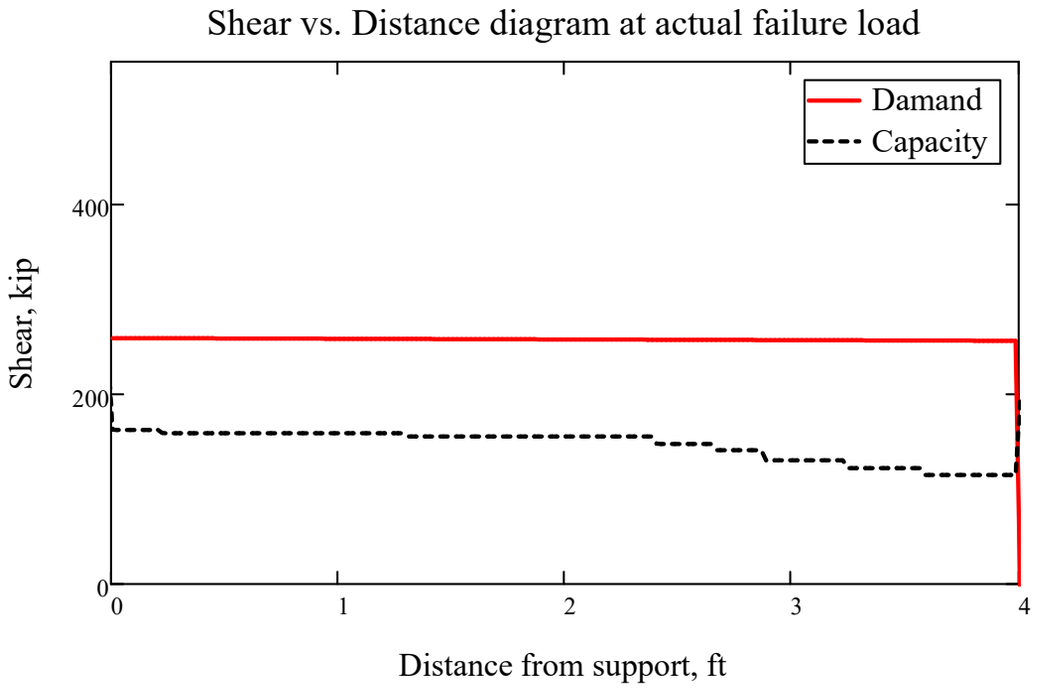

SHEAR CALCS USING ACI Vci-Vcw :

$VV_{n_1} = 202.276 \cdot kip$ Undamaged shear strength at the critical section for shear

$VV_{n_2} = 197.776 \cdot kip$ Damaged shear strength at the critical section for shear

$PP_{kill_1} = 199.419 \cdot kip$ Load to cause shear failure at the critical section for undamaged condition

$PP_{kill_2} = 194.563 \cdot kip$ Load to cause shear failure at the critical section for damaged condition

Shear strength and shear demand along the shear span under the actual failure load:

$P_{test} := 259.19kip$ Failure load from test

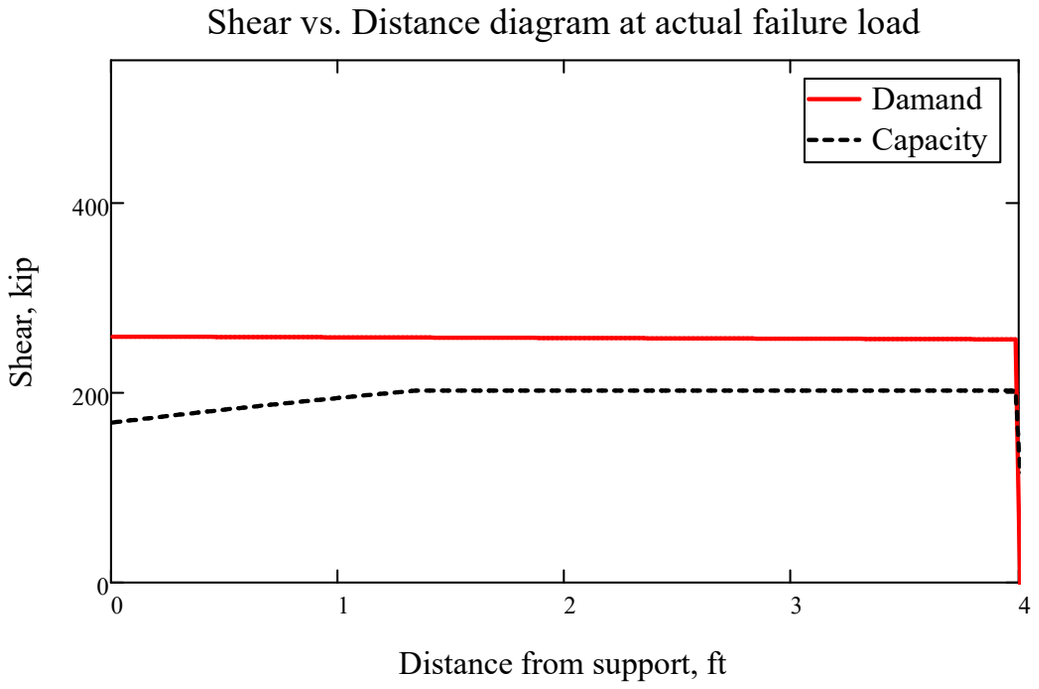

OUTPUT FOR THE ADEN GIRDER (SECOND TEST) :

FLEXURAL CALCS :

$M_{n_1} = 1.48 \times 10^3 \cdot kip \cdot ft$ Unamaged moment capacity

$M_{n_2} = 933.469 \cdot kip \cdot ft$ Damaged moment capacity

$PPkill_{moment_1} = 354.872 \cdot kip$ Load to cause flexural failure at the point load location for undamaged condition

$PPkill_{moment_2} = 217.931 \cdot kip$ Load to cause flexural failure at the point load location for damaged condition

$P_{CR_1} = 242.766 \cdot kip$ Load to cause flexural cracking at the point load location for undamaged condition

$P_{CR_3} = 167.367 \cdot kip$ Load to cause flexural cracking at the point load location for damaged condition

SHEAR CALCS USING AASHTO A5.8.3.4.2 :

$VV_{n_1} = 197.619 \cdot kip$ Undamaged shear strength at the critical section for shear

$VV_{n_2} = 174.348 \cdot kip$ Damaged shear strength at the critical section for shear

$PP_{kill_1} = 201.397 \cdot kip$ Load to cause shear failure at the critical section for undamaged condition

$PP_{kill_2} = 175.856 \cdot kip$ Load to cause shear failure at the critical section for damaged condition

Shear strength and shear demand along the shear span under the actual failure load:

$P_{test} := 230.53kip$ Failure load from test

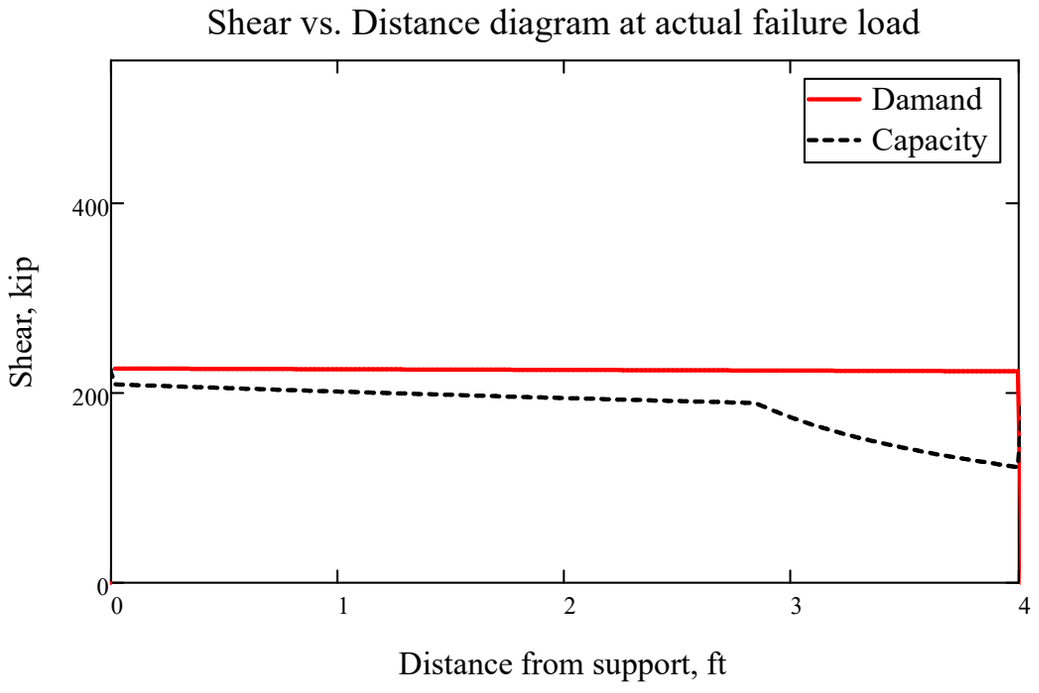

SHEAR CALCS USING AASHTO APPENDIX B.5 :

$VV_{n_1} = 175.604 \cdot kip$ Undamaged shear strength at the critical section for shear

$VV_{n_2} = 166.742 \cdot kip$ Damaged shear strength at the critical section for shear

$PP_{kill_1} = 179.088 \cdot kip$ Load to cause shear failure at the critical section for undamaged condition

$PP_{kill_2} = 167.508 \cdot kip$ Load to cause shear failure at the critical section for damaged condition

Shear strength and shear demand along the shear span under the actual failure load:

$P_{test} := 230.53kip$ Failure load from test

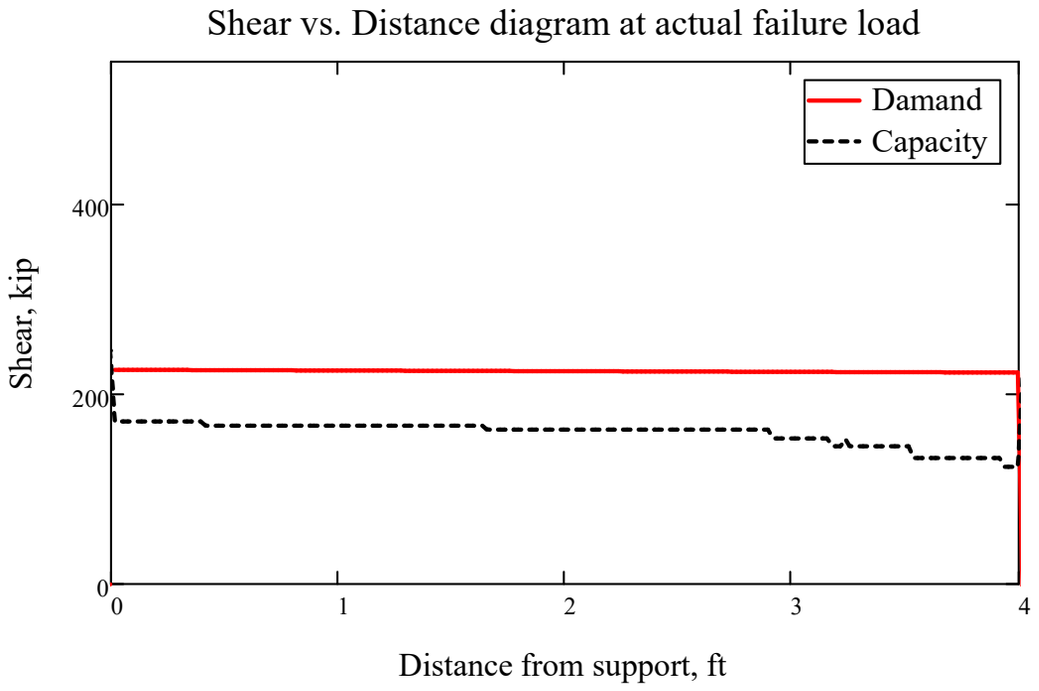

SHEAR CALCS USING ACI Vci-Vcw :

$VV_{n_1} = 202.276 \cdot kip$ Undamaged shear strength at the critical section for shear

$VV_{n_2} = 185.21 \cdot kip$ Damaged shear strength at the critical section for shear

$PP_{kill_1} = 206.538 \cdot kip$ Load to cause shear failure at the critical section for undamaged condition

$PP_{kill_2} = 187.839 \cdot kip$ Load to cause shear failure at the critical section for damaged condition

Shear strength and shear demand along the shear span under the actual failure load:

$P_{test} := 230.53kip$ Failure load from test